Utah State University

DigitalCommons@USU

All Graduate Theses and Dissertations | Graduate Studies

5-2013

A Numerical Algorithm for Simulating Two Species Plasma

Richard F. Datwyler
Utah State University

Follow this and additional works at: https://digitalcommons.usu.edu/etd

Part of the Plasma and Beam Physics Commons

Recommended Citation

Datwyler, Richard F., "A Numerical Algorithm for Simulating Two Species Plasma" (2013). *All Graduate Theses and Dissertations*. 1512.
https://digitalcommons.usu.edu/etd/1512

This Dissertation is brought to you for free and open access by the Graduate Studies at DigitalCommons@USU. It has been accepted for inclusion in All Graduate Theses and Dissertations by an authorized administrator of DigitalCommons@USU. For more information, please contact digitalcommons@usu.edu.

A NUMERICAL ALGORITHM FOR SIMULATING TWO SPECIES PLASMA

by

Richard F Datwyler

A dissertation submitted in partial fulfillment
of the requirements for the degree

of

DOCTOR OF PHILOSOPHY

in

Physics

Approved:

W. Farrell Edwards Major Professor	Eric D. Held Committee Member
Ajay K. Singh Committee Member	David Peak Committee Member
Joseph Koebbe Committee Member	Mark R. McLellan Vice President for Research and Dean of the School of Graduate Studies

UTAH STATE UNIVERSITY
Logan, Utah

2013

Copyright © Richard F Datwyler 2013

All Rights Reserved

ABSTRACT

A Numerical Algorithm for Simulating

Two Species Plasma

by

Richard F Datwyler, Doctor of Philosophy

Utah State University, 2013

Major Professor: Dr. W. Farrell Edwards
Department: Physics

An algorithm for modeling two species plasmas, which evolves the number density, flow velocity, and temperature equations coupled to Maxwell's electric and magnetic field equations, is discussed. Charge separation effects and the displacement current are retained. Mathematical derivations of normal modes in cold and hot plasmas, as represented by dispersion relations resulting from a linear analysis of the two fluid equations, are presented. In addition, numerical theory in relation to the ideas of geometry, temporal and spatial discretization, linearization of the fluid equations, and an expansion using finite elements is given. Numerical results generated by this algorithm compare favorably to analytical results and other published work. Specifically, we present numerical results, which agree with electrostatics, plasma oscillations at zero pressure, finite temperature acoustic waves, electromagnetic waves, whistler waves, and magnetohydrodynamics (MHD) waves, as well as a Fourier analysis showing fidelity to multiple dispersion relations in a single simulation. Final consideration is given to two species plasma stability calculations with a focus on the force balance of the initial conditions for a resistive MHD tearing mode benchmark and a static minimum energy plasma state.

(90 pages)

PUBLIC ABSTRACT

A Numerical Algorithm for Simulating
Two Species Plasma
by
Richard F Datwyler

In our ever-growing technology-dependent society, a great need for cleaner, more lucrative energy sources is being sought out. Nuclear fission power plants have been used to help provide energy for many years now. More recently, fusion test reactors have been built and planned as another means to fill the energy quota. A large part of understanding the fundamental principles in a fusion reactor focuses on the principles of plasma physics. This topic of plasma physics has been studied for many decades and much progress has been made in its understanding.

More recently, computers have become larger and faster allowing for more parameters and larger computations to be simulated. With this increase in computer ability and the growing interest in plasma physics, a sway from a previously heavily used simplification, magnetohydrodynamics (MHD), to a two species approach is often being adopted. This study is of the later research type. It focuses on the physical theory that describes a plasma by considering both the ions and electrons as separate species with the ability to have distinct number densities, velocities, and temperatures. In addition the computational results are compared against solutions that have been found by solving for known parameters from a linear analysis of the two fluid equations. Other considerations include the ideas of geometry, linearization, and breaking the problem down into grids, which describe how the plasma behaves in three dimensions, as well as in time. Specific results are presented to agree with previously known parameters such as: electrostatics, plasma oscillations at zero pressure, finite temperature acoustic waves, electromagnetic waves, whistler waves, and magnetohydrodynamics (MHD) waves, as well as an analysis showing fidelity to multiple relationships in a single simulation. Finally a consideration is given to the stability of a two species plasma, noting first the balance of forces in the initial conditions given for a specific MHD benchmark state and a static minimum energy plasma state.

ACKNOWLEDGMENTS

I would like to thank all of the wonderful people who have helped me to accomplish the dissertation, such as Dr. Eric Held, who made the NIMROD code available to me, as well as taking the time to explain it. He also spent many hours giving advice and clarifications on numerical formulations. This work would not be possible without his help. I am also grateful to Dr. W. Farrell Edwards, whose vision was able to extend this opportunity for me to learn more about energy and plasmas.

I give great thanks to my family and my wife, who have supported me and taken on extra family responsibilities as I have been away from home working on my research. To my children, who have enjoyed looking at the pretty pictures, and who gave me great distractions between the pages of this text. And to my parents, who taught me to dream big and gave me the encouragement and means to become whatever I wanted to be.

Thank you all.

Richard F Datwyler

CONTENTS

Page

ABSTRACT iii

PUBLIC ABSTRACT iv

ACKNOWLEDGMENTS v

LIST OF TABLES viii

LIST Of FIGURES ix

CHAPTER

1. INTRODUCTION 1

2. THEORY 6

   2.1. Introduction 6
   2.2. Boltzmann equation and velocity moments 6
   2.3. Initial fluid and Maxwell's equations 12
   2.4. Nondimensional equations 14
   2.5. Dispersion relations 17

3. NUMERICAL THEORY 25

   3.1. Introduction 25
   3.2. Geometry 25
   3.3. Time discretization 28
   3.4. Spatial discretization 28
   3.5. Finite element method 29
   3.6. NIMROD expansion 30
   3.7. Hyperbolic form of Maxwell's equations 32

4. NUMERICAL TESTS OF THE IDEAL TWO FLUID MODEL IN NIMROD 35

   4.1. Electrostatic oscillations in plasmas 35
   4.2. Acoustic wave, plasma oscillations, and finite temperature effects 37
   4.3. Time advance effects 38
   4.4. Effects of temperature on plasma frequency 40
   4.5. Grid refinement 42
   4.6. Electromagnetic wave test 43
   4.7. Whistler waves 44
   4.8. MHD waves more general 47
   4.9. Fourier analysis 49
   4.10. Waves in periodic cylinder geometry 50

5. LINEAR STABILITY TESTS 54

   5.1. Resistive tearing modes in cylindrical geometry 54
   5.2. Minimum energy equilibrium 61

REFERENCES 71

APPENDIX 74

CURRICULUM VITAE 78

LIST OF TABLES

Table		Page
1	A comparison of analytical and numerical plasma frequencies at different number densities.	39
2	Comparison of analytical and numerical results of pressure effects on acoustic mode frequency with percent error.	43
3	Convergence to the analytical solution by refining the grid size, namely, h-type refinement.	43
4	Convergence to the analytical solution by refining the polynomial degree, namely, p-type refinement.	44
5	Comparison of analytical and numerical results of acoustic mode dispersion relations between the three different geometries we tested.	52

LIST OF FIGURES

Figure		Page
1	Different plasma regimes as described by their number density verses their temperature.	2
2	Different plasma waves existing in a fully ionized plasma.	4
3	Rectangular or slab geometry, with a rectangular logical grid for the variables (R,Z).	26
4	Cylindrical geometry, with a rectangular logical grid for the variables (R,Z).	26
5	Cylindrical geometry, with circular logical grid for the variables (R,Z).	27
6	Rectangular logical grid with grid packing at the edge and circular grid with grid packing near the outer edge.	27
7	Contours of electric potential calculated from a charge density that had the form of a two-dimensional Gaussian function that went to zero on the cell boundaries.	36
8	Contours of the electric potential calculated from a charge density that had the form of a sinusoidal wave in both the x and y direction.	36
9	Plasma frequency versus number density shows the appropriate $\sqrt{n_s}$ dependence.	39
10	Convergence of the numerical solution as the time step is decreased.	40
11	Electric field energy for fully explicit ($\theta = 0$), fully implicit ($\theta = 1$), and $\theta = 0.5$ calculations showing improved energy conservation in the second order, $\theta = 0.5$ case.	41
12	Graphical representation of Table 2.	44
13	A blown up portion of the acoustic mode dispersion relation to highlight the effect of temperature on plasma frequency.	45
14	Angular frequency, ω, verses wave number, k, for light waves.	46
15	The index of refraction versus the oscillation frequency, n^2, vs. ω.	47
16	The whistler mode shows a close-up view of the evanescent region, $\omega_{ce} < \omega < \omega_{cutoff}$, the electron cyclotron resonance, $\omega = \omega_{ce}$, and the free space electromagnetic propagation behavior, $\omega \gg \omega_{cutoff}$.	48
17	The initiation and the progression of a sharp Gaussian function, which initializes many different plasma waves evolving in time.	49
18	The same Gaussian function perturbation as in Fig. 17 in a three-dimensional representation.	50
19	Contours of the Fourier spectrum from a spatially localized perturbation, which then evolved into a suite of normal mode oscillations.	51
20	The Fourier spectrum with analytical dispersion relation results overlaying the numerical contours, which indicate normal modes excited in the plasma.	51

21 The graph on the left shows the initial perturbation of the electron velocity in the Z direction. 53

22 The initial perturbations for all three cases, this time in a 3-D format for rectangular linear, rectangular toroidal, and circular linear geometry. 53

23 The magnetic field in the azimuthal direction, the current density in the azimuthal, and axial directions, and pressure. 56

24 Equilibrium electric field in the axial direction, the axial components of the ion and electron flows, and the ion pressure, which equals the electron pressure. 57

25 The azimuthal magnetic field is the same as the MHD case; also, note the azimuthal electric field is shown here. 59

26 The ion and electron number densities and electric field profiles. 63

27 The ion and electron number densities and electric field profiles, as provided by Dr. Edwards. 64

28 The ion and electron equilibrium velocity profiles, as well as the equilibrium magnetic field in the azimuthal direction, as provided by Dr. Edwards. 65

29 The progression of perturbations in the radial electron flow that originate at the outside edge of the plasma column, most likely from lack of balance of forces at the outer edge. 66

30 The evolution of the electric field in the axial direction. 67

31 The results of Eq. (230) in a graphical form as the dotted line. 69

CHAPTER 1

INTRODUCTION

In this world of ever-changing technology, economic conditions, and political and social ideals, much emphasis is placed on the production and consumption of energy. Looking at the available sources of energy, their renewable natures, and the side effects of energy production has led many to look for superior energy options. In the mid-twentieth century, many eyes turned to nuclear fission. However, what was once hailed as a possible solution to our energy needs has recently raised more questions than answers. Fission devices have led to large-scale disasters, as well as large volumes of radioactive byproducts. The level of risk has changed society's view towards fission and its future is uncertain.

At roughly the same time, many minds were researching a different nuclear process, namely, fusion. The first fusion machines were operated in the mid-1950's in the USSR, the United Kingdom, United States, France, Germany, and Japan. Energy from nuclear fusion has enormous potential as an abundant renewable resource with fewer byproducts. Recently, more of the plasma parameters required for significant fusion to occur have been achieved in devices like TFTR[1] (Tokamak Fusion Test Reactor in Princeton, USA), JET[2] (Joint European Torus in the UK) and JT-60[3] (in Japan). Currently, much effort and funding is going to ITER[4] (International Thermonuclear Experimental Reactor in France), an international attempt to demonstrate controlled thermonuclear fusion at the level of 300-500 MW. Fundamental to the production of energy from fusion is the understanding of magnetically confined plasmas.

A plasma is an ionized gas consisting of ions, electrons, and neutral particles. It differs from a normal gas in that long-range electric and magnetic forces play a more central role than short-range forces. A plasma can be achieved by adding sufficient energy to an ordinary gas such that the ionization rate exceeds the recombination rate.

Not only is the study of plasmas important for progress in fusion energy production, but much of the known universe is composed of plasmas at different temperature and densities. Examples include the solar corona, gaseous nebulae, the Earth's ionosphere, the solar wind, and flames. Examples of laboratory plasmas include shock tubes, z-pinches, laser plasma, plasma focus, and tokamaks. Fig. 1 shows a graphical listing of some of these examples. Note the extreme range in densities

[1] http://www.pppl.gov/projects/pages/tftr.html
[2] http://www.efda.org/jet/
[3] http://www-jt60.jaea.go.jp/english/index-e.html
[4] http://www.iter.org/

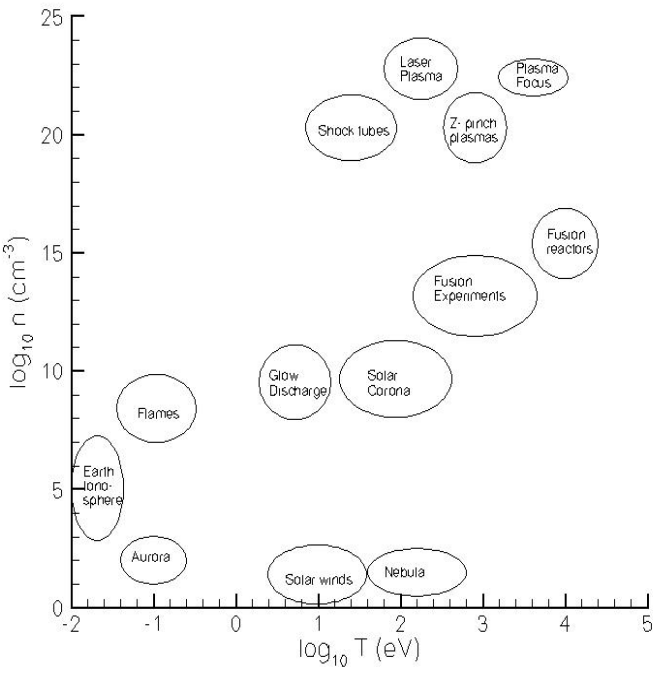

Fig. 1. Different plasma regimes as described by their number density verses their temperature. Both axis are log base 10 scale and units are listed. [1]

and temperatures of the plasma state for both naturally occurring plasmas, as well as man-made plasmas.

As groups have studied the characteristics and effects of plasma, much success has come from thinking of the plasma species, electron, ion and neutrals, as fluids. One such model is called magnetohydrodynamics (MHD).

In MHD studies, ions and electrons move together as a conducting fluid and plasma motion is characterized by low-frequency and long-wavelength oscillations. Many studies have been done using ideal MHD, which assumes no dissipative effects like resistivity or viscosity [2]. In addition many reduced and extended versions of MHD exist with comprehensive studies being done on them [3, 4]. The extended versions add in separate species affects through nontrivial additions to Ohm's Law, like the Hall current. This is an attempt to make MHD more of a two fluid theory [5]. In addition other models, like electron magnetohydrodynamics (EMHD), ignore low-frequency waves and focus only on the upper frequency limits imposed by the motion of electrons inside the plasma. Yet in either case of high- or low-frequency limits of the MHD models, there are still many concepts lacking. The focus on MHD is somewhat due to the nature of the computational challenge of correctly modeling

plasma effects. Studies focusing on the MHD models require less computational power to achieve results. Early focus on MHD models is, in part, due to the fact computational power was equally limited during the same historical timeframe.

Because of advancements in computational speed, more difficult problems have a larger chance of success than they once did. Cray supercomputers are able to perform petaflop calculations at lightning-fast speeds in comparison to those of a few decades ago when ideal MHD was primarily being used. As such, previously unaddressed terms and features of plasma fluid models are able to be studied.

In most MHD models a quasi-neutrality assumption is made, wherein the ions and electrons move in such a way that no long-range charge separation can build up, creating a net charge. The two species model drops this quasi-neutrality idea by allowing there to be separate number densities and separate flow variables describing both the ions and the electrons. This leads to the possibility of substantial charge separation and resultant strong electric fields. In addition, Maxwell's displacement current in Ampère's Law is retained in this work. These ideas are not addressed in ideal MHD or extended MHD schemes like Hall MHD and EMHD.

Building on the success of computational models of MHD, two species models are beginning to surface, which address the nature and effects of these terms on the plasma [6, 7]. The results are promising. Success has been found in reproducing previous MHD phenomena, as well as modeling other two species effects that lie outside the realm of MHD. Numerical algorithms for two species models have focused on finite volume (Galerkin and Riemann solvers) [8–10] and finite element [11, 12] spatial discretization techniques. The work outlined in this paper builds on this same idea of developing an algorithm that can work in the ideal MHD and extended MHD regimes, both high and low frequencies, as well as model the full two species system that removes the quasi-neutrality restriction by advancing separate continuity, flow, and temperature equations for both ions and electrons.

Inherent in the study of plasma physics, as it applies to disciplines ranging from space weather and solar studies, to astrophysics and the fusion community, is the study of waves. Ideal MHD focuses on Alfvén waves, but many other waves exist in plasmas [13–15]. Some examples of waves in a cold plasma are shown in Fig. 2. Ideal MHD allows for certain waves to exist, shear Alfvén, slow, and fast magnetosonic modes. Extended MHD allows for the addition of X, O, R, (often referred to as the whistler mode) and L waves. The two fluid equations described in this work capture these waves, as well as electromagnetic, acoustic, and Langmuir waves. Understanding the nature of plasma waves can lead to better understanding of plasmas in applications of stability

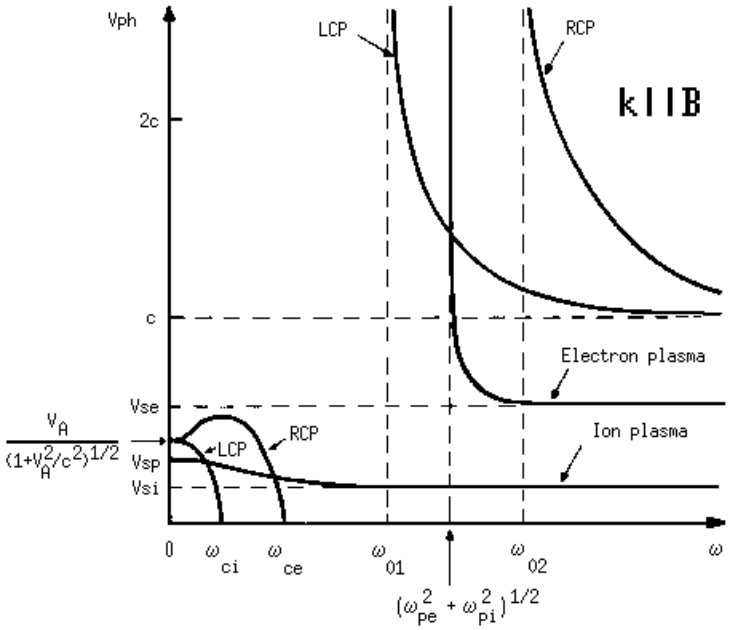

Fig. 2. Different plasma waves existing in a fully ionized plasma. Electron and ion waves are shown here with phase speed plotted as a function of frequency for various modes. Left and right circularly polarized waves are shown here with notable Alfvén speeds (V_A), sound speeds (V_{se}, V_{si} andV_{sp}), cyclotron frequencies (ω_{ce} and ω_{ci}), and plasma frequencies (ω_{pe} and ω_{pi}).

and transport in fusion devices, as well as ionospheric plasmas. In this work we look at different modes, which are excited in a two fluid plasma, and test our algorithm's ability to predict behavior consistent with linear dispersion relations. These tests show the robust nature of our computational model in predicting both high- and low-frequency behavior. In addition, we discuss preliminary work involving stability calculations of resistive tearing modes [16] and minimum energy equilibrium in cylindrical geometry.

Much success has been achieved using extended MHD codes, which consider the effects of resistivity, Hall MHD and two fluid problems. One such code, freely available to plasma physicists, is called NIMROD [17, 18]. NIMROD is an acronym for Non-Ideal Magnetohydrodynamics with Rotation Open Discussion. The NIMROD code has been designed to model the effects of plasmas in different geometries for different applications. The work outlined in this paper focuses on taking the NIMROD algorithm and adjusting the existing code to consider ions and electrons as two separate species, with individual variables describing the number densities, velocities, and temperatures of each species. In addition, the electric field is advanced in time with the displacement current in Ampère's Law. This is in contrast to using NIMROD's ideal or extended Ohm's Law. Separate electron and ion density evolution equations allow for charge separation and the formation of internal

electric fields as discussed in [19]. Critical to this study was the inclusion of the displacement current, which introduces fast oscillations associated with electromagnetic waves. In addition, because of the nonneutrality assumption, we are able to model high-frequency plasma oscillations with and without the effects of pressure. Because of the presence of these higher-frequency oscillations, an implicit time advance is needed when performing stability calculations of slow-growing modes.

The genesis of this research has come about as all of these ideas have merged together: an interest in the need for cleaner, safer, and more renewable energy, the study of the nature of the plasma state and an understanding of the waves that can exist in a plasma, and an extension of the paradigms of studying plasmas from ideal and extended MHD to that of a fully two fluid model with high- and low-frequency waves bouncing around during stability calculations. We will look at these ideas in more detail as we move through the sections of this thesis.

We begin with a study of plasma theory, a derivation of the two species flow evolution, and number density and temperature equations, which couple to Maxwell's electric and magnetic field equations. The normal modes of cold and hot plasmas, as represented by dispersion relations resulting from a linear analysis of the two fluid equations, will be covered in the next section. Chapter 3, a numerical theory discussion will cover the ideas of geometry, temporal and spatial discretization, linearization of the fluid equations, and the NIMROD expansion using the finite element approach. Chapter 4 will discuss the numerical results of the algorithm, specifically electrostatics, acoustic waves, temperature effects on acoustic waves, θ-centered time advances, electromagnetic waves, whistler waves, MHD waves, and a Fourier analysis of many different plasma waves. A final chapter will discuss future work looking at the modeling of resistive MHD modes with two species equations, as well as a the stability of a static equilibrium minimum energy plasma state.

CHAPTER 2

THEORY

2.1. Introduction

In the study of the natural world, specific nomenclature has been developed to describe interactions between atoms. Atoms that are bonded tightly together are solids, liquids have less bonding, and gases are individual atoms. A plasma is a gas that has been ionized so it consists of electrons and ions, as well as some neutral atoms. Particles in a plasma are free to interact with one another, and with external and internal electric and magnetic fields. As they interact, their distribution functions change. Certain state variables have been assigned to describe different aspects of their collective position, motion, and energy, such as density, macroscopic velocity (flow), and temperature. Although this work focuses on fluid quantities like density, we will begin by discussing plasma kinetic theory and distribution functions.

2.2. Boltzmann equation and velocity moments

The distribution function, $f_s(\mathbf{r}, \mathbf{v}_s, t)$, describes the phase space density of a species, s, as a function of the independent variables position, velocity, and time. Here the species can be electrons, ions, or neutrals. This function evolves in time according to the Boltzmann equation,

$$\frac{\partial f_s}{\partial t} + \mathbf{v}_s \cdot \nabla f_s + \mathbf{a}_s \cdot \nabla_v f_s = \frac{\delta f_s}{\delta t} \ , \tag{1}$$

where, for the purpose of this thesis, the acceleration is given by $\mathbf{a}_s = (q_s/m_s)\,(\mathbf{E} + \mathbf{v}_s \times \mathbf{B})$, and $\frac{\delta f_s}{\delta t}$ represents the effects of binary Coulomb collisions, which will take a simplified form. Here q_s is the species charge, m_s is the species mass, and $\mathbf{E}$ and $\mathbf{B}$ are the electric and magnetic fields, respectively.

At this point, we need to define some velocity moments. The distribution function, $f_s(\mathbf{r}, \mathbf{v}_s, t)$, represents the probable number of particles of a given species found in an infinitesimal phase space volume at location, $\mathbf{r}$, with velocity, $\mathbf{v}$, at time, t. If this function is integrated over all velocities, the result would be the number of particles of a given species at location, $\mathbf{r}$, at a specific time, namely, the number density,

$$n_s(\mathbf{r}, t) = \int d^3 v_s f_s(\mathbf{r}, \mathbf{v}_s, t) \ . \tag{2}$$

In a similar manner, an average drift (flow) velocity of a given species, $\mathbf{u}_s(\mathbf{r}, t)$, can be found by integrating the distribution function multiplied by the velocity, and then dividing by the number

density,

$$\mathbf{u}_s(\mathbf{r},t) = \frac{\int d^3v_s \mathbf{v}_s f_s(\mathbf{r},\mathbf{v}_s,t)}{\int d^3v_s f_s(\mathbf{r},\mathbf{v}_s,t)} \ . \tag{3}$$

This brings in the idea of taking velocity moments of the Boltzmann equation. This method of taking velocity moments has been studied at length. In the early works of Chapman [20], Enskog [21], Burnett [22] and others, it was done using the particle velocity, $\mathbf{v}_s(\mathbf{r},t)$. As the distribution function is multiplied by different velocity terms and then integrated over $\mathbf{v}_s$, velocity moments are obtained. For example, if the distribution function is multiplied by $\frac{1}{2}m_s v_s^2$ and then integrated over $\mathbf{v}_s$, the kinetic energy density or temperature equation may be obtained. It should be noted Grad [23, 24] did a similar treatment, but used the random velocity for the velocity moment expansions, defining the random velocity as the difference between the total velocity and the drift velocity, $\mathbf{c}_s = \mathbf{v}_s - \mathbf{u}_s$. Given this definition for $\mathbf{c}_s$, the heat flow and pressure tensor can be found by multiplying f_s by $\frac{1}{2}n_s c_s^2 \mathbf{c}_s$ and $n_s m_s \mathbf{c}_s \mathbf{c}_s$, respectively, and integrating over a $\mathbf{v}_s$. Three important moments: kinetic energy, heat flow, and the pressure tensor are shown below:

$$W_s(\mathbf{r},t) = \frac{3}{2}k_B n_s T_s = \int d^3v_s \frac{1}{2} m_s v_s^2 f_s(\mathbf{r},\mathbf{v}_s,t) \ , \tag{4}$$

$$\mathbf{q}_s\left(\mathbf{r},t\right) = \int d^3v_s \frac{1}{2} n_s m_s c_s^2 \mathbf{c}_s f_s(\mathbf{r},\mathbf{v}_s,t) \ , \tag{5}$$

$$\mathbf{P}_s\left(\mathbf{r},t\right) = \int d^3v_s n_s m_s \mathbf{c}_s \mathbf{c}_s f_s(\mathbf{r},\mathbf{v}_s,t) \ . \tag{6}$$

One often separates out the pressure tensor into its diagonal and off diagonal elements, $\mathbf{P}_s = \boldsymbol{\tau}_s + p_s \boldsymbol{I}$, where $\boldsymbol{\tau}_s$ is the stress tensor leaving the scalar quantity p_s to multiply $\boldsymbol{I}$, the unit tensor.

Now that some common velocity moments of the distribution function have been defined, a similar analysis can be used to find the transport equations by taking velocity moments of the Boltzmann equation. It is convenient to make a change in the notation of the Boltzmann equation. This is done by noting the complete divergence of the following terms simplifies to the previous version of the equation, because $\mathbf{r}$, $\mathbf{v}_s$, and t are independent, as shown below:

$$\nabla \cdot \left(f_s \mathbf{v}_s\right) = \left(\mathbf{v}_s \cdot \nabla\right) f_s + f_s \left(\nabla \cdot \mathbf{v}_s\right) = \left(\mathbf{v}_s \cdot \nabla\right) f_s \ , \tag{7}$$

and

$$\nabla_v \cdot (f_s \mathbf{a}_s) = (\mathbf{a}_s \cdot \nabla_v) f_s + f_s (\nabla_v \cdot \mathbf{a}_s) = (\mathbf{a}_s \cdot \nabla_v) f_s \ . \tag{8}$$

The later works because in the acceleration, $\mathbf{a}_s = \frac{q_s}{m_s}(\mathbf{E} + \mathbf{v}_s \times \mathbf{B})$, and the terms $\nabla_v \cdot \mathbf{E} = 0$ and $\nabla_v \cdot (\mathbf{v}_s \times \mathbf{B}) = 0$. This is due to the nature of the electric and magnetic fields being independent of velocity, and the divergence of the cross product of velocity and magnetic field being zero.

With those simplifications, we start by taking the zeroth order moment and integrating the modified Boltzmann equation over all velocities

$$\int d^3 v_s \left[\underbrace{\frac{\partial f_s}{\partial t}}_{1} + \underbrace{\nabla \cdot (f_s \mathbf{v}_s)}_{2} + \underbrace{\nabla_v \cdot (f_s \mathbf{a}_s)}_{3} \right] = \underbrace{\int d^3 v_s \frac{\delta f_s}{\delta t}}_{4} \ . \tag{9}$$

Looking at the first term, the velocity integral can be brought inside the partial derivative with respect to time, and thus, we obtain the partial time derivative of the number density,

$$\frac{\partial \int d^3 v_s f_s}{\partial t} = \frac{\partial n_s}{\partial t} \ . \tag{10}$$

In the second term the same procedure can be done again, taking the velocity integral inside the divergence, thus obtaining the divergence of the number density times the drift velocity,

$$\nabla \cdot \int d^3 v_s f_s \mathbf{v}_s = \nabla \cdot (n_s \mathbf{u}_s) \ . \tag{11}$$

The third term makes use of Gauss's theorem, with the surface term evaluated as the velocity goes to infinity. If f_s falls off more rapidly than v_s^2, there are few particles with velocities outside a chosen Gaussian surface and

$$\int d^3 v_s \nabla_v \cdot f_s \mathbf{a}_s = \oint_s dA_v \, (f_s \mathbf{a}_s) \cdot \hat{\mathbf{n}}_s = 0 \ . \tag{12}$$

Lastly, we define the right side integral as the collision term:

$$\int d^3 v_s \frac{\delta f_s}{\delta t} = \frac{\delta n_s}{\delta t} \tag{13}$$

leaving

$$\frac{\partial n_s}{\partial t} + \nabla \cdot (n_s \mathbf{u}_s) = \frac{\delta n_s}{\delta t} \ . \tag{14}$$

This equation is the zeroth order velocity moment of the Boltzmann equation, which is the evolution equation for number density, often called the continuity equation.

Similarly, the first order velocity moment of the Boltzmann equation can be found. It results in an evolution equation for the drift velocity. Proceeding by multiplying the Boltzmann equation by $m_s\mathbf{v}_s$ and integrating over all velocities, we have

$$m_s \int d^3v_s \left[\underbrace{\mathbf{v}_s \frac{\partial f_s}{\partial t}}_{1} + \underbrace{\mathbf{v}_s \nabla \cdot (f_s \mathbf{v}_s)}_{2} + \underbrace{\mathbf{v}_s \nabla_v \cdot (f_s \mathbf{a}_s)}_{3} \right] = \underbrace{m_s \int d^3\mathbf{v}_s \frac{v_s \delta f_s}{\delta t}}_{4} \ . \tag{15}$$

In term 1, we bring the v_s term and the integral inside the partial time derivative and use the moment definition to get

$$\frac{\partial \left(\int d^3v_s \mathbf{v}_s f_s \right)}{\partial t} = m_s \frac{\partial \left(n_s \mathbf{u}_s \right)}{\partial t} \ . \tag{16}$$

For the second term, we pull the del operator out of the velocity space integral and use $\mathbf{v}_s\mathbf{v}_s = (\mathbf{v}_s - \mathbf{u}_s)(\mathbf{v}_s - \mathbf{u}_s) + \mathbf{u}_s\mathbf{v}_s + \mathbf{v}_s\mathbf{u}_s - \mathbf{u_s}\mathbf{u_s}$. After the integral over all velocity space is performed, the last two terms cancel, leaving

$$\nabla \cdot m_s \int d^3v_s \left(\mathbf{v}_s \mathbf{v}_s f_s \right) = \nabla \cdot \mathbf{P}_s + \nabla \cdot \left(m_s n_s \mathbf{u_s} \mathbf{u_s} \right) \ , \tag{17}$$

where we have used our pressure tensor moment from earlier.

Term 3 is more complicated. We begin by using index notation: $\mathbf{v}_s \nabla_v \cdot f_s \mathbf{a}_s = v_\alpha \frac{\partial}{\partial v_\beta} f a_\beta$, and consider

$$\begin{aligned} \frac{\partial}{\partial v_\beta} v_\alpha f a_\beta &= \frac{\partial v_\alpha}{\partial v_\beta} f a_\beta + v_\alpha \frac{\partial}{\partial v_\beta} f a_\beta \\ &= \partial_{\alpha\beta} f a_\beta + v_\alpha \frac{\partial}{\partial v_\beta} f a_\beta \\ &= f a_\alpha + v_\alpha \frac{\partial}{\partial v_\beta} f a_\beta \quad . \end{aligned} \tag{18}$$

Therefore, the third term of the momentum advance can be written as

$$\int d^3v_s \mathbf{v}_s \nabla_v \cdot (f_s \mathbf{a}_s) = \int d^3v_s \nabla_v \cdot (\mathbf{a}_s f \mathbf{v}_s) - \int d^3v_s f_s \mathbf{a}_s \ . \tag{19}$$

Again from the divergence theorem, the first term goes to zero, leaving only the second term. If the

acceleration is taken from the Lorentz force, this simplifies to

$$\int d^3 v_s \mathbf{v}_s \nabla_v \cdot (f_s \mathbf{a}_s) = -\frac{n_s e_s}{m_s} \left(\mathbf{E} + \mathbf{u}_s \times \mathbf{B}\right) \ . \tag{20}$$

Finally, term 4 of the original equation is defined to be a collisional term noted as

$$m_s \int d^3 \mathbf{v}_s \frac{\mathbf{v}_s \delta f_s}{\delta t} = \frac{\delta M_s}{\delta t} \ . \tag{21}$$

Collecting terms yields

$$m_s \frac{\partial n_s \mathbf{u}_s}{\partial t} + \nabla \cdot (m_s n_s \mathbf{u_s} \mathbf{u_s}) + \nabla \cdot \mathbf{P}_s - n_s e_s \left(\mathbf{E} + \mathbf{u}_s \times \mathbf{B}\right) = \frac{\delta M_s}{\delta t} \ . \tag{22}$$

To simplify, we consider the first two terms in this equation and use the product rule

$$\begin{aligned} m_s \frac{\partial n_s \mathbf{u}_s}{\partial t} + \nabla \cdot (m_s n_s \mathbf{u_s} \mathbf{u_s}) &= m_s n_s \frac{\partial \mathbf{u}_s}{\partial t} + m_s \mathbf{u}_s \frac{\partial n_s}{\partial t} + m_s n_s \left(\mathbf{u}_s \cdot \nabla\right) \mathbf{u_s} + m_s \mathbf{u}_s \nabla \cdot (n_s \mathbf{u_s}) \\ &= m_s n_s \left[\frac{\partial \mathbf{u}_s}{\partial t} + \left(\mathbf{u}_s \cdot \nabla\right) \mathbf{u_s}\right] + m_s \mathbf{u}_s \left[\frac{\partial n_s}{\partial t} + \nabla \cdot (n_s \mathbf{u_s})\right] \ . \end{aligned} \tag{23}$$

We note the last term is the continuity equation multiplied by the momentum, which can be set to zero so long as there are no production or loss terms for the number density. This leaves a final form for the momentum moment, or the evolution of species flow (drift velocity) as

$$m_s n_s \left[\frac{\partial \mathbf{u}_s}{\partial t} + \left(\mathbf{u}_s \cdot \nabla\right) \mathbf{u_s}\right] + \nabla \cdot \mathbf{P}_s - n_s e_s \left(\mathbf{E} + \mathbf{u}_s \times \mathbf{B}\right) = \frac{\delta M_s}{\delta t} \ , \tag{24}$$

where one can write the pressure tensor term as $\nabla \cdot \mathbf{P}_s = \nabla p_s + \nabla \cdot \boldsymbol{\tau}_s$.

Before leaving this section, one more velocity moment expansions is required, specifically the second order scalar moment used to find the evolution of energy density or temperature. This is done by multiplying the Boltzmann equation by $\frac{1}{2} m_s c_s^2$ and then massaging each individual term as has been shown twice now. Rather than following the same approach, we note Maxwell developed a method of formulating each of the velocity moment expansions called the Maxwell transfer equation. As a good demonstration of its effectiveness, consider its use to find the energy evolution equation.

The Maxwell transfer equation in general terms is

$$\underbrace{\frac{\partial}{\partial t}\left(n_s\left\langle\xi_s\right\rangle\right)}_{1}+\underbrace{\nabla\cdot\left(n_s\left\langle\mathbf{c}_s\xi_s\right\rangle\right)}_{2}+\underbrace{\mathbf{u}_s\cdot\nabla\left(n_s\left\langle\xi_s\right\rangle\right)}_{3}$$
$$+\underbrace{n_s\frac{D_s\mathbf{u}_s}{Dt}\cdot\left\langle\nabla_c\xi_s\right\rangle}_{4}-\underbrace{n_s\left\langle\mathbf{a}_s\cdot\nabla_c\xi_s\right\rangle}_{5}$$
$$+\underbrace{n_s(\nabla\mathbf{u}_s):\left\langle\nabla_c\left(\mathbf{c}_s\xi_s\right)\right\rangle}_{6} \;=\; \underbrace{\int d^3c_s\xi_s\frac{\delta f_s}{\delta t}}_{7}\,, \tag{25}$$

where ξ_s is the velocity moment to be multiplied to the Boltzmann equation. Before using it to derive the energy equation, it can be used to prove correctness for the first two velocity moments, for the continuity equation, $\xi_s = 1$, and for the momentum equation, $\xi_s = m_s\mathbf{v}_s$. Also note $\langle A_s\rangle$ denotes an average defined as $\langle A_s\rangle = \int d^3c_sA_sf_s$. For the continuity equation only, terms 1, 3, 6, and 7 survive giving $\frac{\partial n_s}{\partial t}+\left(\mathbf{u}_s\cdot\nabla\right)n_s+n_s\left(\nabla\cdot\mathbf{u}_s\right)=\frac{\delta n_s}{\delta t}$. The other confidence test is when $\xi_s = m_s\mathbf{v}_s$, and terms 1, 2, 5, 6, and 7 survive giving $m_s\frac{\partial n_s\mathbf{u}_s}{\partial t}+\nabla\cdot\mathbf{P}_s-n_se_s\left(\mathbf{E}+\mathbf{u}_s\times\mathbf{B}\right)+\nabla\cdot m_sn_s\mathbf{u_s}\mathbf{u_s}=\frac{\delta M_s}{\delta t}$, which is the momentum equation.

Proceeding to the case where $\xi_s = \frac{1}{2}m_sc_s^2$, we note first $\left\langle\frac{1}{2}m_sc_s^2\right\rangle=\frac{3}{2}k_BT_s$. Also, when that term is multiplied by n_s, the first and third terms become $\frac{\partial\frac{3}{2}p_s}{\partial t}$ and $\mathbf{u}_s\cdot\nabla\frac{3}{2}p_s$, respectively. Here we have used the ideal gas law, $p_s = n_sk_BT_s$. Collecting those from the first few terms in Maxwell's transfer equation gives a preliminary result of

$$\frac{\partial\frac{3}{2}p_s}{\partial t}+\nabla\cdot\mathbf{q}_s+\left(\mathbf{u}_s\cdot\nabla\right)\frac{3}{2}p_s+0-0+\underbrace{\frac{1}{2}n_sm_s\nabla\mathbf{u}_s:\left\langle\nabla_c\left(\mathbf{c}_sc_s^2\right)\right\rangle}_{A}=\frac{\delta\mathbf{E}_s}{\delta t}\,. \tag{26}$$

The only term that will take some work is term A. Start by using a product rule for the internal parenthesis, namely,

$$\begin{aligned}\frac{1}{2}n_sm_s\nabla\mathbf{u}_s:\left\langle\nabla_c\left(\mathbf{c}_sc_s^2\right)\right\rangle &= \frac{1}{2}n_sm_s\nabla\mathbf{u}_s:\left\langle\mathbf{c}_s\left(\nabla_cc_s^2\right)+\left(\nabla_c\mathbf{c}_s\right)c_s^2\right\rangle\,,\\ &= \frac{1}{2}n_sm_s\nabla\mathbf{u}_s:\left\langle\mathbf{c}_s\left(2\mathbf{c}_s\right)+\left(\mathbb{I}\right)c_s^2\right\rangle\,,\\ &= \nabla\mathbf{u}_s:\mathbf{P}_s+\frac{3}{2}n_sk_BT_s\left(\nabla\cdot\mathbf{u}_s\right)\,,\\ &= \nabla\mathbf{u}_s:\mathbf{P}_s+\frac{3}{2}p_s\left(\nabla\cdot\mathbf{u}_s\right)\quad.\end{aligned} \tag{27}$$

Finally, using $\mathbf{P}_s = p_s\boldsymbol{I}+\boldsymbol{\tau}_s$, $\nabla\mathbf{u}_s:\mathbf{P}_s$ becomes $p_s\left(\nabla\cdot\mathbf{u}_s\right)+\boldsymbol{\tau}_s:\nabla\mathbf{u}_s$, and putting these all together

yields

$$\frac{\partial \frac{3}{2} p_s}{\partial t} + (\mathbf{u}_s \cdot \nabla) \frac{3}{2} p_s + \frac{5}{2} p_s (\nabla \cdot \mathbf{u}_s) + \nabla \cdot \mathbf{q}_s + \boldsymbol{\tau}_s : \nabla \mathbf{u}_s = \frac{\delta \mathbf{E}_s}{\delta t} \ . \tag{28}$$

2.3. Initial fluid and Maxwell's equations

We list these evolution equations again for completeness. First, the continuity equation is

$$\frac{\partial n_s}{\partial t} + \nabla \cdot (n_s \mathbf{u}_s) = \frac{\delta n_s}{\delta t} \ . \tag{29}$$

Second, the momentum or flow evolution equation is

$$n_s m_s \left[\frac{\partial \mathbf{u}_s}{\partial t} + (\mathbf{u}_s \cdot \nabla) \mathbf{u}_s \right] + \nabla p_s + \nabla \cdot \boldsymbol{\tau}_s - n_s e_s (\mathbf{E} + \mathbf{u}_s \times \mathbf{B}) = \frac{\delta \mathbf{M}_s}{\delta t} \ . \tag{30}$$

Finally, the energy or evolution of pressure equation is

$$\frac{\partial \frac{3}{2} p_s}{\partial t} + (\mathbf{u}_s \cdot \nabla) \frac{3}{2} p_s + \frac{5}{2} p_s (\nabla \cdot \mathbf{u}_s) + \nabla \cdot \mathbf{q}_s + \boldsymbol{\tau}_s : \nabla \mathbf{u}_s = \frac{\delta \mathbf{E}_s}{\delta t} \ . \tag{31}$$

Those are the first five velocity moment transport equations. Notice this set of equations is not closed, meaning in the evolution of number density, flow, and pressure, there are terms for collisional particle production and loss $\left(\frac{\delta n_s}{\delta t}\right)$, stress $(\boldsymbol{\tau}_s)$, collisional friction $\left(\frac{\delta \mathbf{M}_s}{\delta t}\right)$, heat flow$(\mathbf{q}_s)$, and collisional energy exchange$\left(\frac{\delta \mathbf{E}_s}{\delta t}\right)$, which do not have an evolution equation or an expression in terms of lower order moments.

A modification of these equations yields a closed five moment approximation. Here the collision terms, stress tensor, and heat flow are omitted by brute force truncation:

$$\frac{\partial n_s}{\partial t} + \nabla \cdot (n_s \mathbf{u}_s) = 0 \ , \tag{32}$$

$$n_s m_s \left[\frac{\partial \mathbf{u}_s}{\partial t} + (\mathbf{u}_s \cdot \nabla) \mathbf{u}_s \right] + \nabla p_s - n_s e_s (\mathbf{E} + \mathbf{u}_s \times \mathbf{B}) = 0 \ , \tag{33}$$

$$\frac{\partial \frac{3}{2} p_s}{\partial t} + (\mathbf{u}_s \cdot \nabla) \frac{3}{2} p_s + \frac{5}{2} p_s (\nabla \cdot \mathbf{u}_s) = 0 \ . \tag{34}$$

Eqs. (32)-(34) are a simplified five moment approximation, where the assumption of no collisions is made. Likewise the heat flow or stress tensor have not been specified in any manner. Before moving on to Maxwell's equations, a change is made to the momentum and energy Eqs. (33) and (34). They will be used in another form in the numerical representation used in this study, and

these changes are described below.

First, divide the momentum equation by the mass density and use $p_s = n_s T_s$ to obtain

$$\frac{\partial \mathbf{u}_s}{\partial t} + (\mathbf{u}_s \cdot \nabla)\,\mathbf{u}_s + \frac{\nabla\,(n_s T_s)}{n_s m_s} - \frac{e_s}{m_s}\,(\mathbf{E} + \mathbf{u}_s \times \mathbf{B}) = 0\,. \tag{35}$$

Eq. (34) could be left as is with a slight modification of the 3/2 term to give an advance for the pressure

$$\frac{\partial p_s}{\partial t} + (\mathbf{u}_s \cdot \nabla)\,p_s + \frac{5}{3} p_s\,(\nabla \cdot \mathbf{u}_s) = 0\,. \tag{36}$$

For simplicity, we scale the temperature such that Boltzmann's constant is absorbed into the temperature. Again using $p_s = n_s T_s$ in Eq. (36),

$$\frac{\partial n_s T_s}{\partial t} + (\mathbf{u}_s \cdot \nabla)\,n_s T_s + \frac{5}{3} n_s T_s\,(\nabla \cdot \mathbf{u}_s) = 0\,. \tag{37}$$

Splitting up the last term and using the product rule twice on the other terms leads to

$$T_s \frac{\partial n_s}{\partial t} + n_s \frac{\partial T_s}{\partial t} + T_s\,(\mathbf{u}_s \cdot \nabla)\,n_s + n_s\,(\mathbf{u}_s \cdot \nabla)\,T_s + n_s T_s\,(\nabla \cdot \mathbf{u}_s) + \frac{2}{3} n_s T_s\,(\nabla \cdot \mathbf{u}_s) = 0\,. \tag{38}$$

Collecting terms gives

$$T_s \left[\frac{\partial n_s}{\partial t} + (\mathbf{u}_s \cdot \nabla)\,n_s + n_s\,(\nabla \cdot \mathbf{u}_s)\right] + n_s \left[\frac{\partial T_s}{\partial t} + (\mathbf{u}_s \cdot \nabla)\,T_s + \frac{2}{3} T_s\,(\nabla \cdot \mathbf{u}_s)\right] = 0\,. \tag{39}$$

Note the second and third terms in the first parenthesis gives the total divergence of $n_s \mathbf{u}_s$, which makes the first term the continuity equation multiplied by temperature: $T_s\left[\frac{\partial n_s}{\partial t} + \nabla \cdot (n_s \mathbf{u}_s)\right] = 0$. Finally, we divide by the common factor, n_s, to get an equation for the advance of temperature,

$$\frac{\partial T_s}{\partial t} + (\mathbf{u}_s \cdot \nabla)\,T_s + \frac{2}{3} T_s\,(\nabla \cdot \mathbf{u}_s) = 0\,, \tag{40}$$

which is equivalent to an adiabatic equation of state.

This then gives fluid equations to advance the number densities, flows, and pressures or temperatures leaving the need to look at evolution equations for the electric and magnetic fields. Maxwell's equations are used to advance these terms. For this study a hyperbolic form of Maxwell's equations is used [25, 26]. We begin by stating Maxwell's equations in their standard differential form:

$$\frac{\partial \mathbf{E}}{\partial t} - c^2 \left(\nabla \times \mathbf{B}\right) = -\sum_s \frac{e_s n_s \mathbf{u}_s}{\epsilon_0} \,, \tag{41}$$

$$\nabla \cdot \mathbf{E} = \sum_s \frac{e_s n_s}{\epsilon_0} \,, \tag{42}$$

$$\frac{\partial \mathbf{B}}{\partial t} + \left(\nabla \times \mathbf{E}\right) = 0 \,, \tag{43}$$

$$\nabla \cdot \mathbf{B} = 0 \,. \tag{44}$$

These equations represent six additional variables (with added potentials that will be discussed in 3.5), which are advanced in our numerical code along with

$$\frac{\partial n_s}{\partial t} + \nabla \cdot \left(n_s \mathbf{u}_s\right) = 0 \,, \tag{45}$$

$$\frac{\partial \mathbf{u}_s}{\partial t} + \left(\mathbf{u}_s \cdot \nabla\right) \mathbf{u}_s + \frac{\nabla \left(n_s T_s\right)}{n_s m_s} - \frac{e_s}{m_s} \left(\mathbf{E} + \mathbf{u}_s \times \mathbf{B}\right) = 0 \,, \tag{46}$$

$$\frac{\partial T_s}{\partial t} + \left(\mathbf{u}_s \cdot \nabla\right) T_s + \frac{2}{3} T_s \left(\nabla \cdot \mathbf{u}_s\right) = 0 \,, \tag{47}$$

which gives the last 10 variables (for two species) that are being modeled. These make up the coupled fluid and Maxwell's equations used in this study.

2.4. Nondimensional equations

In this section, the equations will be changed to a nondimensional form in the interest of making the fields we solve for numerically, all of the same order. For example, there are terms that are very large like number density, which can be on the order of 10^{18} (m^{-3}) or more, while the magnetic field, measured in Tesla, is only on the order of 1. Having nondimensional equations reduces the burden on linear algebra solvers by reducing the condition number of the matrix that is inverted to advance all of the fields simultaneously.

To make the equations nondimensional, we define a dimensionless variable for space and time, and then for each individual variable, as well. To begin with we set up a distance and a speed of propagation, and from these two, a dimensionless time can be found. Each of these normalizing coefficients are left as inputs in the numerical code. For example, distance can be defined as $\mathbf{r} \rightarrow r_0 \mathbf{r}'$, where $\mathbf{r}'$ is the dimensionless variable and r_0 is the normalizing coefficient, which can be chosen to be the minor radius of a tokamak, for example, or any other characteristic length scale of the plasma. Note, this study shows time as scaled by r_o divided by the speed of light. Other choices could be

to use the thermal speed, $V_S = \sqrt{\gamma \frac{P_0}{\rho_{m0}}}$, or the Alfvén speed, $V_A = \sqrt{\frac{B_0^2}{\mu_0 \rho_{m0}}}$, as desired or needed. Our definitions are as follows:

$$\mathbf{r} \rightarrow r_0 \mathbf{r}' \quad or \quad \nabla \rightarrow \frac{1}{r_o} \nabla' \,, \tag{48}$$

$$\mathbf{u} \rightarrow c\mathbf{u}' \,, \tag{49}$$

$$t \rightarrow \frac{r_0}{c} t' \,, \tag{50}$$

$$\mathbf{E} \rightarrow cB_0 \mathbf{E}' \,, \tag{51}$$

$$\mathbf{B} \rightarrow B_0 \mathbf{B}' \,, \tag{52}$$

$$T_s \rightarrow T_0 T_s' \,, \tag{53}$$

$$n \rightarrow n_0 n' \,. \tag{54}$$

Making these substitutions, the equations become:

$$\frac{c^2 B_o}{r_0} \frac{\partial \mathbf{E}'}{\partial t'} - \frac{B_o}{r_0} c^2 \left(\nabla' \times \mathbf{B}' \right) = -c n_o \sum_s \frac{e_s n_s' \mathbf{u}_s'}{\epsilon_0} \,, \tag{55}$$

$$\frac{cB_o}{r_0} \left(\nabla' \cdot \mathbf{E}' \right) = n_o \sum_s \frac{e_s n_s'}{\epsilon_0} \,, \tag{56}$$

$$\frac{cB_o}{r_0} \frac{\partial \mathbf{B}'}{\partial t'} + \frac{cB_o}{r_0} \left(\nabla' \times \mathbf{E}' \right) = 0 \,, \tag{57}$$

$$\frac{B_o}{r_0} c^2 \nabla' \cdot \mathbf{B}' = 0 \,, \tag{58}$$

$$\frac{n_0 c}{r_0} \frac{\partial n_s'}{\partial t'} + \frac{n_0 c}{r_0} \nabla' \cdot \left(n_s' \mathbf{u}_s' \right) = 0 \,, \tag{59}$$

$$\frac{c^2}{r_0} \frac{\partial \mathbf{u}_s'}{\partial t'} + \frac{c^2}{r_0} \left(\mathbf{u}_s' \cdot \nabla' \right) \mathbf{u}_s' + \frac{n_o T_o}{n_o r_0} \frac{\nabla' \left(n_s' T_s' \right)}{n_s' m_s} - cB_0 \frac{e_s}{m_s} \left(\mathbf{E}' + \mathbf{u}_s' \times \mathbf{B}' \right) = 0 \,, \tag{60}$$

$$\frac{T_o c}{r_0} \frac{\partial T_s'}{\partial t'} + \frac{T_o c}{r_0} \left(\mathbf{u}_s' \cdot \nabla' \right) T_s' + \frac{2}{3} \frac{T_o c}{r_0} T_s' \left(\nabla' \cdot \mathbf{u}_s' \right) = 0 \,. \tag{61}$$

Next, dropping the prime notation and dividing through by the leading term coefficient, we get

$$\frac{\partial \mathbf{E}}{\partial t} - \left(\nabla \times \mathbf{B} \right) = - \sum_s \frac{r_0 n_o}{cB_0} \frac{e_s n_s \mathbf{u}_s}{\epsilon_o} \,, \tag{62}$$

$$\nabla \cdot \mathbf{E} = \sum_s \frac{r_0 n_o}{cB_0} \frac{e_s n_s}{\epsilon_o} \,, \tag{63}$$

$$\frac{\partial \mathbf{B}}{\partial t} + (\nabla \times \mathbf{E}) = 0 \,, \tag{64}$$

$$\nabla \cdot \mathbf{B} = 0 \,, \tag{65}$$

$$\frac{\partial n_s}{\partial t} + \nabla \cdot n_s \mathbf{u}_s = 0 \,, \tag{66}$$

$$\frac{\partial \mathbf{u}_s}{\partial t} + (\mathbf{u}_s \cdot \nabla)\, \mathbf{u}_s + \frac{T_o}{c^2} \frac{\nabla (n_s T_s)}{n_s m_s} - \frac{r_0 B_0}{c} \frac{e_s}{m_s} (\mathbf{E} + \mathbf{u}_s \times \mathbf{B}) = 0 \,, \tag{67}$$

$$\frac{\partial T_s}{\partial t} + (\mathbf{u}_s \cdot \nabla)\, T_s + \frac{2}{3} T_s (\nabla \cdot \mathbf{u}_s) = 0 \,. \tag{68}$$

Note, only the first, second, and sixth equations have a nondimensional scaling coefficient.

Consider the last term in the first equation. Rearranging yields

$$- \sum_s \frac{r_0}{c} \frac{n_o e_s^2}{\epsilon_0 m_s} \frac{m_s}{e_s B_0} n_s \mathbf{u}_s \,, \tag{69}$$

which simplifies to

$$- \sum_s \frac{r_0}{c} \frac{\omega_{ps}^2}{\omega_{cs}} n_s \mathbf{u}_s \,. \tag{70}$$

The factor, $\frac{r_0}{c}\frac{\omega_{ps}^2}{\omega_{cs}}$, is identical for the first and second equations. Here the normalized time is $\frac{r_o}{c}$, the plasma frequency is $\omega_{ps} = \sqrt{\frac{n_o e_s^2}{\epsilon_0 m_s}}$, and the cyclotron frequency is $\omega_{cs} = \frac{e_s B_0}{m_s}$.

In the velocity advance, there are two coefficients to discuss. The first one is in front of the gradient of pressure term. Defining $T_o = m_i c^2$ makes this term go to one for the ion flow and the mass ratio for the electron flow. For the other term we split up the fraction and write

$$- \frac{r_0}{c} \frac{B_0 e_s}{m_s} (\mathbf{E} + \mathbf{u}_s \times \mathbf{B}) = -r_0 \frac{\omega_{cs}}{c} (\mathbf{E} + \mathbf{u}_s \times \mathbf{B}) = - \frac{r_0}{r_c} (\mathbf{E} + \mathbf{u}_s \times \mathbf{B}) \,, \tag{71}$$

where $r_c = \frac{c}{\omega_{cs}}$. With these definitions the dimensionless equations become

$$\frac{\partial \mathbf{E}}{\partial t} - (\nabla \times \mathbf{B}) = - \sum_s \frac{r_0}{c} \frac{\omega_{ps}^2}{\omega_{cs}} n_s \mathbf{u}_s \,, \tag{72}$$

$$\nabla \cdot \mathbf{E} = \sum_s \frac{r_0}{c} \frac{\omega_{ps}^2}{\omega_{cs}} n_s \,, \tag{73}$$

$$\frac{\partial \mathbf{B}}{\partial t} + (\nabla \times \mathbf{E}) = 0 \,, \tag{74}$$

$$\nabla \cdot \mathbf{B} = 0 \,, \tag{75}$$

$$\frac{\partial n_s}{\partial t} + \nabla \cdot n_s \mathbf{u}_s = 0 \ , \tag{76}$$

$$\frac{\partial \mathbf{u}_s}{\partial t} + (\mathbf{u}_s \cdot \nabla)\, \mathbf{u}_s + \frac{m_i}{m_s} \frac{\nabla (n_s T_s)}{n_s} - \frac{r_0}{r_c} (\mathbf{E} + \mathbf{u}_s \times \mathbf{B}) = 0 \ , \tag{77}$$

$$\frac{\partial T_s}{\partial t} + (\mathbf{u}_s \cdot \nabla)\, T_s + \frac{2}{3} T_s (\nabla \cdot \mathbf{u}_s) = 0 \ . \tag{78}$$

2.5. Dispersion relations

We have derived equations to advance the different plasma variables of interest. Important assumptions include ignoring the stress and the conductive heat flow, as well as collision terms. Note, however, we have allowed for finite electron mass, charge separation, and displacement current, which are ignored in the standard magnetohydrodynamics (MHD) model. Solving these equations, given certain initial and boundary conditions, permits careful study of the plethora of waves found in plasmas. At this point we will derive common dispersion relations to be used later when testing the code's ability to properly reproduce these waves.

2.5.1. Whistler waves

Dispersion relationships of plasma waves provide a great test of the ability of the two species model to cover both high- and low-frequency effects. To set up these waves, a constant background magnetic field is set in the z direction, $\mathbf{B_o} = (0, 0, B_o)$. We also assume there is no zeroth-order electric field or initial flows, as well as zero plasma pressure. With these assumptions, the linearized electron momentum equation is

$$\frac{\partial \mathbf{u}_{e1}}{\partial t} = \frac{e}{m_e} (\mathbf{E}_1 + \mathbf{u}_{e1} \times \mathbf{B}_0) \ . \tag{79}$$

Considering the solution vectors as plain waves, we Fourier transform in space and time and write

$$-i\omega u_{e_{1_x}} = \frac{e}{m_e} \left(E_{1_x} + u_{e_{1_y}} B_o \right) \ , \tag{80}$$

$$-i\omega u_{e_{1_y}} = \frac{e}{m_e} \left(E_{1_y} + u_{e_{1_x}} B_o \right) \ . \tag{81}$$

Solving for the flows we get

$$u_{e_{1_x}} = \frac{e}{m_e \omega} \left(-iE_{1_x} - \frac{\omega_{ce}}{\omega} E_{1_y} \right) \left(\frac{1}{1 - \frac{\omega_{ce}^2}{\omega^2}} \right) \ , \tag{82}$$

$$u_{e_{1_y}} = \frac{e}{m_e \omega}\left(-iE_{1_y} + \frac{\omega_{ce}}{\omega}E_{1_x}\right)\left(\frac{1}{1-\frac{\omega_{ce}^2}{\omega^2}}\right) . \tag{83}$$

To proceed further with this derivation, the previous two flow equations need to be substituted into Maxwell's equations. To produce the wave equation, Faraday's Law and Ampère's Law are used. Taking the curl of Faraday's Law yields

$$\nabla \times (\nabla \times \mathbf{E}) = -\frac{\partial}{\partial t}(\nabla \times \mathbf{B}) , \tag{84}$$

and substituting in Ampère's Law yields

$$\nabla \times (\nabla \times \mathbf{E}) = -\frac{\partial}{\partial t}\left(\mu_o \mathbf{J} + \mu_o \epsilon_o \frac{\partial}{\partial t}\mathbf{E}\right) . \tag{85}$$

Using vector identities to write

$$\nabla(\nabla \cdot \mathbf{E}) - \nabla^2 \mathbf{E} = -\frac{\partial}{\partial t}\left(\mu_o \mathbf{J} + \mu_o \epsilon_o \frac{\partial}{\partial t}\mathbf{E}\right) , \tag{86}$$

where $\mathbf{J} = 0 + \mathbf{J}_1$ and $\mathbf{E} = 0 + \mathbf{E}_1$, we linearize and Fourier transform in space and time to get

$$\mathbf{k} \cdot (\mathbf{k} \cdot \mathbf{E}_1) - k^2 \mathbf{E}_1 = -i\omega\mu_o \mathbf{J}_1 + \frac{\omega^2}{c^2}\mathbf{E}_1 . \tag{87}$$

Finally bringing in the assumption of transverse waves, $\mathbf{k} \cdot \mathbf{E}_1 = 0$, gives

$$-k^2 \mathbf{E}_1 = -i\omega\mu_o \mathbf{J}_1 + \frac{\omega^2}{c^2}\mathbf{E}_1 \tag{88}$$

or

$$\left(\omega^2 - k^2 c^2\right)\mathbf{E}_1 = -i\omega\mu_o c^2 \mathbf{J}_1 . \tag{89}$$

To simplify this electromagnetic wave equation, we assume the ions are immobile, thus $\mathbf{J}_1 = -n_{e_o} e \mathbf{u}_{e_1}$ can be substituted in to give

$$\left(\omega^2 - k^2 c^2\right)\mathbf{E}_1 = i\omega\mu_o c^2 n_{e_o} e \mathbf{u}_{e_1} . \tag{90}$$

Now, collecting the electron flow terms from the electron momentum equation and substituting into the previous equations yields

$$\left(\omega^2 - k^2c^2\right) E_{1_x} = \frac{\omega_{pe}^2}{1 - \frac{\omega_{ce}^2}{\omega^2}} \left(E_{1_x} - \frac{i\omega_{ce}}{\omega} E_{1_y} \right) , \tag{91}$$

$$\left(\omega^2 - k^2c^2\right) E_{1_y} = \frac{\omega_{pe}^2}{1 - \frac{\omega_{ce}^2}{\omega^2}} \left(E_{1_y} + \frac{i\omega_{ce}}{\omega} E_{1_x} \right) . \tag{92}$$

For simplicity we define $\alpha = \frac{\omega_{pe}^2}{1 - \frac{\omega_{ce}^2}{\omega^2}}$ and collect terms

$$\left(\omega^2 - k^2c^2 - \alpha\right) E_{1_x} = -\frac{i\alpha\omega_{ce}}{\omega} E_{1_y} , \tag{93}$$

and

$$\left(\omega^2 - k^2c^2 - \alpha\right) E_{1_y} = \frac{i\alpha\omega_{ce}}{\omega} E_{1_x} . \tag{94}$$

Solving these equations and replacing α yields the following relation:

$$\omega^2 - k^2c^2 - \frac{\omega_{pe}^2}{1 - \frac{\omega_{ce}^2}{\omega^2}} = \pm \frac{\omega_{ce}}{\omega} \frac{\omega_{pe}^2}{1 - \frac{\omega_{ce}^2}{\omega^2}} \tag{95}$$

or

$$\omega^2 - k^2c^2 = \frac{\omega_{pe}^2 \omega}{\omega^2 - \omega_{ce}^2} \left(\omega \pm \omega_{ce}\right) . \tag{96}$$

This dispersion relation permits two waves that propagate along the background magnetic field, $\mathbf{B}_o$, which is in the z direction. They are designated as the L and R waves, the R wave corresponding to the plus sign and the L wave to the minus sign:

$$\omega^2 - k^2c^2 = \frac{\omega_{pe}^2 \omega}{\omega - \omega_{ce}} , \qquad \text{L wave} , \tag{97}$$

$$\omega^2 - k^2c^2 = \frac{\omega_{pe}^2 \omega}{\omega + \omega_{ce}} , \qquad \text{R wave} . \tag{98}$$

A particular region of the dispersion relation for the R wave is commonly know as the Whistler mode. A convenient way of viewing these dispersion relations is by defining the index of refraction as $n = \frac{kc}{\omega}$. Making this substitution and reverting back to either species gives

$$n^2 = 1 - \sum_s \frac{\omega_{ps}^2}{\omega \left(\omega + \omega_{cs}\right)} . \tag{99}$$

In reverting back to both species, the cyclotron frequencies have different signs for ions and electrons,

thus a + sign was inserted with the realization the sign of ω_{ce} is negative, which recovers the R wave dispersion relation. At certain frequencies above the electron cyclotron frequency, the index of refraction will go to zero, when considering only the electron species. Taking this into account we solve for a cutoff frequency as

$$n^2 = 0 = 1 - \frac{\omega_{pe}^2}{\omega\left(\omega - |\omega_{ce}|\right)} \ . \tag{100}$$

Solving for this frequency yields

$$\omega_{cutoff} = \frac{|\omega_{ce}|}{2} + \sqrt{\left(\frac{\omega_{ce}}{2}\right)^2 + \omega_{pe}^2} \ . \tag{101}$$

In the region below this cutoff frequency, the index of refraction is found to be negative. This indicates the wave cannot propagate and becomes evanescent. Above the cutoff frequency, the wave behaves like it is in free space and the index of refraction tends to 1. Finally as the frequency drops below the electron cyclotron frequency, it leaves the evanescent region and becomes what is commonly known as a Whistler mode. The frequency dips down to one and then rises to the Alfvén index of refraction given by

$$n_A^2 = 1 + \sum_s \frac{\omega_{ps}^2}{\omega_{cs}^2} \ . \tag{102}$$

Numerical results will be compared to these dispersion relations in Chapter 4.

2.5.2. General MHD waves

Before leaving behind the theory section, a deeper and more general look at MHD waves would be beneficial. For a true two species plasma to behave like an MHD plasma, the frequency must be very low. In this region there are multiple waves that can be generated, of which the whistler wave is just one type. We note the fast and slow MHD waves change depending on the density, or more appropriately, on the thermal speed versus the Alfvén speed, as previously defined. The two species plasma reduces to the MHD approximation by making the assumptions listed below. Starting with a combined mass density and an averaged fluid velocity,

$$\rho_m = \sum_s \rho_{ms} \ , \tag{103}$$

$$\mathbf{U} = \frac{1}{\rho_m} \sum_s \rho_{ms} \mathbf{U}_s \ , \tag{104}$$

we use these two definitions to add the two separate continuity equations together after multiplying by their respective masses. This yields

$$\frac{\partial \rho_m}{\partial t} + \nabla \cdot (\rho_m \mathbf{U}) = 0 \, . \tag{105}$$

It can also be shown adding the separate momentum equations yields

$$\rho_m \frac{d\mathbf{U}}{dt} = \mathbf{J} \times \mathbf{B} - \nabla P \, , \tag{106}$$

where the $\frac{\mathbf{d}}{\mathbf{d}t}$ operator is defined as

$$\frac{d}{dt} = \frac{\partial}{\partial t} + (\mathbf{U} \cdot \nabla) \ . \tag{107}$$

The only other equation needed at present are the appropriate versions of Maxwell's equations, an equation of state, and an ideal Ohm's Law, namely:

$$\nabla \times \mathbf{B} = \mu_o \mathbf{J} \, , \tag{108}$$

$$\nabla \times \mathbf{E} = -\frac{\partial \mathbf{B}}{\partial t} \, , \tag{109}$$

$$\frac{d}{dt} \left(P \rho_m^{-\gamma} \right) = 0 \, , \tag{110}$$

$$\mathbf{E} = -\mathbf{U} \times \mathbf{B} \, . \tag{111}$$

With these equations, a study of low-frequency waves is possible. As has been done before, we linearize the equations by ordering the variables, letting each variable have a zeroth-order and a first-order part. As a generic example: $\mathbf{A} = \mathbf{A}_0 + \mathbf{A}_1$. Applying linearization, along with inserting Ohm's Law into Faraday's Law, as well as Ampère's Law into the momentum equation yields

$$\frac{\partial \rho_{m_1}}{\partial t} + \rho_{m_0} \nabla \cdot \mathbf{U}_1 = 0 \, , \tag{112}$$

$$\rho_{m_0} \frac{\partial \mathbf{U}_1}{\partial t} = \frac{1}{\mu_0} (\nabla \times \mathbf{B}_1) \times \mathbf{B}_0 - \nabla P_1 \, , \tag{113}$$

$$\frac{\partial \mathbf{B}_1}{\partial t} = \nabla \times (\mathbf{U}_1 \times \mathbf{B}_0) \ , \tag{114}$$

$$P_1 = \gamma \left(\frac{P_0}{\rho_{m_0}} \right) \rho_{m_1} = V_S^2 \rho_{m_1} \, , \tag{115}$$

where V_S^2 is the speed of sound defined by $V_S^2 = \gamma \frac{P_0}{\rho_{m_0}}$. Fourier transforming in space and time using $\nabla = i\mathbf{k}$ and $\frac{\partial}{\partial t} = -i\omega$ yields

$$-i\omega\rho_{m_1} + i\rho_{m_0}\mathbf{k}\cdot\mathbf{U}_1 = 0\ , \tag{116}$$

$$-i\omega\rho_{m_0}\mathbf{U}_1 = \frac{i}{\mu_0}\left(\mathbf{k}\times\mathbf{B}_1\right)\times\mathbf{B}_0 - i\mathbf{k}P_1\ , \tag{117}$$

$$-i\omega\mathbf{B}_1 = i\mathbf{k}\times\left(\mathbf{U}_1\times\mathbf{B}_0\right)\ , \tag{118}$$

$$P_1 = V_S^2\rho_{m_1}\ . \tag{119}$$

Putting the continuity equation into the equation of state will remove the first-order number density term, which can then be placed into the momentum equation to yield

$$-i\omega\rho_{m0}\mathbf{U}_1 = \frac{i}{\mu_0}\left(\mathbf{k}\times\mathbf{B}_1\right)\times\mathbf{B}_0 - i\mathbf{k}\left[V_S^2\left(\frac{\rho_{m0}}{\omega}\mathbf{k}\cdot\mathbf{U}_1\right)\right]\ . \tag{120}$$

This can be further reduced by substituting the resultant Ampère's Law into the above equation, thus solving for the perturbed flow velocity after multiplying through by $i\omega/\rho_{m0}$:

$$\omega^2\mathbf{U}_1 = \frac{1}{\mu_0\rho_{m0}}\left\{\mathbf{k}\times\left[\mathbf{k}\times\left(\mathbf{U}_1\times\mathbf{B}_0\right)\right]\right\}\times\mathbf{B}_0 + V_S^2\mathbf{k}\left(\mathbf{k}\cdot\mathbf{U}_1\right)\ . \tag{121}$$

To help understand this, and without losing generality, let $\mathbf{B}_0 = (0, 0, B_0)$ and $\mathbf{k} = (k\,sin\theta, 0, k\,cos\theta)$, where θ is the angle between $\mathbf{B}_0$ and $\mathbf{k}$. It can be shown [27] this leads to

$$\left(\frac{\omega}{k}\right)^2\begin{bmatrix}U_x\\U_y\\U_z\end{bmatrix} = V_A^2\begin{bmatrix}U_x\\U_y\,cos^2\theta\\U_z\end{bmatrix} + \begin{bmatrix}U_x\,sin^2\theta + U_z\,sin\theta\,cos\theta\\0\\U_x\,sin\theta\,cos\theta + U_z\,cos^2\theta\end{bmatrix} \tag{122}$$

with the Alfvén velocity defined as $V_A = B_0/\sqrt{\mu_0\rho_{m0}}$. This can also be written in matrix form as

$$\begin{bmatrix}v_p^2 - V_S^2\,sin^2\theta - V_A^2 & 0 & -V_S^2\,sin\theta\,cos\theta\\0 & v_p^2 - V_A^2\,cos^2\theta & 0\\-V_S^2\,sin\theta\,cos\theta & 0 & v_p^2 - V_S^2\,cos^2\theta\end{bmatrix}\begin{bmatrix}U_x\\U_y\\U_z\end{bmatrix} = 0\ , \tag{123}$$

where $v_p = \omega/k$ is the phase velocity of the wave. Taking the determinant of the matrix gives the dispersion relation

$$D(k,\omega) = \left(v_p^2 - V_A^2\,cos^2\theta\right)\left[v_p^4 - v_p^2\left(V_A^2 + V_S^2\right) + V_A^2V_S^2\,cos^2\theta\right] = 0\ . \tag{124}$$

The solutions to this dispersion relationship is the topic of the next two subsections, where we discuss the fast magnetosonic, slow magnetosonic, and transverse Alfvén modes. The solutions are listed here to complete this section before looking closer at each individual mode:

$$v_p^2 = \frac{1}{2}\left(V_A^2 + V_S^2\right) - \frac{1}{2}\left[\left(V_A^2 - V_S^2\right)^2 + 4V_A^2 V_S^2\, sin^2\theta\right]^{1/2} , \tag{125}$$

$$v_p^2 = V_A^2\, cos^2\theta , \tag{126}$$

$$v_p^2 = \frac{1}{2}\left(V_A^2 + V_S^2\right) + \frac{1}{2}\left[\left(V_A^2 - V_S^2\right)^2 + 4V_A^2 V_S^2\, sin^2\theta\right]^{1/2} . \tag{127}$$

2.5.3. Transverse wave (shear)

The transverse Alfvén or shear Alfvén mode has the simple looking solution $v_p^2 = V_A^2\, cos^2\theta$. To find the appropriate eigenvectors, we substitute the solution back into the matrix:

$$\begin{bmatrix} V_A^2\, cos^2\theta - V_S^2\, sin^2\theta - V_A^2 & 0 & -V_S^2\, sin\theta\, cos\theta \\ 0 & V_A^2\, cos^2\theta - V_A^2\, cos^2\theta & 0 \\ -V_S^2\, sin\theta\, cos\theta & 0 & V_A^2\, cos^2\theta - V_S^2\, cos^2\theta \end{bmatrix} \begin{bmatrix} U_x \\ U_y \\ U_z \end{bmatrix} = 0 . \tag{128}$$

The most convenient solution to this system of equations is $\mathbf{U}_1 = (0, U_y, 0)$. With this solution placed back into the modified Ampère's Law the solution for the perturbed magnetic field is $\mathbf{B}_1 = (0, B_y, 0)$, with $B_y = -B_0 \frac{U_y}{V_A}$ for $0 \leq \theta \leq \frac{\pi}{2}$ and $B_y = B_0 \frac{U_y}{V_A}$ for $\frac{\pi}{2} \leq \theta \leq \pi$. In a like manner, we use the ideal Ohm's Law, $\mathbf{E} = -\mathbf{U} \times \mathbf{B}$ and the perturbed electric field is found to be $\mathbf{E}_1 = (E_x, 0, 0)$, with $E_x = -B_0 U_y$. These constraints give the initial perturbation to produce the shear Alfvén wave.

2.5.4. Fast and slow MHD wave

The fast and slow MHD waves have similar origins and are best discussed together. The modes associated with fast and slow MHD waves exhibit both sound wave parts and electromagnetic parts, thus the term magnetosonic applies well to these. The general dispersion relation given by the solution to the first and third equations above are rather complex, but looking at limiting cases simplifies the matter significantly. Here $\theta = 0$ and $\theta = \pi/2$ are the two limiting cases. Taking $\theta = 0$ the matrix equation simplifies to

$$\begin{bmatrix} v_p^2 - V_A^2 & \\ & v_p^2 - V_S^2 \end{bmatrix} \begin{bmatrix} U_x \\ U_z \end{bmatrix} = 0 . \tag{129}$$

This has two solutions when $v_p^2 = V_A^2$ and $v_p^2 = V_S^2$. The trick with this solution is the fast and slow waves are determined by the relationship between the sound speed and the Alfvén speed. If the Alfvén speed is larger than the sound speed, then the fast mode is the solution $v_p^2 = V_A^2$ and the slow mode is the solution $v_p^2 = V_S^2$. When the Alfvén speed is smaller, then the modes switch.

Looking first at the case when $v_p^2 = V_A^2$, it can be shown the most convenient solution to these equations is $\mathbf{U}_1 = (U_x, 0, 0)$. With this solution placed back into the modified Ampère's Law, the solution for the perturbed magnetic field is $\mathbf{B}_1 = (B_x, 0, 0)$, with $B_x = -B_0 \frac{U_y}{V_A}$. In like manner using the ideal Ohm's Law, the perturbed electric field is found to be $\mathbf{E}_1 = (0, E_y, 0)$, with $E_y = -B_0 U_x$, with $\rho_{m_1} = 0$. Note, this is a special case that only happens when $\theta = 0$, specifically this is a transverse wave. It should be noted this could be either the fast or slow mode depending on the relationship between the Alfvén speed and the sound speed, but either way it is the solution for $v_p^2 = V_A^2$. In a similar manner the solution for $v_p^2 = V_S^2$ gives $\mathbf{U}_1 = (0, 0, U_z)$, $\mathbf{B}_1 = (0, 0, 0)$, $\mathbf{E}_1 = (0, 0, 0)$, and $\rho_{m1} = \rho_{m0}(U_z/V_S)$. This is also a special case of sound waves with density perturbations, but zero perturbed electric and magnetic fields.

The other simplification is when $\theta = \pi/2$. With this assumption the homogeneous equation becomes

$$\begin{bmatrix} v_p^2 - V_A^2 - V_S^2 & \\ & v_p^2 \end{bmatrix} \begin{bmatrix} U_x \\ U_z \end{bmatrix} = 0 \ , \tag{130}$$

which has only one root, $v_p^2 = V_A^2 + V_S^2$, giving the solution for the flow velocity $\mathbf{U}_1 = (U_x, 0, 0)$. Placing this back into the modified Ampère's Law the solution for the perturbed magnetic field gives $\mathbf{B}_1 = (0, 0, B_z)$, with $B_z = -B_0 \frac{U_x}{V_A}$. In a like manner, using the ideal Ohm's Law, the perturbed electric field is found to be $\mathbf{E}_1 = (0, E_y, 0)$, with $E_y = -B_0 U_x$, and $\rho_{m_1} = \rho_{m_0}(U_x/\sqrt{(V_A^2 + V_S^2)})$. Here it is apparent the properties exhibited have both the electromagnetic parts of the previous $v_p = V_A$ solution and the acoustic properties from the $v_p = V_S$ solution.

In Chapter 4, these different modes are benchmarked by perturbing the plasma with a spectrum of wavelengths and then performing a Fourier analysis to find the different modes that are produced. Specifically, the frequencies and their associated wave numbers are graphed and compared with results from the analytic dispersion relations presented here.

CHAPTER 3

NUMERICAL THEORY

3.1. Introduction

Before moving into the results section, a discussion of the numerical theory is needed. This chapter discusses the discretization in both time and space as used in the NIMROD [17, 28] (Non-Ideal Magnetohydrodynamics with Rotation, Open Discussion) code. Modifications were made to NIMROD to allow for the study of a resistive two fluid species model, modeling both ions and electrons with their number densities, flows, and temperatures. In addition, the electric field is advanced to facilitate the displacement current in Ampère's Law. In this chapter, we will discuss some of the finer points of the numerical methods used in this study, specifically, geometric considerations, time discretization, and the finite element implementation and their manifestation in our modified version of the NIMROD code.

3.2. Geometry

To lay the foundation for the numerical methods used in this study, reference needs to be made concerning geometry. Often, the first step in numerical solutions of partial differential equations involves choosing the grid or partitioning the computational domain. The NIMROD code has the ability to change the domain geometry to multiple configurations. The domains used in this study were rectangular slab (see Fig. 3) and cylindrical. In some cases, multiple periodic directions exist. This allows one the freedom to apply a Fourier series expansion in one of multiple directions. For example, in the periodic cylinder geometry, the Fourier direction could either run in the axial direction (circular grid, see Fig. 5) or the azimuthal direction (rectangular grid, see Fig. 4). In this study, three geometries were used, rectangular slab geometry with a rectangular grid, cylindrical geometry with a circular grid, and cylindrical geometry with a rectangular grid.

In addition there is the ability to pack the grid in areas where the fields change rapidly. In this way, areas that have little change in the data only require a few grid points, leaving more points to model the rapidly changing data. This helps to smooth out data and speed computation. Fig. 6 shows a picture of grid packing used in the rectangular and circular logical grids. Simulations that use these geometries and grid packing will be discussed in Chapter 4.

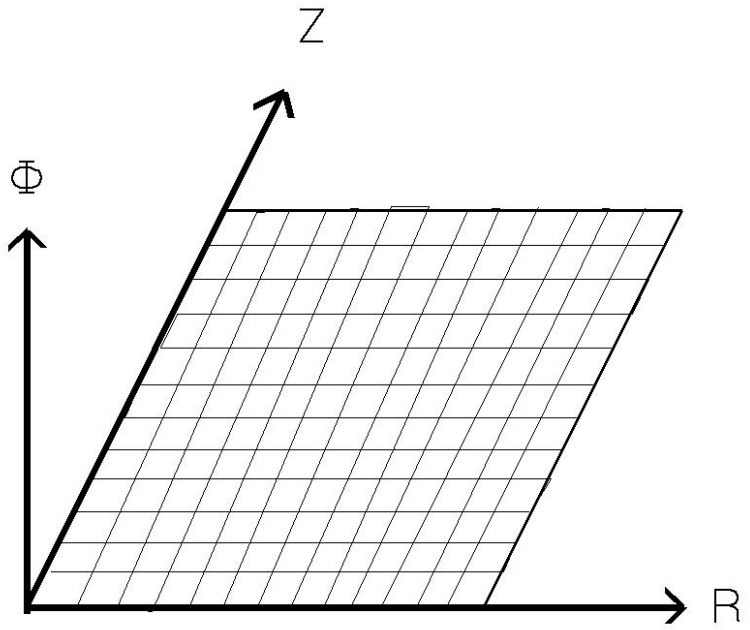

Fig. 3. Rectangular or slab geometry, with a rectangular logical grid for the variables (R,Z). The Fourier direction is vertical and periodicity is enforced over a length in the ϕ direction defined by the user.

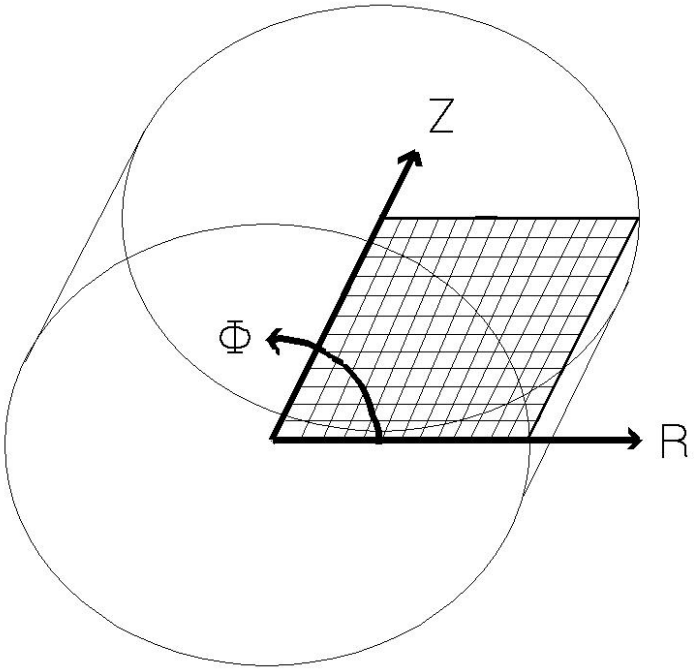

Fig. 4. Cylindrical geometry, with a rectangular logical grid for the variables (R,Z). The Fourier direction is azimuthal with periodicity being 2π.

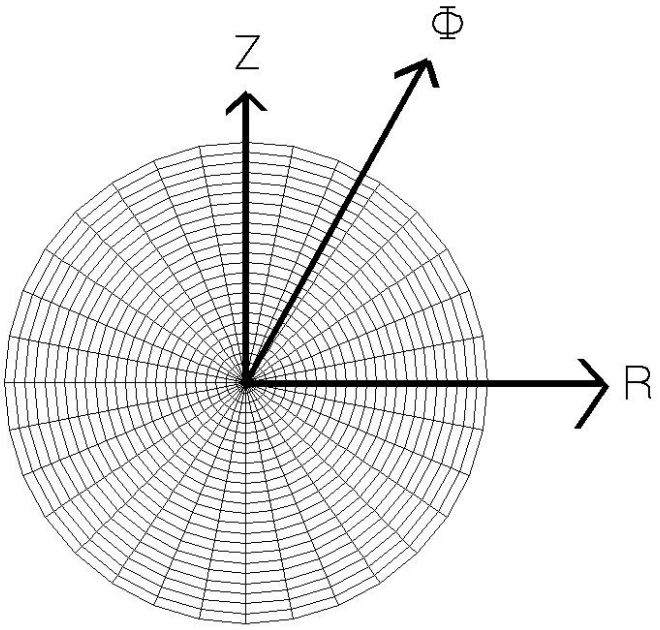

Fig. 5. Cylindrical geometry, with circular logical grid for the variables (R,Z). The Fourier direction is axial and periodicity is enforced over a length in the ϕ direction defined by the user.

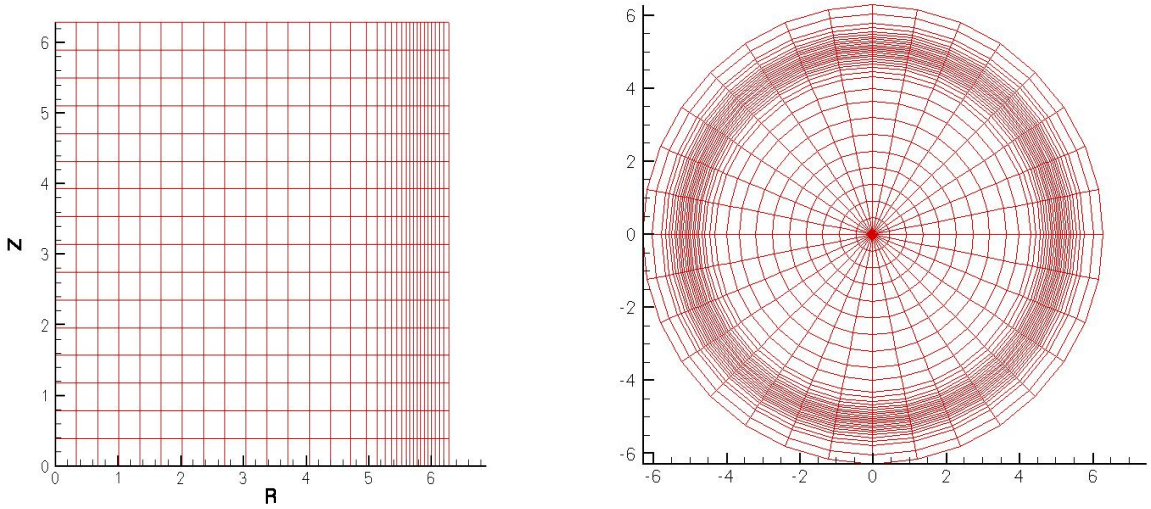

Fig. 6. Rectangular logical grid with grid packing at the edge and circular grid with grid packing near the outer edge.

3.3. Time discretization

Different numerical schemes are used to solve partial differential equations. One such scheme is the finite difference (FD) method. This method is employed by NIMROD in discretizing time. Specifically, an adjustable method is used so as to allow numerical stability, as well as speed up computation.

With the FD method, the partial derivative with respect to time of any variable in NIMROD, $\frac{\partial A}{\partial t}$, is discretized as $\frac{\Delta A}{\Delta t} = \frac{A^{k+1}-A^k}{\Delta t}$, where Δt is the discrete time step. If one wants to represent an advance based on previously determined or known variables, all of the terms (save the one being advanced) will have an explicit exponent, A^k. Rather, if one wants to represent an advance in terms of unknown variables, all of the terms will have an implicit exponent, A^{k+1}. This is especially important due to the large frequency spectrum of modes, which can by modeled by this system of equations. Implicit calculations allow for numerical stability with much larger time steps, thus allowing one to treat longer frequency modes without having to temporally resolve faster dynamics.

A centering coefficient can be used to adjust the desired amount of implicitness of any given advance. Let θ be the centering coefficient, and let it run between $0 \rightarrow 1$. Any term involving the variable, A, on either side of the equal sign can be written as $\theta L\left(A^{k+1} - A^k\right) = -L(A^k)$ or $\theta L(A^{k+1}) = -(1-\theta)L(A^k)$. In this way if $\theta = 1$, the explicit terms reside on both sides of the equation and cancel rendering the advance completely implicit. If $\theta = 0$, the implicit terms are gone and only the right side remains making the advance completely explicit. A more detailed account of the time discretization and nonlinear treatment is given in Appendix A.

3.4. Spatial discretization

The NIMROD code is three-dimensional and can address rectangular slab, periodic cylinder, and toroidal geometries. Two dimensions (R,Z) employ a 2D finite element (FE) representation, while the third is periodic and uses a Fourier representation. Specifically, NIMROD uses a pseudo-spectral method and expands the trial function in the periodic direction with a finite Fourier series, namely,

$$\mathbf{u}_s(\mathbf{x},t) = \mathbf{u}_{s,o}\left(R,Z\right) + \sum_{n=1}^{N}\left[\mathbf{u}_{s,n}(R,Z,t)e^{in\phi} + \mathbf{u}^*_{s,n}(R,Z,t)e^{-in\phi}\right] \ . \tag{131}$$

In strongly magnetized plasmas, such as tokamaks, this Fourier expansion needs only the first few terms to converge. This is because of the toroidal magnetic field strength and the symmetry it produces in the toroidal direction.. With this Fourier expansion, we need to find the coefficients $\mathbf{u}_{s,n}\left(R,Z\right)$ (s for species, n for Fourier expansion index), to achieve a solution. The coefficients

$\mathbf{u}_{s,n}(R,Z)$ are treated using the finite element method.

3.5. Finite element method

Having looked at the time discretization and Fourier representation for the periodic direction, we now discuss the spatial discretization using finite elements in the (R,Z) plane. In comparing the FD and FE methods, both convert partial differential equations into algebraic equations. The finite difference method uses a Taylor series to approximate partial derivatives as a difference between variables at discrete points divided by a discrete step in space or time. It should be noted this method effectively changes the equations being modeled, in the way it treats the partial derivatives. To obtain better accuracy, one simply reduces the steps size.

In contrast, the finite element method does not change the equation; rather, it is a method of approximating the actual solution to these equations. The finite-element method is based on a variational principle. Specifically FE truncate the solution space to a finite set of test and trial functions. Fundamentally they are very different; but put into practice, they both convert differential equations into algebraic equations.

To begin the finite element method, one defines a grid for the domain, and a partition for the problem. In 2D, this can be done with different types of cell geometries, often triangles or squares are used, but any type of polygon or shape with curvilinear sides will work. NIMROD uses triangles and rectangles; but for the purpose of this study, only rectangular cells are used. The partitioning of the domain must be defined such that all the separate partitions added together constitute the whole domain (see Figs. 3 and 5 for examples). Note, the union between any two cells is zero. This is described mathematically by writing the domain as the union of disjoint cells, namely,

$$\Omega = \bigcup_{i=1}^{N} \Omega_i \qquad \text{with} \qquad \Omega_i \cap \Omega_j = 0 \qquad \forall\ i \neq j\ . \tag{132}$$

Once this partition is set up, the solution for any particular variable can be considered. Each of these partitions is a space where one can define a function, called a trial function, such that when this function is acted upon by the differential operator, L, the result is as follows:

$$L[\mathbf{u}(\mathbf{x},t)] = 0\ . \tag{133}$$

The functions, $\mathbf{u}(\mathbf{x})$, can be sets of polynomials, for example, which are finite over only a particular cell Ω_i. In addition, a set of test functions may be defined such that the inner product of any member

of this set with the differential equations yields zero, namely,

$$\langle v(\mathbf{x}), L(u(\mathbf{x},t))\rangle = \int_\Omega d\mathbf{x} v(\mathbf{x}) L[u(\mathbf{x},t)] = 0 \ . \tag{134}$$

If this inner product, $\langle v(\mathbf{x}), L[u(\mathbf{x})]\rangle$, vanishes for every $v(\mathbf{x})$, then $u(\mathbf{x})$ is the solution to the differential equation. The trick then is finding appropriate sets of test and trial functions. Not all of them need to be found, rather just a complete basis for the specified domain. The catch is, in practice, we need to truncate the infinite sets of trial and test functions.

3.6. NIMROD expansion

Considering all of these concepts, we write the Fourier coefficients as functions of time multiplying FE basis functions, $\alpha_j(R,Z)$:

$$u_{s,n}(R,Z,t) = \sum_{j=0}^{J} u_{s,n,j}(t)\alpha_j(R,Z) \ . \tag{135}$$

Here the α_j are the basis trial function composed of Lagrange bipolynomials, and $u_{s,n,i}(t)$ is the coefficient that is ultimately solved for. The k-th order 1D Lagrange polynomials are defined as

$$l_n(x) = \prod_{0\le m\ne n\le k} \frac{x - x_m}{x_n - x_m} \ . \tag{136}$$

Lagrange bipolynomials are then simply the k^2 products of all 1D Lagrange polynomials. These are finite over one cell only in our partitioned domain. Lagrange bipolynomials are referred to as a nodal basis in that one of them takes on the value 1 at a node in the 2D cell and all the others vanish there.

By using these basis trial functions, the expansion for scalar $u(\mathbf{x})$ may be written as

$$u_s(\mathbf{x},t) = \sum_{j=0}^{J} \left\{ \alpha_j(R,Z) \left[u_{s,0,j}(t) + \sum_{n=1}^{N} \left(u_{s,n,j}(t) e^{in\phi} + u^*_{s,n,j}(t) e^{-in\phi} \right) \right] \right\} \ . \tag{137}$$

For vectors, unit vectors, $\hat{e}_l$, are introduced. For the Cartesian directions, $\hat{e}_x$, $\hat{e}_y$, and $\hat{e}_z$, and for cylindrical geometries, $\hat{e}_R$, $\hat{e}_Z$, and $\hat{e}_\phi$, we sum over the scalar expansion times the unit vectors

$$\mathbf{u}_s(\mathbf{x},t) = \sum_{j=0}^{J} \sum_{l} \left\{ \alpha_j(R,Z)\hat{e}_l \left[u_{s,0,j,l}(t) + \sum_{n=1}^{N} \left(u_{s,n,j,l}(t) e^{in\phi} + u^*_{s,n,j,l}(t) e^{-in\phi} \right) \right] \right\} \ . \tag{138}$$

This will be how all of the variables are expanded in this study. Finally after the expansions are

made over the trial basis function, a Galerkin method [11, 12] is used for the test functions, $v(\mathbf{x})$. Specifically, the complex conjugate, $e^{-in\phi}$, is used with the test functions, $\alpha_i(R,Z)$; that is, the set $v(\mathbf{x})$ has elements

$$\alpha_i(R,Z)e^{-in'\phi} \,. \tag{139}$$

With these test and trial functions in place, the products can be taken and a solution for the coefficients $u_{s,n,j}(t)$ can be found. This is done by enforcing

$$\langle v(\mathbf{x}), L(u(\mathbf{x},t))\rangle = \left\langle \alpha_i(R,Z)e^{-in'\phi}, L\left(u_{s,n,j}\alpha_j(R,Z)e^{in\phi}\right)\right\rangle = \int_\Omega d\mathbf{x}\alpha_i(R,Z)e^{-in'\phi}L[u_s(\mathbf{x},t)] = 0 \tag{140}$$

for all test functions.

In this way the partial differential equations have been changed into algebraic equations, which we solve for these coefficients. In taking this inner product, the integration over all space is needed. In doing this, a Gaussian quadrature method is used, thus turning the integrals into sums, which can be evaluated numerically. In taking these integrals, an integration by parts is sometimes used; this is referred to as the weak form of the equations. The integrated by parts form converts second derivatives into first derivatives allowing for C^0 continuity only in the finite element representation.

To demonstrate the implementation of the time discretization and 2D FE/1D Fourier expansion, the continuity equation is shown below

$$\left\langle \alpha_i \mathrm{e}^{-in'\phi}, \Delta n_s \right\rangle - \theta\Delta t \left\langle \alpha_i \mathrm{e}^{-in'\phi}, \left[\nabla\cdot\left(n_s^k\Delta\mathbf{u}_s + \Delta n_s\mathbf{u}_s^k\right)\right]\right\rangle = \Delta t \left\langle \alpha_i \mathrm{e}^{-in'\phi}, \nabla\cdot n_s^k\mathbf{u}_s^k\right\rangle \,. \tag{141}$$

Recall

$$\Delta n_s = n_s^{k+1} - n_s^k \qquad \text{and} \qquad \Delta\mathbf{u}_s = \mathbf{u}_s^{k+1} - \mathbf{u}_s^k \,. \tag{142}$$

In writing this, we need to show how to evaluate the inner products. Each of these terms is computed similarly, and it will suffice to show just one. We will explicitly state the right side following an

integration by parts:

$$\left\langle \alpha_i \mathrm{e}^{-in'\phi}, \nabla \cdot n_s^k \mathbf{u}_s^k \right\rangle = -\int_\Omega d\mathbf{x} \sum_{j=0}^{J} \sum_{m=0}^{M} \sum_l \left(\frac{\partial}{\partial \mathbf{x}} \alpha_i \mathrm{e}^{-in'\phi} \right) \cdot$$
$$\alpha_j \alpha_m \{ n_{s,0,j}^k \hat{e}_l \left[\mathbf{u}_{s,0,m,l}^k + \sum_{n=1}^{N} \left(\mathbf{u}_{s,n,m,l}^k e^{in\phi} + \mathbf{u}_{s,n,m,l}^{k*} e^{-in\phi} \right) \right]$$
$$+ \mathbf{u}_{s,0,m,l}^k \hat{e}_l \left[n_{s,0,j}^k + \sum_{p=1}^{N} \left(n_{s,p,j}^k e^{ip\phi} + n_{s,p,j}^{k*} e^{-ip\phi} \right) \right]$$
$$+ \sum_{p=1}^{N} \sum_{n=1}^{N} \hat{e}_l \big(n_{s,p,j}^k \mathbf{u}_{s,n,m,l}^k e^{i(p+n)\phi} + n_{s,p,j}^{k*} \mathbf{u}_{s,n,m,l}^{k*} e^{-i(p+n)\phi}$$
$$+ n_{s,p,j}^k \mathbf{u}_{s,n,m,l}^{k*} e^{i(p-n)\phi} + n_{s,p,j}^{k*} \mathbf{u}_{s,n,m,l}^k e^{-i(p-n)\phi} \big) \} \quad (143)$$

where $\frac{\partial}{\partial \mathbf{x}} \alpha_i \mathrm{e}^{-in'\phi} = \left(\frac{\partial \alpha_i}{\partial R} \hat{R} + \frac{\partial \alpha_i}{\partial Z} \hat{Z} - in' \alpha_i \hat{\phi} \right) \mathrm{e}^{-in'\phi}$. Note, we have assumed the surface term vanishes, which is consistent with n· normal flow into the domain boundary. The integrand is evaluated using a fast Fourier transform algorithm for the periodic direction, and the R and Z integrals are computed with Gaussian quadrature. All of the equations in this system follow the same procedure, and thus the coupled set may be cast as a set of linear equations with a matrix acting on an unknown solution vector involving Δn_s and $\Delta \mathbf{u}_s$ equally . It is noted, due to the large set of unknowns, the size of the matrix is large. However, it is a sparse matrix because of the finite element method, which makes it much more manageable.

3.7. Hyperbolic form of Maxwell's equations

In order to describe the electric and magnetic field evolution, we use Maxwell's equations. Of the four, two of them (Ampère's Law and Faraday's Law) advance the fields in time. The other two equations involve divergences of these fields. The law of no magnetic monopoles is written $\boldsymbol{\nabla} \cdot \mathbf{B} = 0$, and Poisson's equation is given as $\boldsymbol{\nabla} \cdot \mathbf{E} = \sum_s e_s n_s / \epsilon_0$. If the simulation is only an initial value problem, some consider the two advance equations to be sufficient and the divergence equations are not used. However, it has been shown [25] if the simulation is an initial-boundary value problem the divergence terms are needed to help correct numerical errors, which can creep into the solution. One way to exactly enforce the divergence properties of $\mathbf{E}$ and $\mathbf{B}$ is to introduce a scalar potential (ϕ) and a vector potential ($\mathbf{A}$) as $\mathbf{E} = -\boldsymbol{\nabla}\phi + {}^{\partial \mathbf{A}}/_{\partial t}$ and $\mathbf{B} = \boldsymbol{\nabla} \times \mathbf{A}$. This choice is referred to as the Coulomb gauge. Hakim et al. [10] have shown, however, by introducing advances for two more terms, namely, the scalar corrective potentials, ϕ and φ, the divergence properties of $\mathbf{E}$ and $\mathbf{B}$ may be satisfied to within numerical errors already present in the algorithm. This numerical approach is

the one we adopt in this work. These two terms act similar to potentials and serve the purpose of correcting the advancement of the **E** and **B** fields. Their evolution is given by

$$\frac{\partial \phi}{\partial t} + \zeta(\nabla \cdot E) = \zeta \sum_s \frac{e_s n_s}{\epsilon_0} \,, \tag{144}$$

with $\zeta c^2 \nabla \phi$ being added to Ampère's Law and

$$\frac{\partial \varphi}{\partial t} + \xi c^2 \nabla \cdot \mathbf{B} = 0 \,, \tag{145}$$

with $\xi \nabla \varphi$ being added to Faraday's Law. Note, in Faraday's and Ampère's Laws, the gradient of the corrective potentials is controlled by a scalar. Also note as $\zeta, \xi \to \infty$, Gauss's Law and $\nabla \cdot \mathbf{B} = 0$, are satisfied exactly. This can be shown by dividing the corrective potential evolution equations by their respective scalar terms, ζ, ξ, and letting those terms get very large, approaching infinity. The coefficients ζ and ξ can be thought of as a speed of propagation for these corrective potentials, which are typically set to values on the order of the speed of light. With these potentials, Maxwell's equation can be written in a purely hyperbolic form [26] as:

$$\frac{\partial \mathbf{E}}{\partial t} - c^2(\nabla \times \mathbf{B}) + \zeta c^2 \nabla \phi = -\sum_s \frac{e_s n_s \mathbf{u}_s}{\epsilon_0} \,, \tag{146}$$

$$\frac{\partial \phi}{\partial t} + \zeta(\nabla \cdot \mathbf{E}) = \zeta \sum_s \frac{e_s n_s}{\epsilon_0} \,, \tag{147}$$

$$\frac{\partial \mathbf{B}}{\partial t} + (\nabla \times \mathbf{E}) + \xi \nabla \varphi = 0 \,, \tag{148}$$

$$\frac{\partial \varphi}{\partial t} + \xi c^2 \nabla \cdot \mathbf{B} = 0 \,. \tag{149}$$

To demonstrate the purely hyperbolic nature, take the divergence of Eq. (146) and the partial time derivative of Eq. (147) to get

$$\frac{\partial^2 \phi}{\partial t^2} - (\zeta c)^2 \nabla^2 \phi = \frac{1}{\epsilon_0} \sum_s \left[\zeta \frac{\partial (e_s n_s)}{\partial t} - \nabla \cdot (e_s n_s \mathbf{u}_s) \right] \,, \tag{150}$$

which is a purely hyperbolic expression for ϕ. Similar methods applied to Eqs. (146), (147), (148), and (149) yield hyperbolic expressions for ψ, **B**, and **E**. These equations represent the first eight

variables modeled in this numerical code. We dimensionalize the corrective potentials using

$$\phi \rightarrow B_0 \phi' \ , \tag{151}$$

$$\varphi \rightarrow c B_0 \varphi' \ , \tag{152}$$

and again drop the prime notation to write the now nondimensional, purely hyperbolic from of Maxwell's equations:

$$\frac{\partial \mathbf{E}}{\partial t} - (\nabla \times \mathbf{B}) + \zeta c^2 \nabla \phi = -\sum_s \frac{r_0}{c} \frac{\omega_{ps}^2}{\omega_{cs}} n_s \mathbf{u}_s \ , \tag{153}$$

$$\frac{\partial \phi}{\partial t} + \zeta (\nabla \cdot \mathbf{E}) = \zeta \sum_s \frac{r_0}{c} \frac{\omega_{ps}^2}{\omega_{cs}} n_s \ , \tag{154}$$

$$\frac{\partial \mathbf{B}}{\partial t} + (\nabla \times \mathbf{E}) + \xi \nabla \varphi = 0 \ , \tag{155}$$

$$\frac{\partial \varphi}{\partial t} + \xi \nabla \cdot \mathbf{B} = 0 \ . \tag{156}$$

The time-discretized form for these equations uses the same method as given in section 3.3.

CHAPTER 4

NUMERICAL TESTS OF THE IDEAL TWO FLUID MODEL IN NIMROD

4.1. Electrostatic oscillations in plasmas

The first test of the two fluid implementation we present involves electrostatic oscillations in a plasma. For this problem, the set of equations is significantly simplified. We assume a cold plasma, so temperature and pressure are zero. In this test we initially used Gauss's Law coupled to a definition of electrostatic potential, as well as the equations for the advancement of number density and flow velocity

$$\nabla \cdot \mathbf{E} = \sum_s \frac{e_s n_s}{\epsilon_0} \ , \tag{157}$$

$$\mathbf{E} = -\nabla\varphi \ , \tag{158}$$

$$\frac{\partial n_s}{\partial t} + \nabla \cdot n_s \mathbf{u}_s = 0 \ , \tag{159}$$

$$\frac{\partial \mathbf{u}_s}{\partial t} + (\mathbf{u}_s \cdot \nabla)\mathbf{u}_s - \frac{e_s}{m_s}(\mathbf{E} + \mathbf{u}_s \times \mathbf{B}_0) = 0 \ . \tag{160}$$

Here $\mathbf{B}_0$ is a static, constant background magnetic field.

Before running a time-dependent simulation, we wanted to test the code's ability to compute the electrostatic potential given a static charge distribution. Several density distributions were implemented to give different charge densities, a Gaussian function, some sinusoidal functions, and a delta function. From these, the electric potential was correctly calculated and then the electric field was computed by taking the gradient of the electric potential. Figs. 7 and 8 show two of these electric potentials for Gaussian and sinusoidal charge distributions.

When the time-dependent tests were first run, we perturbed the number density for the ions and the electrons and computed the electric potential based on the charge density. From the electric potential, the electric field was found, and the velocity was advanced. Finally, the number density was advanced.

Although we thought this should have been sufficient to simulate plasma oscillations, the results were unphysical. We soon realized we needed the displacement current in Ampère's Law. Additionally, the corrective potentials were added to provide for numerical stability, as well as enforce Gauss's Law and $\boldsymbol{\nabla} \cdot \mathbf{B} = 0$. This is when we implemented the hyperbolic form of Maxwell's equations, as

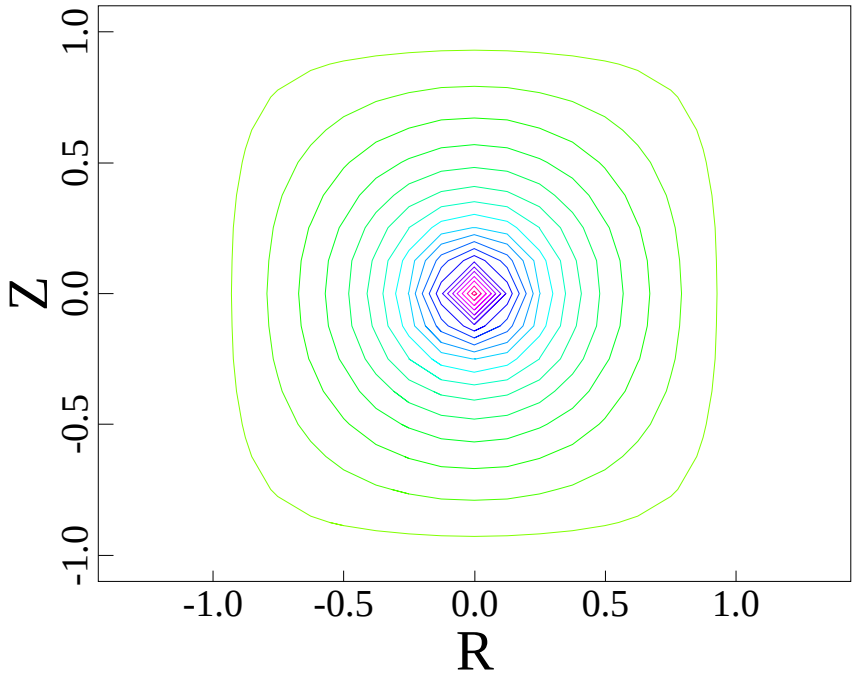

Fig. 7. Contours of electric potential calculated from a charge density that had the form of a two-dimensional Gaussian function that went to zero on the cell boundaries.

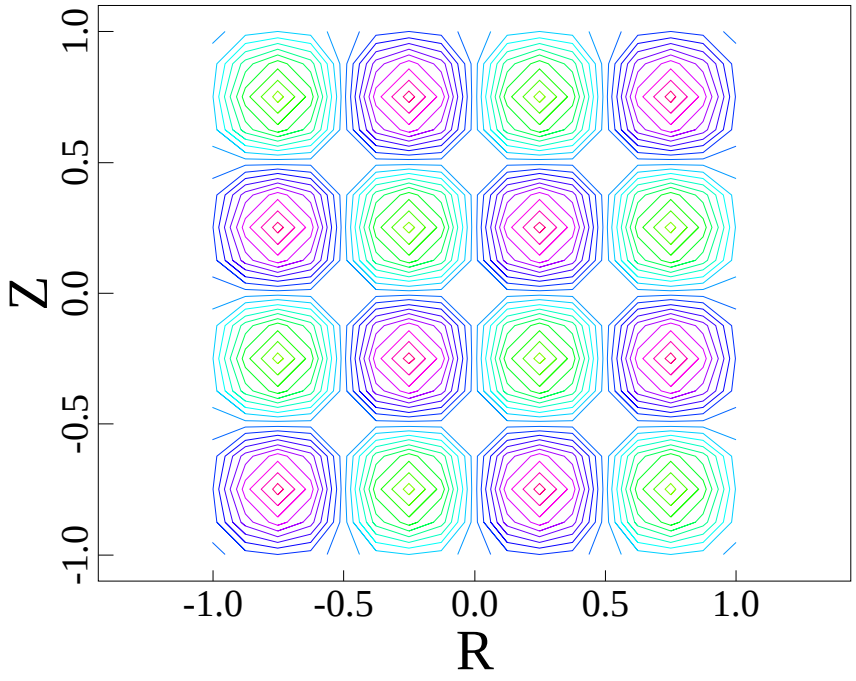

Fig. 8. Contours of the electric potential calculated from a charge density that had the form of a sinusoidal wave in both the x and y direction. Green contours represent electrostatic potential wells, while the purple represent electrosatic rises.

well as the full, zero pressure, two fluid equations, namely,

$$\frac{\partial \mathbf{E}}{\partial t} - c^2(\nabla \times \mathbf{B}) + \zeta c^2 \nabla \phi = -\sum_s \frac{e_s n_s \mathbf{u}_s}{\epsilon_0} \ , \tag{161}$$

$$\frac{\partial \phi}{\partial t} + \zeta(\nabla \cdot \mathbf{E}) = \zeta \sum_s \frac{e_s n_s}{\epsilon_0} \ , \tag{162}$$

$$\frac{\partial \mathbf{B}}{\partial t} + (\nabla \times \mathbf{E}) + \xi \nabla \varphi = 0 \ , \tag{163}$$

$$\frac{\partial \varphi}{\partial t} + \xi c^2 \nabla \cdot \mathbf{B} = 0 \ , \tag{164}$$

$$\frac{\partial \mathbf{u}_s}{\partial t} + (\mathbf{u}_s \cdot \nabla)\mathbf{u}_s - \frac{e_s}{m_s}(\mathbf{E} + \mathbf{u}_s \times \mathbf{B}_0) = 0 \ , \tag{165}$$

$$\frac{\partial n_s}{\partial t} + \nabla \cdot n_s \mathbf{u}_s = 0 \ . \tag{166}$$

With this change, the electric field was calculated correctly, and we were able to match the analytic dispersion relation for plasma oscillations. The results comparing the analytical and numerical plasma frequencies are shown in Table 1.

4.2. Acoustic wave, plasma oscillations, and finite temperature effects

Next, we simulated plasma oscillations by initializing the ion and electron velocities to vary sinusoidally in the z direction. The separation of the ions from the electrons creates an electric field, which, in turn, puts a restoring force on the number densities, causing them to flow back. The frequency of this cycle was the quantitative value, which could be tested against analytical results. To measure the frequency, a graph of energy versus time was used. Here we provide a derivation of the oscillation frequency from the standing wave that is set up. We begin by writing the plasma flow in the z direction as a standing wave, namely,

$$\begin{aligned} u_z(z,t) &= A[sin(kz - \omega t) + sin(kz + \omega t)] \\ &= 2Asin(kz)cos(\omega t) \ . \end{aligned} \tag{167}$$

Taking the derivative with respect to time

$$\dot{u}_z = -\omega 2Asin(kz)sin(\omega t) \ , \tag{168}$$

and then forming the kinetic energy density yields

$$\frac{1}{2}m\dot{u}_z^2 = mn\omega^2 A^2 sin^2(kx)sin^2(\omega t) \ . \tag{169}$$

Finally, using the identity $sin^2(\omega t) = \frac{1}{2}(1 - cos(2\omega t))$ we have

$$\frac{1}{2}m\dot{u}_z^2 = mn\omega^2 A^2 sin^2(kx)\frac{1}{2}\left[1 - cos(2\omega t)\right] \ , \tag{170}$$

which shows the kinetic energy density oscillates at twice the frequency of the standing wave. With this, the plasma oscillation frequency is found from the energy oscillation frequency. For two species, the plasma frequency is calculated analytically as

$$\omega_p = \sqrt{\omega_{pi}^2 + \omega_{pe}^2} \ , \tag{171}$$

where $\omega_{ps} = \sqrt{\frac{n_s e^2}{\epsilon_0 m_s}}$. To give an idea of the value of the ion, electron, and total plasma frequency we use $n_s = 1 \times 10^{20}$, which yields

$$\omega_{pi} = 1.48200647 \times 10^9 \ , \qquad \omega_{pe} = 8.97866371 \times 10^{10} \ , \qquad \omega_p = 8.97988672 \times 10^{10} \ . \tag{172}$$

Note, although the ion plasma frequency is small, it makes a measurable contribution to the total plasma frequency; and hence, this is a good test of numerical accuracy. For comparison, the numerical value we obtained by running with the same number density was

$$\omega_p = 8.97988648 \times 10^{10} \ , \tag{173}$$

which agrees up to the seventh digit, at this density. Thus, the effects of the ions are accounted for and the plasma oscillation mode is physically accurate. A list of other numerical and analytical values for the plasma frequency at different densities is shown in Table 1 and a graphical representation is given in Fig. 9. Pressure effects modify the plasma frequency and produce a new wave called the acoustic mode. When $\beta = 0$, the acoustic wave is equivalent to the plasma oscillation mode.

4.3. Time advance effects

At this point, we discuss the effect decreasing the time step has on calculating the plasma frequency. Recall the analytic plasma frequency is 8.97988×10^8. This makes the period $1.1136 \times$

Table 1. A comparison of analytical and numerical plasma frequencies at different number densities.

Number density	Analytical ω_p	Numerical ω_p
1×10^{16}	$8.9798867199 \times 10^{8}$	8.97988613×10^{8}
1×10^{17}	$2.8396895165 \times 10^{9}$	2.83968933×10^{9}
1×10^{18}	$8.9798867199 \times 10^{9}$	$8.97988290871 \times 10^{9}$
1×10^{19}	$2.8396895165 \times 10^{10}$	$2.8396893288 \times 10^{10}$
1×10^{20}	$8.9798867199 \times 10^{10}$	$8.97988290829 \times 10^{10}$
1×10^{21}	$2.8396895165 \times 10^{11}$	$2.8396893287 \times 10^{11}$
1×10^{22}	$8.9798867199 \times 10^{11}$	$8.97988290828 \times 10^{11}$
1×10^{23}	$2.8396895165 \times 10^{12}$	$2.8396893285 \times 10^{12}$
1×10^{24}	$8.9798867199 \times 10^{12}$	$8.97988290828 \times 10^{12}$

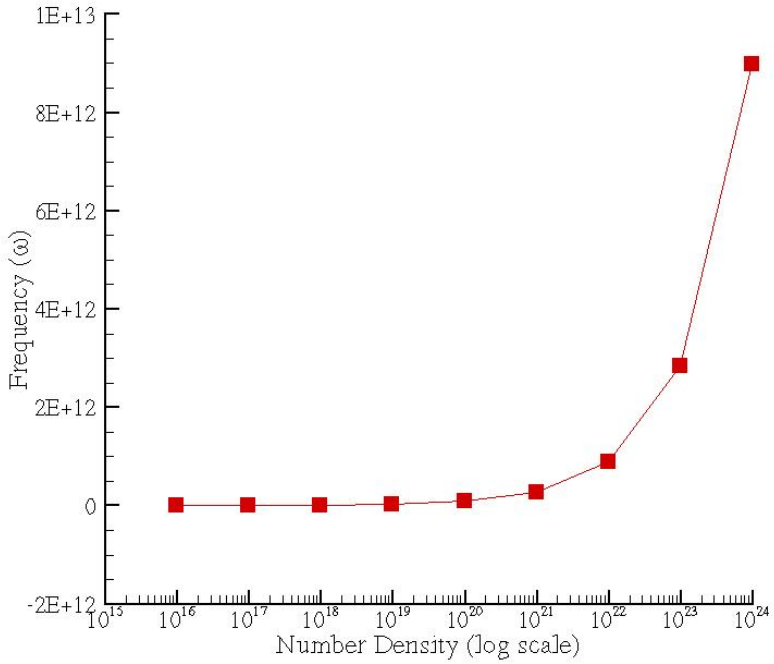

Fig. 9. Plasma frequency versus number density shows the appropriate $\sqrt{n_s}$ dependence.

10^{-11}. Fig. 10 shows the step size as percentages of this period, as well as the percent error from the analytical solution for $\theta = 0.5$ runs, fully explicit runs ($\theta = 0.0$), and fully implicit runs ($\theta = 1.0$). Recall θ is our centering parameter for all terms in our equations.

As a point of interest, one can look at the effects of the implicit verses explicit advance by looking at the total energy of the system. Analytically the energy is conserved, but if one runs this experiment with a fully explicit scheme, the energy increases slightly. If it is run with a fully implicit scheme, the energy decreases slightly with errors decreasing linearly as Δt. For $\theta = 0.5$, the energy conservation is much more accurate, as shown in Fig. 11, and errors scale as $(\Delta t)^2$. The scaling of error with Δt versus Δt^2 is tied to using a first- versus second-order time discretization.

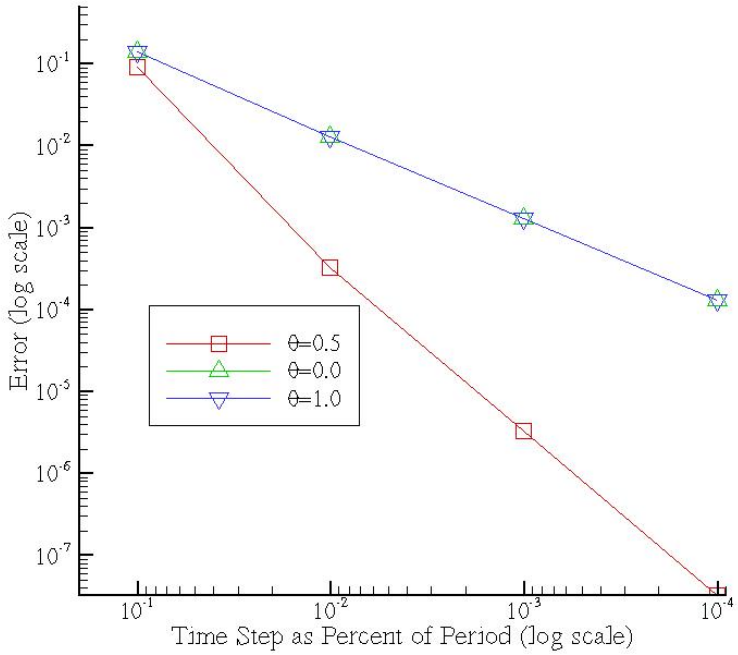

Fig. 10. Convergence of the numerical solution as the time step is decreased. Both axes are in log scale. It can be seen the slope of the fully implicit and fully explicit advances indicates a linear convergence in Δt, while the slope of the $\theta = 0.5$ indicates quadratic convergence with Δt^2.

4.4. Effects of temperature on plasma frequency

Another good demonstration of the versatility of the ideal two fluid model is to test the effects of temperature on plasma oscillations, i.e. the acoustic mode. Temperature advances were added to the other equations and the gradient of number density times pressure was added to the velocity advances.

Before presenting numerical results, we discuss the analytics of electron plasma waves with temperature effects. Using perturbation theory on the continuity, momentum, temperature (pressure), and Poisson's equations, and assuming plane wave solutions in 1-D results in

$$(-i\omega)n_{e_1} + n_{e_0} iku_{e_1} = 0 \ , \tag{174}$$

$$m_e n_{e_0}(-i\omega)u_{e_1} = -n_{e_0} eE_1 - ikp_{e_1} \ , \tag{175}$$

$$p_{e_1} = m_e \gamma_e C_e^2 n_{e_1} \ , \tag{176}$$

$$ikE_1 = -\frac{en_{e_1}}{\epsilon_0} \ , \tag{177}$$

where $C_s = \sqrt{\frac{\kappa T_{s0}}{m_s}}$ is the thermal speed of species s, and γ_s is ratio of specific heat capacity of

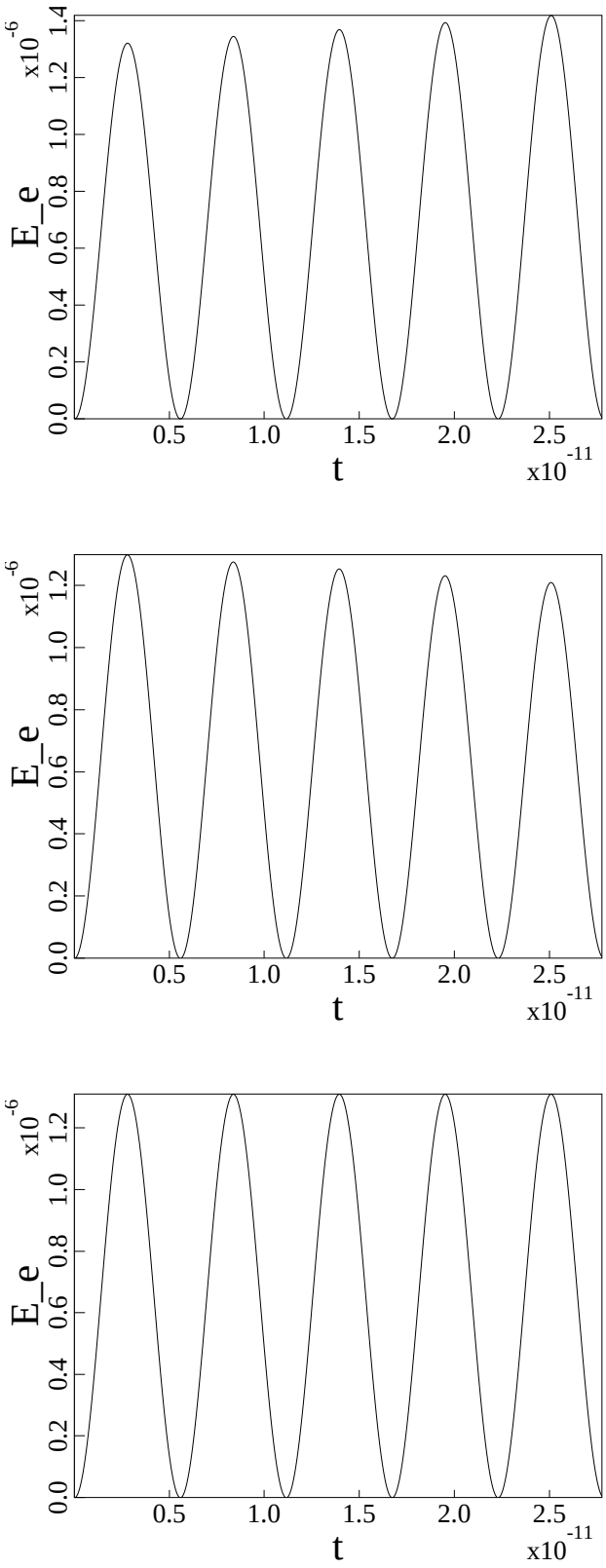

Fig. 11. Electric field energy for fully explicit ($\theta = 0$), fully implicit ($\theta = 1$), and $\theta = 0.5$ calculations showing improved energy conservation in the second order, $\theta = 0.5$ case.

species s at constant pressure to that at constant volume. This is determined by the number of degrees of freedom as $\gamma_s = \frac{f+2}{f}$, where f is the number of degrees of freedom, thus $\gamma_s = 5/3$ for $f = 3$. With these four equations, one can substitute the first, third, and last into the second and pull out the remaining common factor n_{e_1} to get

$$n_{e_1}[-\omega^2 + k^2\gamma_e C_e^2 + \omega_{pe}^2] = 0 \; . \tag{178}$$

Solving for the frequency of this electron plasma wave and using $\omega_{pe}\lambda_{De} = C_e$, where the Debye length is defined as $\lambda_{De} = \sqrt{\frac{\epsilon_0 \kappa T_0}{n_{e_0} e^2}}$ gives the following dispersion relation

$$\omega^2 = \omega_{pe}^2(1 + \gamma_e \lambda_{De}^2 k^2) \; . \tag{179}$$

If the temperature is very low, the Debye length is small and the frequency follows the plasma frequency. In contrast, if the temperature gets very large the phase velocity follows the thermal velocity as

$$\frac{\omega}{k} \simeq \sqrt{\frac{\gamma_e \kappa T_e}{m_e}} \; . \tag{180}$$

To demonstrate the results of this test, Table 2 shows the comparison of the analytical values to that of the numerical results. The results are also presented as a graph of ω versus k. When the wave number approaches one over the Debye length, $k \approx 1/\lambda_{De}$, the frequency follows the thermal velocity relationship shown above. This is shown in Fig. 12 where the numerical results curve away from the line $\sqrt{\frac{\gamma_e \kappa T_e}{m_e}}$ toward the plasma frequency in the limit of no temperature/pressure effects.

4.5. Grid refinement

In doing finite element analysis, the representation of the solution may be refined using different methods: h-type, p-type, or a combination of both. The h-type refinement is a grid refinement that reduces the size of the grid cells, whereas the p-type increases the order of the polynomials in the underlying representation. In general p-type refinement leads to faster convergence. In addition, we have observed with our code, using p-type refinement does not slow the computation time down as much as h-type. For the simple case of an acoustic wave perturbation, Fig. 13 shows the acoustic mode dispersion relation is well represented by several different grid sizes and polynomial degrees.

Tables 3 and 4 show convergence to analytical results. Table 3 shows results for h-type grid refinement with bi-linear FE basis functions. Table 4 shows results for p-type refinement. Note how the p-type refinement converges much more quickly. Both h- and p-type grid refinements had a time

Table 2. Comparison of analytical and numerical results of pressure effects on acoustic mode frequency with percent error.

Wave number	Analytical ω_p	Numerical ω_p	Percent Error
1×10^{-15}	$8.9802070460 \times 10^{10}$	$8.9801813151 \times 10^{10}$	2.87×10^{-4} %
1×10^{-14}	$8.9830897681 \times 10^{10}$	$8.9830506077 \times 10^{10}$	4.36×10^{-4} %
1×10^{-13}	$9.0118630377 \times 10^{10}$	$9.0116938990 \times 10^{10}$	1.88×10^{-3} %
1×10^{-12}	$9.2936636163 \times 10^{10}$	$9.2933064182 \times 10^{10}$	3.84×10^{-3} %
5×10^{-12}	$1.04589519956 \times 10^{11}$	$1.04540235871 \times 10^{11}$	4.71×10^{-2} %
1×10^{-11}	$1.17542737544 \times 10^{11}$	$1.17452929814 \times 10^{11}$	7.64×10^{-2} %
5×10^{-11}	$1.91924242523 \times 10^{11}$	$1.91677522857 \times 10^{11}$	0.129 %
1×10^{-10}	$2.56140956818 \times 10^{11}$	$2.55785544032 \times 10^{11}$	0.139 %
1×10^{-9}	$7.63859498610 \times 10^{11}$	$7.62747886967 \times 10^{11}$	0.146 %
1×10^{-8}	$2.40056589067 \times 10^{12}$	$2.397017110946 \times 10^{12}$	0.148 %
1×10^{-7}	$7.586475544878 \times 10^{12}$	$7.575053140397 \times 10^{12}$	0.151 %
1×10^{-6}	$2.398902993387 \times 10^{13}$	$2.395457926161 \times 10^{13}$	0.144 %
1×10^{-4}	$2.398886358593 \times 10^{14}$	$2.395406466287 \times 10^{14}$	0.145 %
1×10^{-2}	$2.398886192245 \times 10^{15}$	$2.395338979054 \times 10^{15}$	0.149 %
1	$2.398886190582 \times 10^{16}$	$2.395338977393 \times 10^{16}$	0.148 %

Table 3. Convergence to the analytical solution by refining the grid size, namely, h-type refinement.

Grid size	8×8	16×16	24×24	32×32
Poly Deg	1	1	1	1
Solution	2.55602×10^{11}	2.56111×10^{11}	2.5613636×10^{11}	2.561399×10^{11}
Error	1.996×10^{-1}	1.199×10^{-2}	1.1999×10^{-3}	2.307×10^{-4}

step that is 0.001 % of the analytic frequency, so it would be resolved in time, as well as in space. For comparison, this case has an analytic frequency of $2.56141483772 \times 10^{11}$ with $\theta = 0.5$ centering for added accuracy.

4.6. Electromagnetic wave test

As another test, we set number density very low in order to initialize electromagnetic waves propagating through free space. As expected, the observed speed of the counter propagating electric and magnetic fields making up the standing waves is found to be the speed of light. The results of

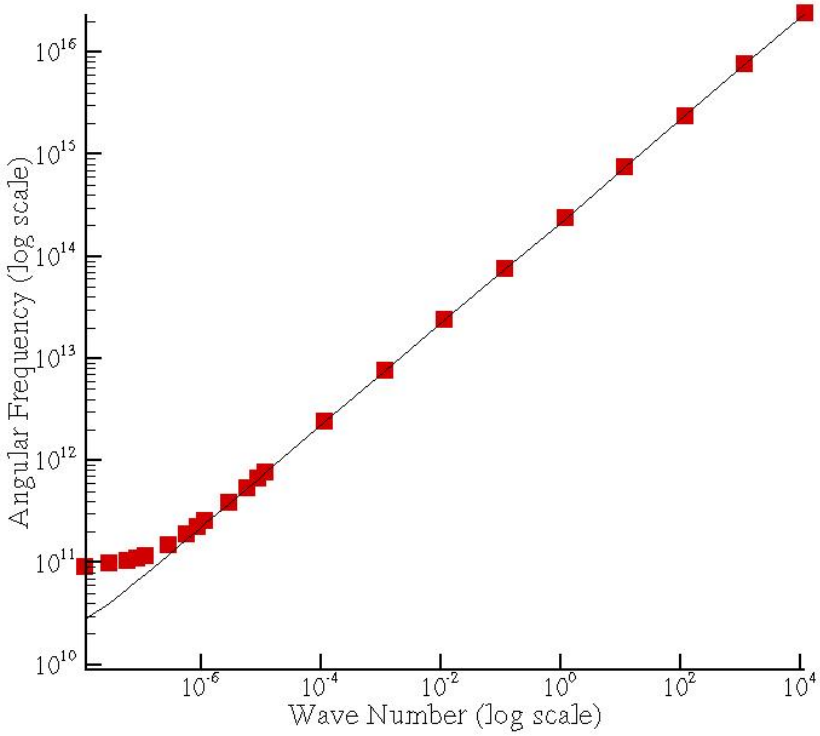

Fig. 12. Graphical representation of Table 2. Note the slope of this line is $\sqrt{\frac{\gamma_e \kappa T_e}{m_e}}$, which is proportional to the thermal speed. For high wave numbers, the numerical data scales as $\sqrt{T_e}$, as expected.

Table 4. Convergence to the analytical solution by refining the polynomial degree, namely, p-type refinement.

Grid size	8×8	8×8	8×8	8×8
Poly Deg	1	2	3	4
Solution	2.55602×10^{11}	2.5612196×10^{11}	$2.56141483 \times 10^{11}$	$2.5614148379 \times 10^{11}$
Error	1.996×10^{-1}	7.99×10^{-3}	7.068×10^{-8}	9.047×10^{-9}

adjusting the wave number and monitoring the change in the frequency are shown in Fig. 14. The slope of the ω versus k curve is the speed of light, $\omega/k = c$.

4.7. Whistler waves

In Chapter 2 we derived the dispersion relationship for the whistler mode. Reproducing this dispersion relationship is a good test of the code's ability to reproduce both high- and low-frequency

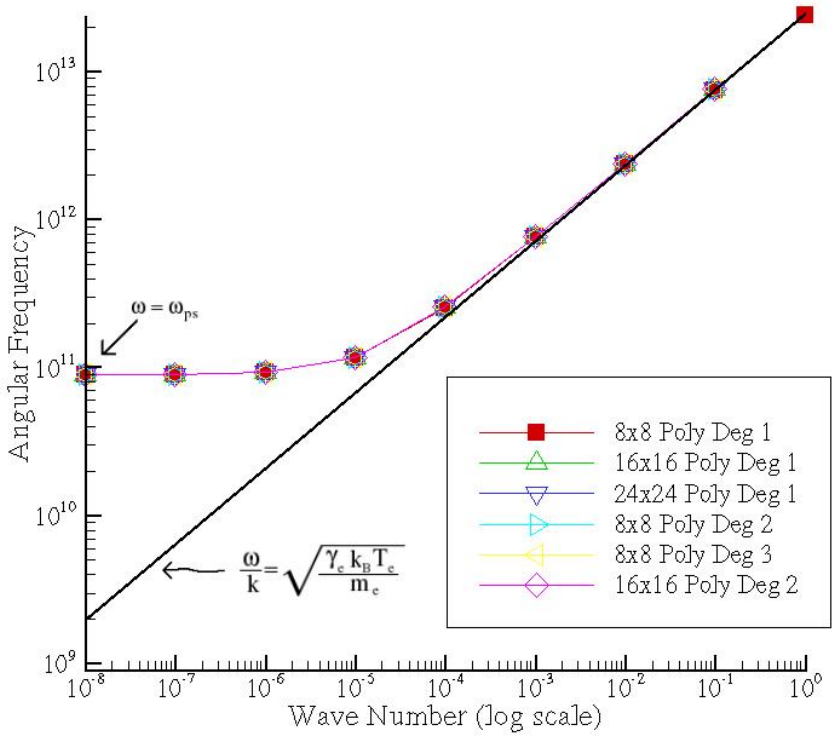

Fig. 13. A blown up portion of the acoustic mode dispersion relation to highlight the effect of temperature on plasma frequency. Note all of the various FE representations match the analytical value remarkably well.

effects in the two species model. Recall the dispersion relations for the L and R waves

$$\omega^2 - k^2c^2 = \frac{\omega_{pe}^2\omega}{\omega - \omega_{ce}} \ , \qquad \text{L wave} \tag{181}$$

$$\omega^2 - k^2c^2 = \frac{\omega_{pe}^2\omega}{\omega + \omega_{ce}} \ . \qquad \text{R wave} \tag{182}$$

A particular region of the dispersion relation for the R wave is commonly known as the Whistler mode. A convenient way of viewing these dispersion relations is by defining the index of refraction as $n = \frac{kc}{\omega}$. Making this substitution and considering electrons, the index of refraction is found to be

$$n^2 = 1 - \frac{\omega_{pe}^2}{\omega(\omega - |\omega_{ce}|)} \ . \tag{183}$$

Note, the frequency exhibits a cutoff value where $n = 0$:

$$\omega_{cutoff} = \frac{|\omega_{ce}|}{2} + \sqrt{\left(\frac{\omega_{ce}}{2}\right)^2 + \omega_{pe}^2} \ . \tag{184}$$

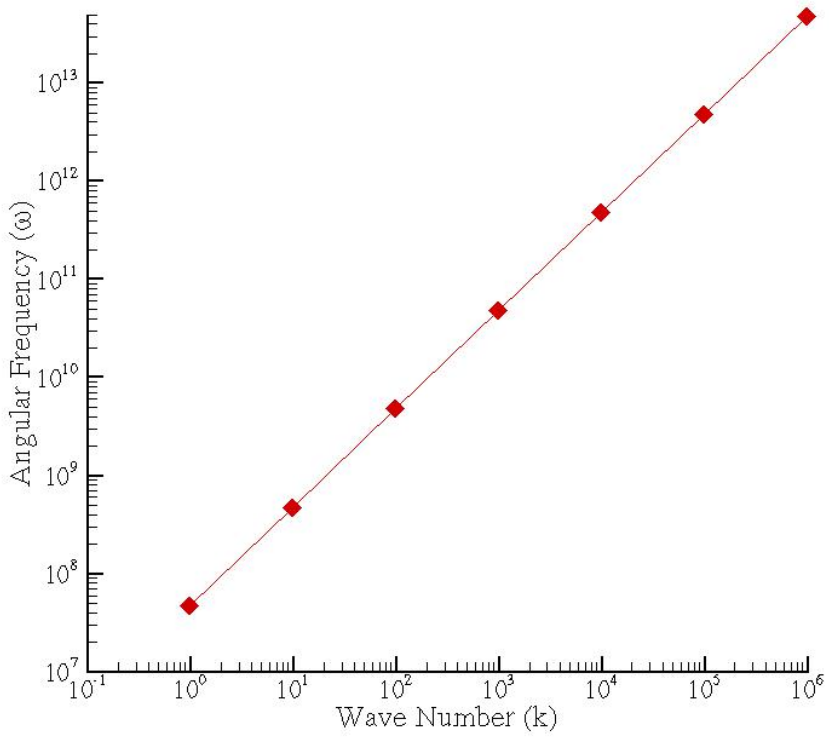

Fig. 14. Angular frequency, ω, verses wave number, k, for light waves. With numerical results (diamonds) plotted over the analytical dispersion curve (line). Note the slope of the line is the speed of light, $\omega/k = c$.

In the region below this cutoff frequency, the index of refraction is found to be negative. This indicates the wave cannot propagate and becomes evanescent. Above the cutoff frequency, the wave behaves like it is in free space and the index of refraction tends to one. Finally, as the frequency drops below the electron cyclotron frequency, it leaves the evanescent region and becomes what is commonly known as a Whistler mode. The frequency dips down to 1 and then rises to the Alfvén index of refraction given by

$$n_A^2 = 1 + \sum_s \frac{\omega_{ps}^2}{\omega_{cs}^2} \; . \tag{185}$$

To initialize the whistler mode, the electric field is perturbed in a right-handed sense with respect to the background magnetic field, such that $E_x = E_o cos(kzt)$ and $E_y = E_o sin(kzt)$, with z being the direction of propagation. As was mentioned, low frequencies yield a result that the index of refraction approaches the Alfvén limit. This only happens when the plasma is electrically neutral and at low frequencies, i.e., when the plasma species oscillate in an MHD fashion. To insure this behavior, the perturbation of the plasma using the electric field needs to be balanced with the magnetic field,

$\mathbf{B}_1 = \mathbf{k} \times \mathbf{E}_1/\omega$. Thus $B_y = k/\omega E_o cos(kzt)$ and $B_x = -k/\omega E_o sin(kzt)$. This produces the desired results, which are demonstrated in Fig. 15. Fig. 16 shows a close up near the electron cyclotron resonance, $\omega = \omega_{ce}$. Notice the result of the wave frequency, ω, at the electron cyclotron frequency, as well as the evanescent region from $\omega_{ce} < \omega < \omega_{cuttoff}$, and finally as the frequency increases, the refractive index tends to one.

4.8. MHD waves more general

As noted, the whistler wave is only one of a many waves that can be found in a plasma. The theory section described other MHD-type waves: transverse, fast, and slow magnetosonic. Instead of finding the exact initialization of each of these waves, which requires knowing the solution to the coupled partial differential equations before it is computed, a Fourier analysis is used to find the dispersion curves of each of these types of waves. How we accomplish this is the subject of the next section.

First, we note the analytical relationships for these waves. In the limit of low temperatures, the fast magnetosonic mode corresponds to the whistler mode or the R mode noted in the previous

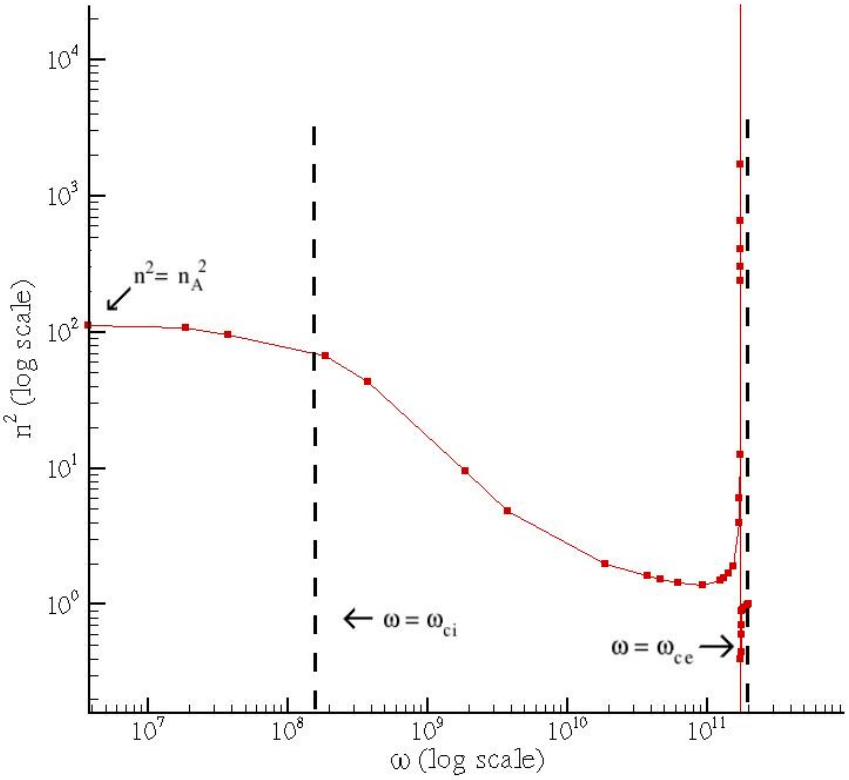

Fig. 15. The index of refraction versus the oscillation frequency, n^2, vs. ω. Due to the range in frequencies, it does not show details near $\omega = \omega_{ce}$. Note the code (squares) accurately reproduces the dispersion relation over six decades of frequency.

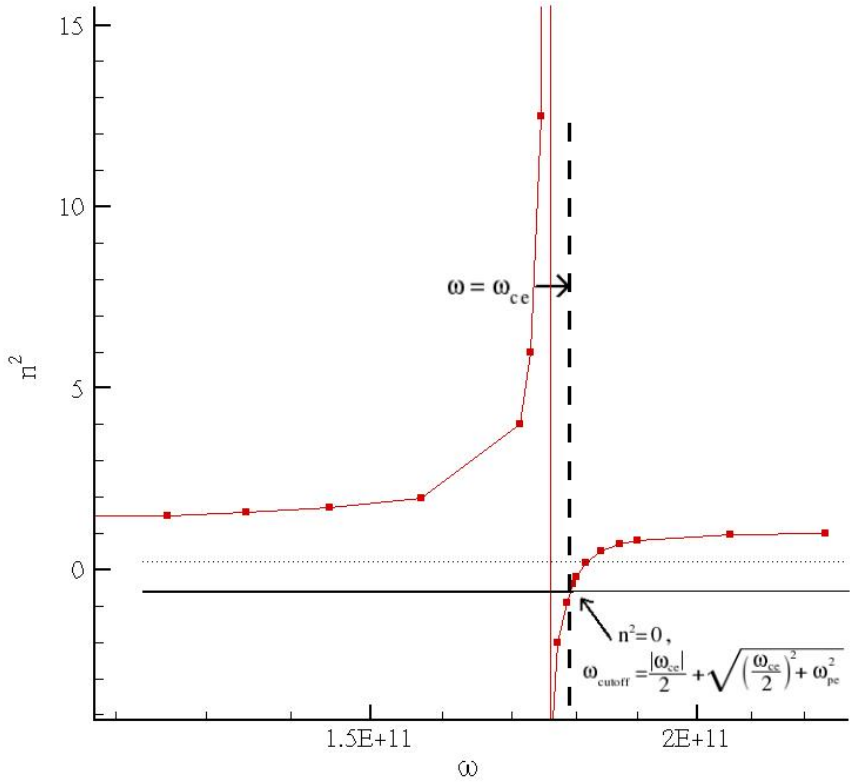

Fig. 16. The whistler mode shows a close-up view of the evanescent region, $\omega_{ce} < \omega < \omega_{cutoff}$, the electron cyclotron resonance, $\omega = \omega_{ce}$, and the free space electromagnetic propagation behavior, $\omega \gg \omega_{cutoff}$.

section and the transverse wave corresponds to the L mode. These waves are based upon the relationship between the Alfvén velocity and the speed of sound:

$$V_A = \frac{B_0}{\sqrt{\mu_0 n_0 m_0}} \,, \tag{186}$$

$$V_S = \sqrt{\frac{\gamma T_0}{m_0}} \,, \tag{187}$$

where B_0, T_0, and n_0 are the background magnetic field strength, temperature, and number density, respectively. Also μ_0 is the permeability of free space and m_0 is the average species mass. Finally, γ is the index that is tied to the number of degrees of freedom. In the case of an adiabatic pressure response, $\gamma = 5/3$.

Depending on the orientation of the wave vector, $\mathbf{k}$, and the background magnetic field, $\mathbf{B}_0$, the different MHD waves have phase velocities V_A, V_S, $\sqrt{V_A^2 + V_S^2}$, or 0.

4.9. Fourier analysis

The previous sections have shown specific waves can be excited by specifying initial conditions consistent with the individual modes. In another approach, a large number of modes with different frequencies can be generated simultaneously in a single simulation. This is done by initializing a spatially localized perturbation, and then performing a Fourier analysis to determine the different frequencies and wave numbers that arise. These are associated with the various plasma modes we have discussed to this point. The perturbation was chosen as a spatially localized Gaussian function in the ion and electron velocity. Fig. 17 shows the progression of the perturbation through the plasma. Note the periodic boundary conditions. Fig. 18 shows the same wave proceeding through

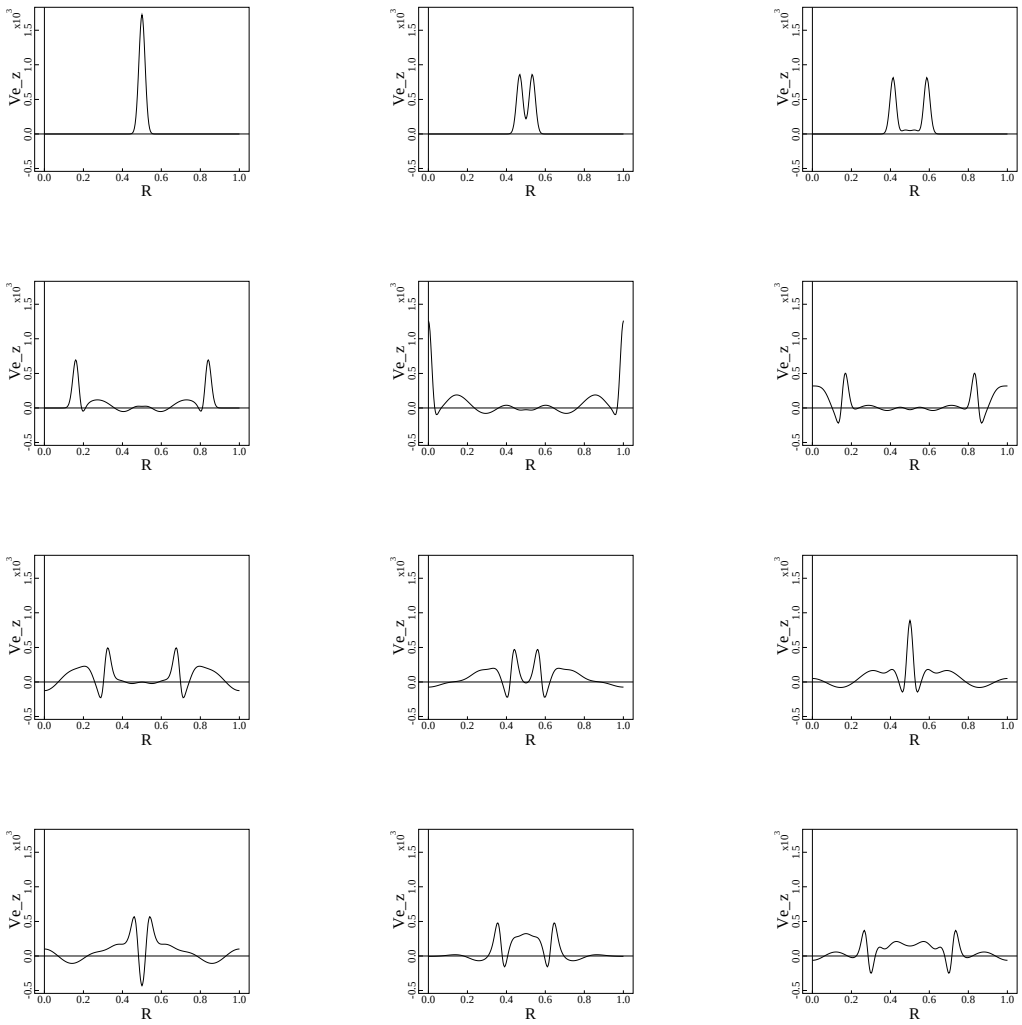

Fig. 17. The initiation and the progression of a sharp Gaussian function, which initializes many different plasma waves evolving in time. The timeline of these graphs goes from left to right, top to bottom.

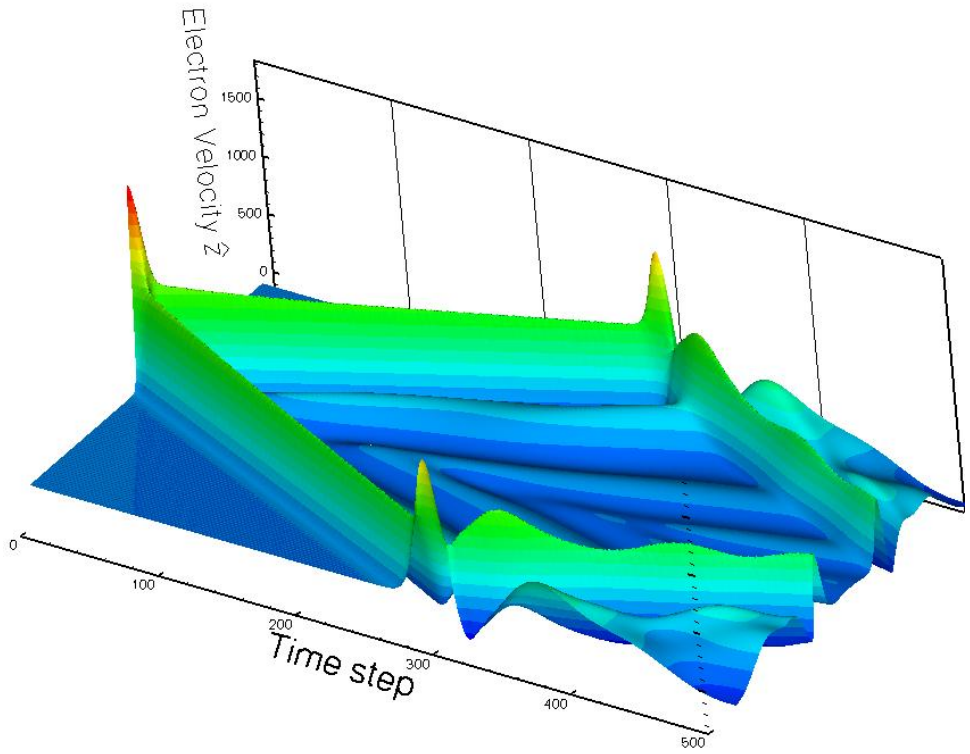

Fig. 18. The same Gaussian function perturbation as in Fig. 17 in a three-dimensional representation. The wave is initialized on the left side of the graph and it proceeds to the right. For ease of viewing, this wave shows fewer time steps than the previous set of figures.

the plasma as a 3D graph. In both figures one is able to see the initial perturbation excites a number of different waves with varying frequencies. The longer the wave is allowed to oscillate, the more apparent the many different modes present in the system become.

A two-dimensional Fourier analysis of these waves and their associated frequencies and wave numbers shows various dispersion relationships in the plasma. Fig. 19 shows the Fourier spectrum with high power in the red regions and low power in the blue. Overlaying Fig. 19 are the analytic results of different dispersion relations. The different modes shown here correspond to the magnetosonic, acoustic, Alfvén, and whistler waves. Each wave is listed, in the caption for Fig. 20.

4.10. Waves in periodic cylinder geometry

Each of the previous tests was done in slab geometry, with one direction modeled by a Fourier series, and the other two directions having periodic boundary conditions. Agreement with analytic dispersion relations was excellent, and this provides confidence in the model to be used for stability calculations later on.

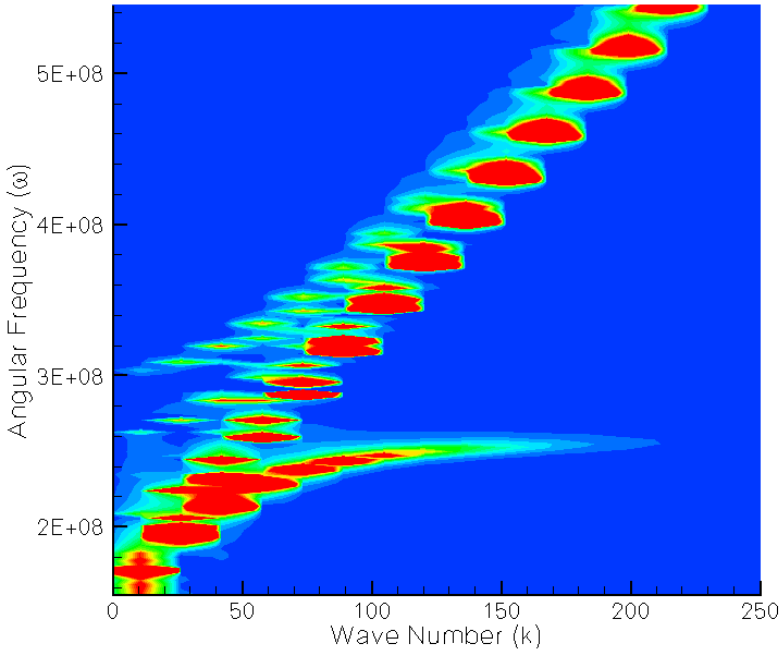

Fig. 19. Contours of the Fourier spectrum from a spatially localized perturbation, which then evolved into a suite of normal mode oscillations. Various dispersion relationships are represented simultaneously.

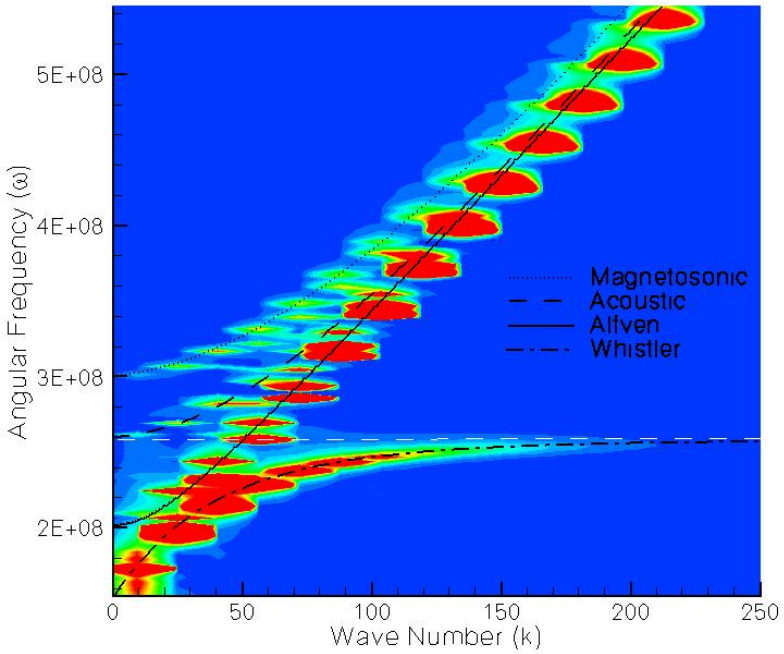

Fig. 20. The Fourier spectrum with analytical dispersion relation results overlaying the numerical contours, which indicate normal modes excited in the plasma. The plasma frequency is shown as the white dashed horizontal line. The dotted black line is the R-mode or the fast magnetosonic mode, the dashed black line is the L-mode or the acoustic mode, the solid black line is the transverse Alfvén mode, and the dot-dash line is the whistler mode.

The next step was to test plasma wave behavior in a cylindrical domain. As mentioned before, two different methods were used: a rectangular grid with an azimuthal Fourier expansion and a circular grid with an axial Fourier expansion. These grids were shown in Figs. 4 and 5.

To make these different methods comparable, similar perturbations were needed. A simple axially propagating acoustic wave was initialized for each of these geometries (see Figs. 21 and 22).

Specifically, the ion and electron velocities were perturbed in a compressional manner, and all other quantities evolved from homogeneous initial conditions. The left of Fig. 21 shows the perturbation using a rectangular grid in the R, Z plane. Bessel functions were used to initialize the radial dependence of the flow perturbations. This allowed a compressional acoustic wave to be generated in the center of the column, which satisfied homogeneous boundary conditions at the plasma boundary. Fig. 21 also shows the same perturbation on the right, using a circular logical grid in the R, Z plane with the Fourier expansion in ϕ. Bessel functions were used to create the radial dependence of the perturbation. Fig. 22 shows the comparrison of these two cylindrical perturbations along with a rectangular slab geometry. Finally, Table 5 shows the results for the three geometries compared to the analytical solution.

Table 5. Comparison of analytical and numerical results of acoustic mode dispersion relations between the three different geometries we tested. The first frequency is the analytic solution. The next case is a rectangular slab geometry, followed by the cylindrical cases. The fourth column is the case using a rectangular logical grid with the Fourier expansion in the azimuthal direction. Finally, the last column is with a circular grid and the Fourier expansion in the axial direction.

Wave number	Analytical ω_p	Rectangular ω_p	Azimuthal ω_p	Axial ω_p
1×10^{-9}	8.98620×10^{10}	8.98018×10^{10}	8.98018×10^{10}	8.97981×10^{10}
1×10^{-8}	8.98309×10^{10}	8.98307×10^{10}	8.98307×10^{10}	8.98270×10^{10}
1×10^{-7}	9.01186×10^{10}	9.01185×10^{10}	9.01185×10^{10}	9.01154×10^{10}
1×10^{-6}	9.29471×10^{10}	9.29601×10^{10}	9.29601×10^{10}	9.29521×10^{10}
1×10^{-5}	1.17548×10^{11}	1.16803×10^{11}	1.16803×10^{11}	1.17457×10^{11}
1×10^{-4}	2.56141×10^{11}	2.56160×10^{11}	2.56910×10^{11}	2.56141×10^{11}
1×10^{-2}	2.40057×10^{12}	2.40931×10^{12}	2.43901×10^{12}	2.40057×10^{12}

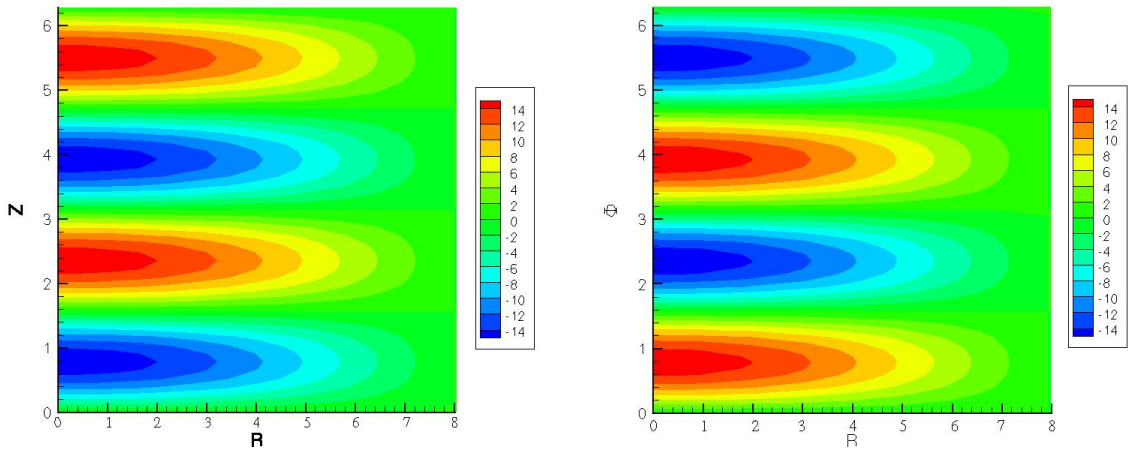

Fig. 21. The graph on the left shows the initial perturbation of the electron velocity in the Z direction. It is a case with rectangular, logical grid and azimuthal Fourier representation (geometry of Fig. 4). Note, because of the $J_0(R)$ Bessel function used for the radial dependence, the perturbation vanishes at the plasma boundary. The graph on the right shows the same initial perturbation of the electron velocity in the Φ direction for a case with circular logical grid. This also constitutes a cylindrical case, but the Fourier expansion is in the periodic, axial direction Φ.

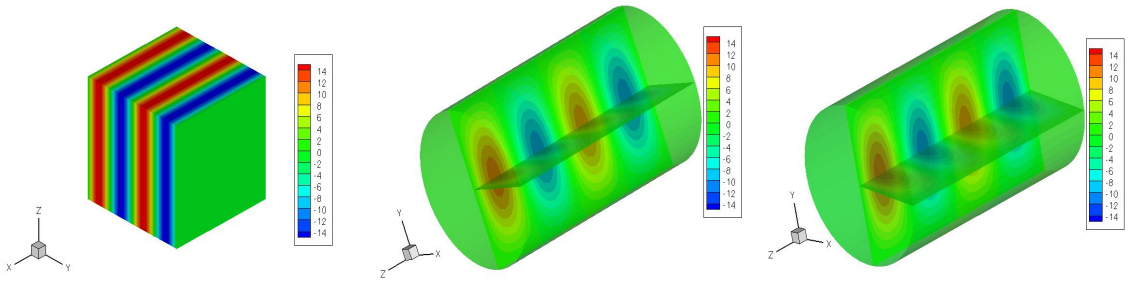

Fig. 22. The initial perturbations for all three cases, this time in a 3-D format for rectangular linear, rectangular toroidal, and circular linear geometry.

CHAPTER 5

LINEAR STABILITY TESTS

5.1. Resistive tearing modes in cylindrical geometry

In the paper done by Holmes et al. [16], the stability of resistive tearing modes using the full MHD and reduced MHD models were compared. To test our code against the results of that paper, we set up a similar configuration with the two species model by adding a resistivity term. It appears in the momentum equations and involves the difference of the electron and ion flows. For the case considered in this study, the momentum moment of the collision operator is defined specifically for species s colliding with species t as

$$m_s n_s \nu_{st} (\mathbf{u}_t - \mathbf{u}_s) \ . \tag{188}$$

Using the definition of conductivity,

$$\sigma_\perp = \frac{1}{\eta} = \frac{n_{e_o} e^2}{\nu_{ei} m_e} \ , \tag{189}$$

the collisional friction term becomes

$$\eta n_{e_o} e^2 n_e (\mathbf{u}_t - \mathbf{u}_s) \ , \tag{190}$$

where $\sigma_\perp$ is the perpendicular conductivity, η is the resistivity, and ν_{ei} is the electron-ion collision frequency. We insert these terms into the momentum equations defined previously, remembering to divide through by $n_s m_s$, as has been done for every term in these equations. Ultimately, this resistivity takes the individual forms of

$$\frac{\eta n_{e_o} e^2}{m_e} (\mathbf{u}_i - \mathbf{u}_e) \ , \ \text{and} \tag{191}$$

$$- \frac{\eta n_{e_o} e^2}{m_i} \frac{n_e}{n_i} (\mathbf{u}_i - \mathbf{u}_e) \ , \tag{192}$$

for the electron and ion flow equations, respectively. With these terms added into the velocity advances, our algorithm can represent resistive MHD type plasmas, with the additional two species physics effects.

Before moving on to the implementation of the collisional friction terms, we need to dedimensionalize them. In the NIMROD, code resistivity is defined as: $\eta = \mu_o C_{elecd}$, where C_{elecd} is an electrical

diffusivity with units of m^2/s. Noting $c^2 = 1/\mu_o\epsilon_o$ and writing resistivity as $\eta = C_{elecd}/c^2\epsilon_o$, we write the nondimensional electron and ion frictional collision terms as

$$\frac{r_o}{c}(\frac{\omega_{pe}}{c})^2 C_{elecd} n_{e_o}(\mathbf{v}_i - \mathbf{v}_e) \ , \quad \text{and} \tag{193}$$

$$\frac{r_o}{c}(\frac{\omega_{pe}}{c})^2 C_{elecd} n_{e_o}\frac{n_e}{n_i}(\mathbf{v}_i - \mathbf{v}_e) \ . \tag{194}$$

In the Holmes [16] paper, the equilibrium is set by using the MHD force balance, $\boldsymbol{\nabla} p = \mathbf{J} \times \mathbf{B}$. In addition, all quantities are cylindrically symmetric. The equilibrium was calculated by specifying the safety factor profile (which describes the pitch of the magnetic field) as $q(r) = q_0[1 + (\frac{r}{r_o})^{2\lambda}]^{1/\lambda}$. This also specifies the pressure profile as $\beta_o p_{eq}(r) = 2\epsilon^2 \int_r^1 dr' \frac{1}{q}\frac{d}{dr'}\frac{r'^2}{q}$. With these and the toroidal magnetic field set to one, $B_{\zeta_{eq}}(r) = 1$, all the information needed to calculate the equilibrium fields is given. Also important to list is the current density, $J_\zeta(r) = \frac{1}{r}\frac{d}{dr}(rB_{\theta_{eq}})$, where ζ is the toroidal direction and $B_{\theta_{eq}}$ is the azimuthal component of the magnetic field. We also note the requirement that $B_{\theta_{eq}}(r) = \epsilon_L r/q$ with q as the safety factor and ϵ_L as the inverse aspect ratio. Fig. 23 shows the azimuthal symmetry in the magnetic field in the azimuthal direction, the current density in both the azimuthal and the axial direction, as well as the pressure are plotted.

To specify the MHD equilibrium, only two of three fields, pressure, current, and magnetic field, need to be specified for force balance, and then the remaining term is computed. In a like manner, the two fluid equilibrium study uses force balance to specify the pressures, flows, and magnetic field. In equilibrium we have

$$(\mathbf{E} + \mathbf{u}_e \times \mathbf{B}) + \frac{\boldsymbol{\nabla} p_e}{e n_e} = -\frac{m_e}{e}\nu_{ei}(\mathbf{u}_e - \mathbf{u}_i) \ , \tag{195}$$

for electrons, and

$$(\mathbf{E} + \mathbf{u}_i \times \mathbf{B}) - \frac{\boldsymbol{\nabla} p_i}{e n_i} = -\frac{m_i}{e}\nu_{ie}(\mathbf{u}_e - \mathbf{u}_i) = -\frac{m_e}{e}\nu_{ei}(\mathbf{u}_e - \mathbf{u}_i) \ , \tag{196}$$

for ions, where in the last equality, we have used $\nu_{ie} = \frac{m_e}{m_i}\nu_{ei}$, which is true for this case because the equilibrium number densities are taken to be equal $n_{e_o} = n_{i_o} = n_o$. We can solve for the specific components of the flow velocities by considering the components of the momentum equation that are parallel and perpendicular to the magnetic field. In this way the cross product in these equations can be simplified.

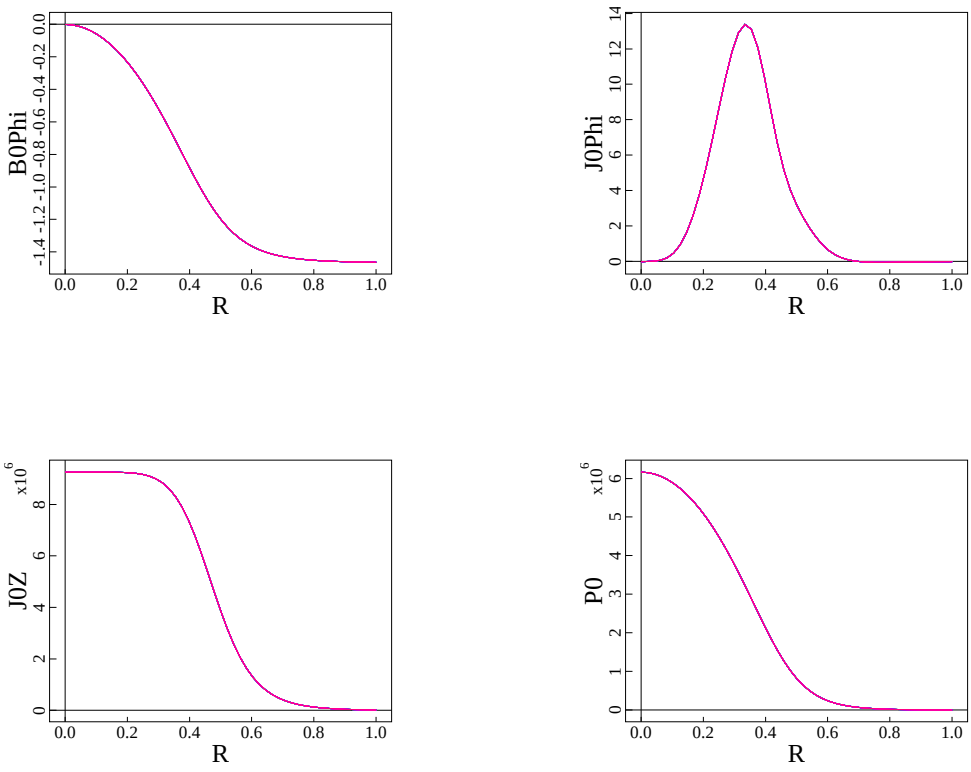

Fig. 23. The magnetic field in the azimuthal direction, the current density in the azimuthal, and axial directions, and pressure. This is shown here to compare against our codes two fluid equilibrium values.

Considering the parallel parts of the flow, we write

$$\mathbf{E}_{\|} = -\frac{m_e}{e}\nu_{ei}(\mathbf{u}_{e_{\|}} - \mathbf{u}_{i_{\|}}) \,, \tag{197}$$

where $\boldsymbol{\nabla}_{\|} p_s = 0$ arises from rapid equilibration of pressure along the magnetic field. This equality defines the parallel part of the electric field once the flows are specified. To do this, we use the definition of the current density to relate the equilibrium flows to the specified current density for the Holmes equilibrium as follows:

$$\mathbf{J}_{\|} = e n_o(\mathbf{u}_{i_{\|}} - \mathbf{u}_{e_{\|}}) \,. \tag{198}$$

As this is underspecified, we use the relationship given by conservation of momentum to solve for the two flows, namely, $m_e \mathbf{u}_{e_{\|}} = m_i \mathbf{u}_{i_{\|}}$. This gives the two equations for the parallel flow velocities as

$$\mathbf{u}_{e_{\|}} = \frac{1}{e n_o[(\frac{m_e}{m_i}) - 1]}\mathbf{J}_{\|} \,, \quad \text{and} \tag{199}$$

$$\mathbf{u}_{i_\parallel} = (\frac{m_e}{m_i})\mathbf{u}_{e_\parallel} \ . \tag{200}$$

The parallel electron and ion flows are shown in Fig. 24, as well as the ion pressure and electric field in the axial direction. Note, the pressure was divided evenly between the ion and electron species, and is set to be the same for both ions and electrons.

To solve for the perpendicular flow velocities we add and subtract the equilibrium momentum equations. In doing this, it is helpful to define four terms, $\mathbf{p}_+ = \frac{\nabla p_e}{en_e} + \frac{\nabla p_i}{en_i}$, $\mathbf{p}_- = \frac{\nabla p_e}{en_e} - \frac{\nabla p_i}{en_i}$, $\mathbf{u}_+ = \mathbf{u}_e + \mathbf{u}_i$, and $\mathbf{u}_- = \mathbf{u}_e - \mathbf{u}_i$ giving

$$\mathbf{p}_- + (2\mathbf{E} + \mathbf{u}_+ \times \mathbf{B}) = -2\frac{m_e \nu_{ei}}{e}\mathbf{u}_- \ , \tag{201}$$

$$\mathbf{p}_+ + (\mathbf{u}_- \times \mathbf{B}) = 0 \ . \tag{202}$$

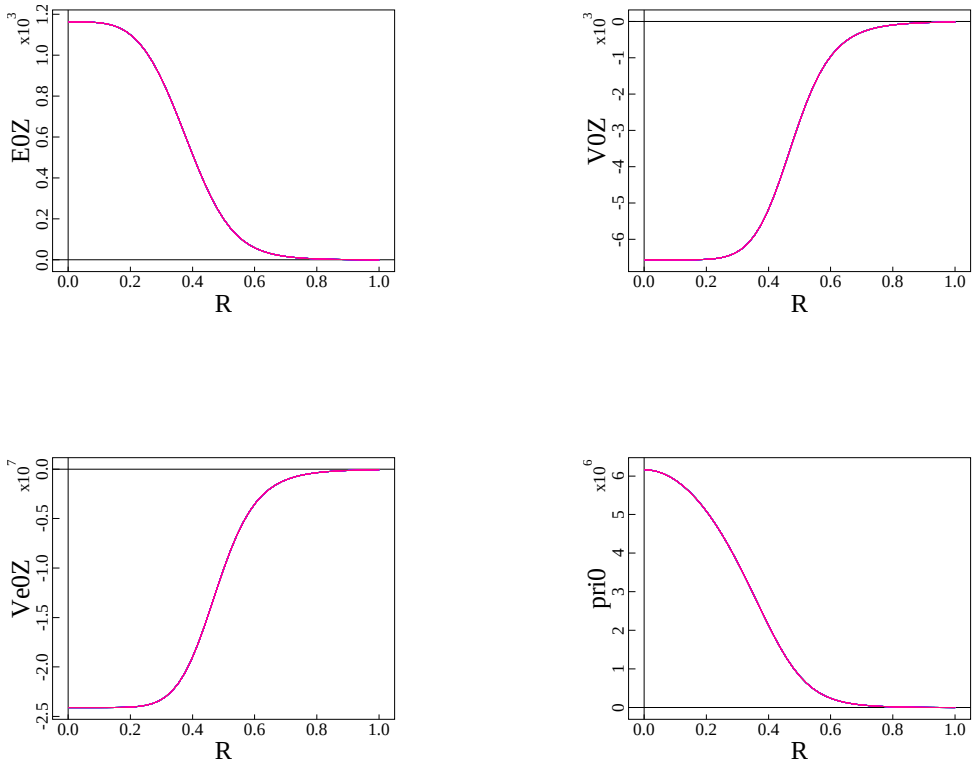

Fig. 24. Equilibrium electric field in the axial direction, the axial components of the ion and electron flows, and the ion pressure, which equals the electron pressure.

Now cross the magnetic field with both of these equations to solve for the components of flow perpendicular to the magnetic field.

$$\mathbf{B}\times\mathbf{p}_- + 2(\mathbf{B}\times\mathbf{E}) + B^2\mathbf{u}_{+_\perp} = -2\frac{m_e\nu_{ei}}{e}\mathbf{B}\times\mathbf{u}_- \ , \tag{203}$$

$$\mathbf{B}\times\mathbf{p}_+ + B^2\mathbf{u}_{-_\perp} = 0 \ . \tag{204}$$

From Eq. (204), a direct solution for $\mathbf{u}_{-_\perp}$ can be found by dividing through by the magnetic field magnitude, namely,

$$\mathbf{u}_{-_\perp} = \frac{1}{B^2}(\mathbf{B}\times\mathbf{p}_+) \ . \tag{205}$$

Rearranging Eq. (202) yields, $\mathbf{B}\times\mathbf{u}_- = \mathbf{p}_+$, which can be substituted into the right side of Eq. (203) giving

$$\mathbf{B}\times\mathbf{p}_- + 2(\mathbf{B}\times\mathbf{E}) + B^2\mathbf{u}_{+_\perp} = -2\frac{m_e\nu_{ei}}{e}\mathbf{p}_+ \ . \tag{206}$$

Solving for $\mathbf{u}_{+_\perp}$ yields

$$\mathbf{u}_{+_\perp} = -\frac{1}{B^2}\mathbf{B}\times\mathbf{p}_- - \frac{2}{B^2}(\mathbf{B}\times\mathbf{E}) - 2\frac{m_e\nu_{ei}}{eB^2}\mathbf{p}_+ \ . \tag{207}$$

Finally, based on our previous definitions, we have the following solution for the perpendicular parts of the ion and electron flow velocities,

$$\mathbf{u}_{e_\perp} = \frac{1}{2}(\mathbf{u}_{+_\perp} + \mathbf{u}_{-_\perp}) \ , \tag{208}$$

$$\mathbf{u}_{i_\perp} = \frac{1}{2}(\mathbf{u}_{+_\perp} - \mathbf{u}_{-_\perp}) \ . \tag{209}$$

These have been specified and loaded in as the initial conditions in the two fluid study. The perpendicular (azimuthal) flows, as well as the azimuthal component of the magnetic and the electric fields are shown in Fig. 25.

Lastly before the full conversion from the Holmes MHD to the current two fluid study, we mention we have added a viscosity term for numerical smoothing of velocity fluctuations. While this term may be derived as part of the small kinematic viscosity in such plasmas, here the coefficient is exaggerated and the term is used to eliminate the small, quick oscillations that arise in a two species study. This allows the slower oscillations inherent in the MHD approximation to arise in the plasma

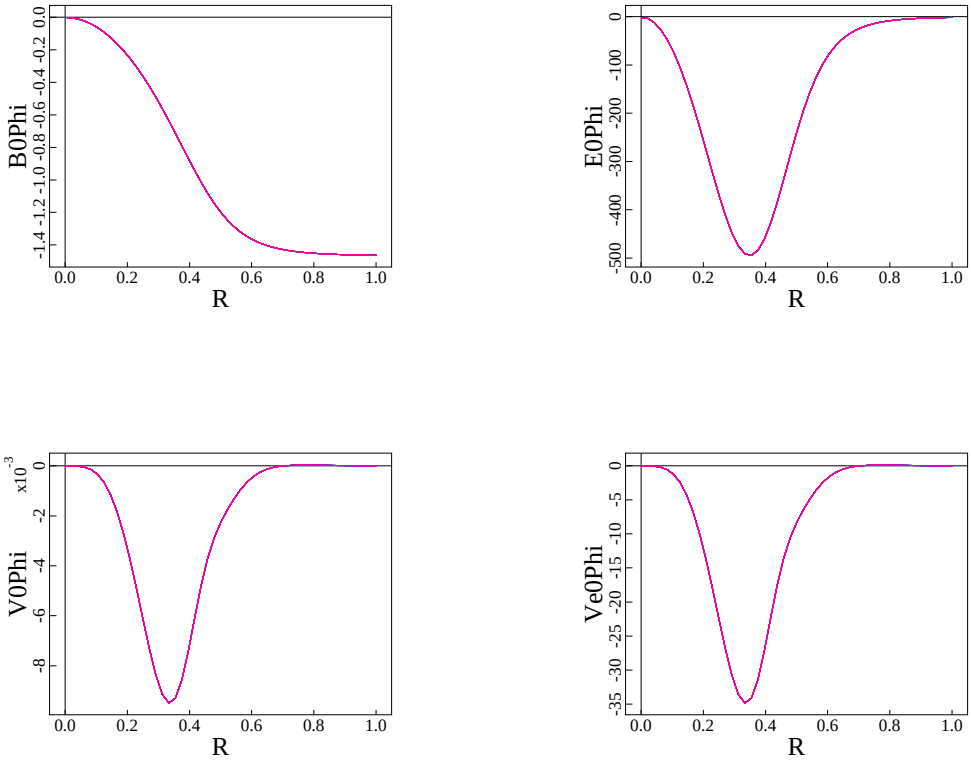

Fig. 25. The azimuthal magnetic field is the same as the MHD case; also, note the azimuthal electric field is shown here. Also the current density has been split into ion and electron flows, shown here for the azimuthal directions. Note the azimuthal symmetry is still the same as the MHD case.

even when faster oscillations are present. The form we use is

$$C_{visc}\nabla^2\mathbf{u}_s \tag{210}$$

for both ions and electrons. In the finite element approach with C^0 basis functions, an integration by parts is needed after multiplication by the test functions:

$$\int_\Omega d\mathbf{V}\ \boldsymbol{\alpha}\cdot C_{visc}\nabla^2\mathbf{u}_s = -\int_\Omega d\mathbf{x}\ C_{visc}\nabla\boldsymbol{\alpha}\cdot\nabla\mathbf{u}_s \quad + \int_s d\mathbf{S}\ C_{visc}\boldsymbol{\alpha}\cdot\nabla\mathbf{u}_s\ , \tag{211}$$

where the last surface integral goes to zero given our boundary conditions. The term that survives

is a vector dotted into a rank two tensor as follows

$$\left[\hat{x}\frac{\partial}{\partial x}\alpha+\hat{y}\frac{\partial}{\partial y}\alpha+\hat{z}\frac{\partial}{\partial z}\alpha\right]\cdot\begin{bmatrix}\hat{x}\frac{\partial}{\partial x}u_x\hat{x} & \hat{y}\frac{\partial}{\partial y}u_x\hat{x} & \hat{z}\frac{\partial}{\partial z}u_x\hat{x}\\ \hat{x}\frac{\partial}{\partial x}u_y\hat{y} & \hat{y}\frac{\partial}{\partial y}u_y\hat{y} & \hat{z}\frac{\partial}{\partial z}u_y\hat{y}\\ \hat{x}\frac{\partial}{\partial x}u_z\hat{z} & \hat{y}\frac{\partial}{\partial y}u_z\hat{z} & \hat{z}\frac{\partial}{\partial z}u_z\hat{z}\end{bmatrix}. \tag{212}$$

To dedimensionalize this term, remember that $n_s m_s$ has been divided through and note C_{visc} has units of m^2/s such that

$$\frac{r_o}{c^2}\frac{c}{r_o^2}C_{visc}\nabla^2\mathbf{u}_s=\frac{1}{cr_o}C_{visc}\nabla^2\mathbf{u}_s\ . \tag{213}$$

The ratio of the coefficient for this viscosity and the conductivity term define the Prandtl number: $P=\frac{C_{elecd}}{C_{visc}}$. We mention this term is specified in the Holmes paper and is a good term to provide guidance for numerical dissipation in our resistive tearing mode simulation.

We have also added a diffusion term to the continuity equation, namely,

$$D_{visc}\nabla^2 n_s\ , \tag{214}$$

to smooth out small scale fluctuations in density. Again, while the term does not belong in the fundamental equations, we use it to provide numerical stability. It is important to test that the physical results are not tied to the values for D_{visc} and C_{visc}.

To make this term dimensionless, we proceed in a similar fashion to the viscosity term, noting the division by cn_0/r_0, which yields

$$\frac{r_o}{cn_o}\frac{n_o}{r_o^2}D_{visc}\nabla^2 n_s=\frac{1}{cr_o}D_{visc}\nabla^2 n_s\ . \tag{215}$$

Having converted the initial conditions for the Holmes MHD case, which were derived by force balance, into the corresponding two fluid initializations, it is good to readdress the idea of force balance. This is done by not initializing perturbations and advancing the equations given our cylindrical, two fluid equilibrium. This would require the use of a rather small grid size to properly resolve each of the forces and accurately demonstrate force balance. Currently, this has only been explored on a small personal laptop that was unable to run the algorithm for a long enough time to adequately address this issue of having force balance. What was observed is the forces were balanced very well in the azimuthal and axial directions, but the radial direction appeared to have some evolution, indicating complete force balance was not obtained. This leads us to inquire about

the ion and electron flows perpendicular to the background magnetic field.

To test this concept of force balance, the original algorithm needed to be modified so as to run in a nonlinear fashion (for more information, see Appendix A). As such a separate subroutine was made to address nonlinearities and produce a matrix preconditioning step for our Newton Krylov method. The NIMROD code has a routine to perform this in an iterative manner for the MHD equations it uses. This same principle was followed in the two species algorithm. A preconditioning matrix is produced in such a way the solution vector can be converged upon more efficiently. The concept of this GMRES operation follows the same principles as outlined in Iterative Methods for Sparse Linear Systems [29].

As we look further at studying the stability of the two fluid Holmes case, we note some special considerations. Because the electrons and ions are allowed to advance separately, the electrons tend to require a smaller time step to adequately refine their motion. In this manner, the rapid oscillations of the electrons are resolved. This motion does not limit the overall characteristics of the plasma, but simply requires a long run for the two fluid code. In the Homes MHD case, a time step of $\Delta t = 1 \times 10^{-7} s$ was adequate, while in the two fluid case, a time step of $\Delta t = 1 \times 10^{-19} s$ was needed. In the MHD case, the code needed to run on the order of 10^3 time steps to reach 100 μs, and a converged growth rate. If the same final time was needed for the two fluid case, we would need to evolve on the order of 10^{15} time steps. This was an inconceivably large amount of computational time.

As a first attempt to compare these results, we ran the Homes MHD case at a similarly small time step and compared its results to the two fluid model. It is not clear the recombination of the ion and electron flows is able to recover the current density predicted by MHD. More time and thought are needed to further verify this case. However, while running the two species model for an extended time, on the order of days, it appeared the growth rate was converging to a fixed value. This is a good beginning for future study and investigation.

5.2. Minimum energy equilibrium

Having considered an initial study of the stability of the Holmes equilibrium, we move on to the study of stability for the minimum energy state described by Edwards and Held [19]. This study focused on the minimization of a confined two species collisionless plasma. The steady-state fluid equations that describe this stationary plasma are the equations of state, momentum equations, Poisson's and Ampère's Laws, and continuity equations as follows

$$p_s = C_s n_s^{\gamma} \ , \tag{216}$$

$$n_s m_s \mathbf{u}_s \cdot \nabla \mathbf{u}_s = q_s n_s (\mathbf{E} + \mathbf{u}_s \times \mathbf{B}) - \nabla p_s \ , \tag{217}$$

$$\nabla \cdot \mathbf{E} = \sum_s \frac{q_s n_s}{\epsilon_0} \ , \tag{218}$$

$$\nabla \times \mathbf{B} = \mu_0 \sum_s q_s n_s \mathbf{u}_s \ , \tag{219}$$

$$\nabla \cdot n_s \mathbf{u}_s = 0 \ . \tag{220}$$

In addition, the plasma was assumed to be symmetric in two directions (azimuthal and axial), but varying in the third (radial). Because of this, the above equations are under determined, thus opening an avenue for minimizing energy. To do this the total energy of the system is considered

$$U = \int d\mathbf{V} [\frac{\epsilon_o}{2} E^2 + \frac{1}{2\mu_0} B^2 + \sum_s (\frac{n_s m_s}{2} u_s^2 + \frac{1}{\gamma - 1} p_s)] \ , \tag{221}$$

and then is varied with the additional constraints of $\nabla \cdot \mathbf{B} = 0$ and $\nabla \times \mathbf{E} = 0$ with the equation of state $p_s = C_s n_s^{\gamma}$ used to eliminate p_s. This yields a set of partial differential equations that become ordinary differential equations, assuming symmetry in two directions, with the resultant ordinary differential equations solved numerically. Fig. 26 shows the profiles of the number densities and the electric field for one of the cylindrically symmetric, minimum energy equilibria discussed in Ref. [19]. Note, this equilibrium is balanced for both species. For the electrons, the electric and magnetic fields balance out the pressure through the Lorentz force. The effect of the magnetic field is negligible for the ions and it is the electric field only that balances out the pressure.

Here, we are interested in the stability of these minimum energy, equilibrium solutions. Equilibrium data files from Dr. Edwards' code were read into NIMROD and an interpolation scheme was used to take data from one grid to the others. Fourth-order interpolation was used. Figs. 27 and 28 show the profiles provided by Dr. Edwards for a case similar to that shown in Fig. 26.

As was considered in the Holmes case, an initial exploration of force balance was conducted. Because the values of number density are so large, small interpolation errors in the ion and electron species can lead to large electric fields. Consider, for example, the computation of the radial component of the electric field in cylindrical geometry given by Poisson's equation,

$$\nabla \cdot \mathbf{E} = \sum_s \frac{q_s n_s}{\epsilon_0} \ . \tag{222}$$

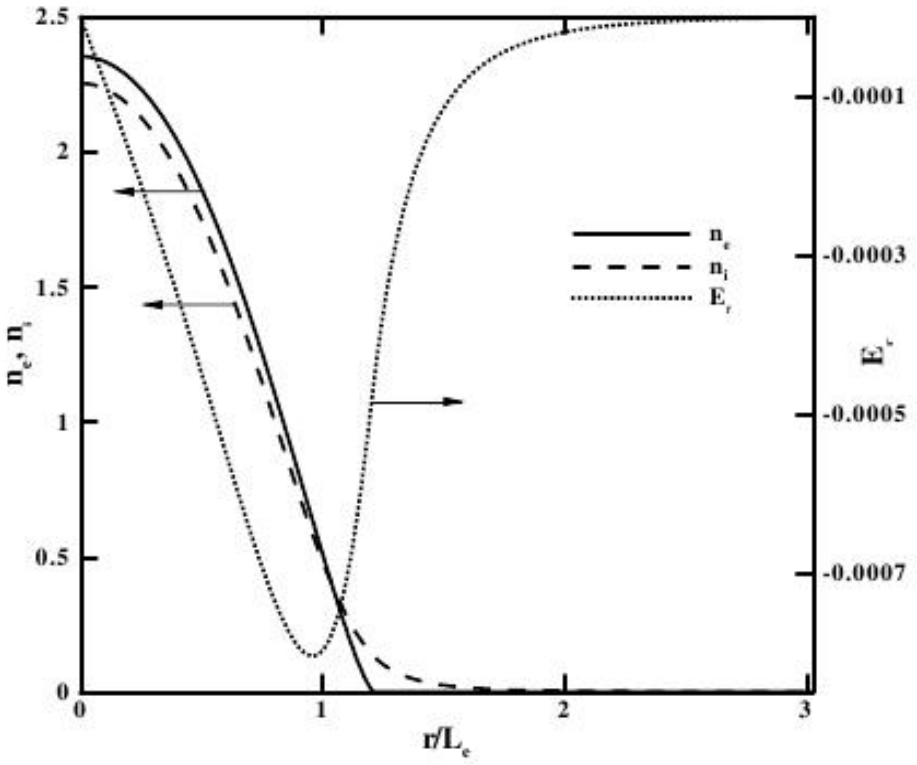

Fig. 26. The ion and electron number densities and electric field profiles. The radial direction is scaled by the electron skin depth, $L_e = c/\omega_{pe}$.

Using the values from the data files for number density and approximating the divergence of the electric field in the radial direction using second order FD

$$\frac{E_r^{k+1} - E_r^{k-1}}{2\Delta r} - \frac{E_r^k}{r^k} - \frac{(q_i n_i + q_e n_e)}{\epsilon_0} = \mathcal{E}_1 \ , \tag{223}$$

the resultant error, $\mathcal{E}_1$, can be calculated. When this was done, significant error was found in the data that was initially read in. A subroutine was written that calculated this difference between the divergence of the electric field and the sum of the charge densities. NIMROD results showed the initial error from the provided data was relatively large, but as the two fluid equations advanced, this error shrunk, but did not vanish completely. Initial differences may be due to the size of the grid and the large number density terms. As seen in the Holmes' case, errors in the equilibrium profiles lead to additional waves and instabilities in the plasma. Further care in preparing the equations is necessary before these important stability calculations may be carried out.

In an initial attempt to resolve some of the force balance issues, grid packing was used. The forces at the region near the center of the plasma column balanced out very well. The greatest

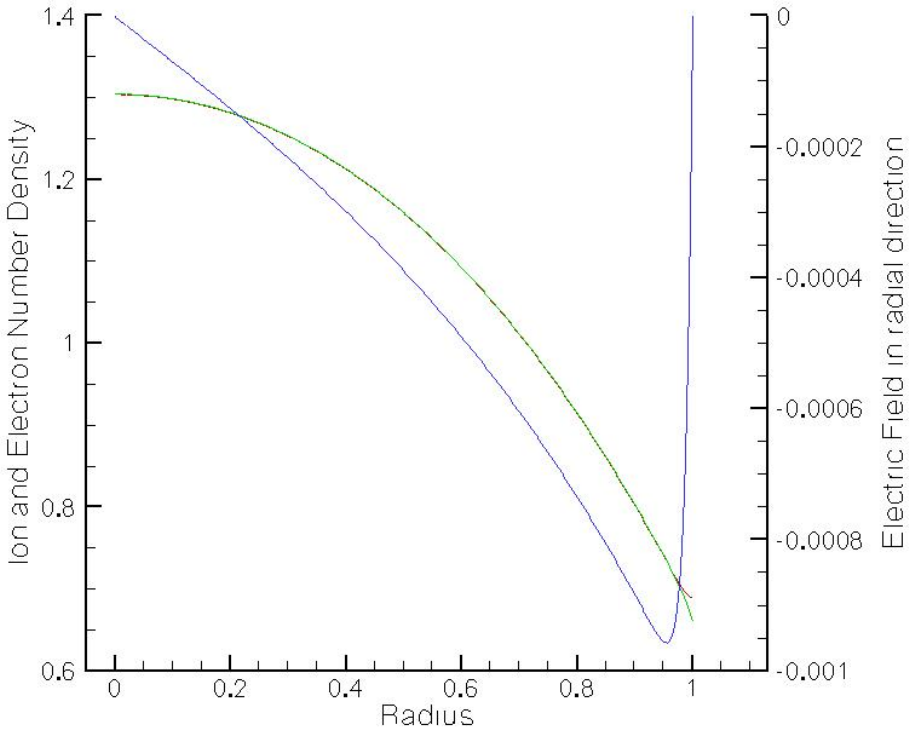

Fig. 27. The ion and electron number densities and electric field profiles, as provided by Dr. Edwards. The ion and electron number densities are shown with the axis to the left, and the electric field is on the right.

separation of ions and electrons occur towards the edge of the plasma column. This creates a large change in the computed electric field at the plasma column boundaries. As such, grid packing was used to put more grid points where the largest changes take place. To some degree, this helped to decrease the errors in the force balance, but it did not appear to make them all disappear. It would be beneficial to look at a separate set of data that could be tested and considered before three-dimensional stability calculations are conducted.

Figs. 29 and 30 show the growth starts at the plasma boundary and moves into the center of the plasma. Fig. 29 shows the perturbations in the radial electron velocity, which propagate from the outer column toward the center. This causes similar perturbations in other fields such as number density and magnetic field. Fig. 30 shows the evolution of the axial electric field. Note, it starts out at zero and the perturbation grows until it oscillates between two values as if an alternating source on axis were moving particles back and forth. This initial observation leads us to believe the forces at the very edge of the plasma are not balanced, and this imbalance is causing waves to move through the plasma.

In a similar manner the initial data given for the force balance leads to a nonnegligible elec-

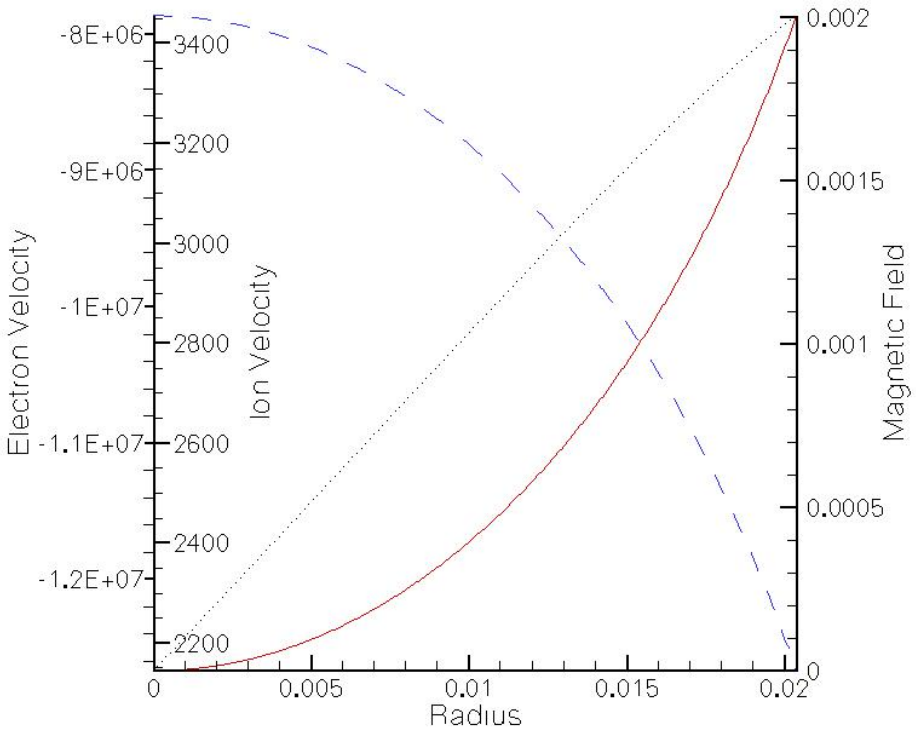

Fig. 28. The ion and electron equilibrium velocity profiles, as well as the equilibrium magnetic field in the azimuthal direction, as provided by Dr. Edwards. The electron (dashed) and ion (solid) velocities are shown with the axes to the left, and the magnetic field (dotted) on the right. It is noted the velocities are similar to each other given a factor of the mass ratio. As well, the velocities and magnetic field strengths balance out the force from the electric field and pressure terms.

tric fields and ion and electron flows in the axial direction. If we consider the axial (z subscript) component of the momentum equation, we have

$$u_{s_z}\frac{\partial}{\partial z}u_{s_z} = \frac{q_s}{m_s}\left(E_z + u_{s_\phi}B_r - u_{s_r}B_\phi\right) - \frac{\partial}{\partial z}p_s \ . \tag{224}$$

From the initialization, u_r and u_ϕ are both zero, and there is no initial variation in the axial direction, $\frac{\partial}{\partial z} = 0$, for any quantity in both species. This should, therefore, give $E_z = 0$, which is what we see in the initial quantities. But at the next time step, Fig. 30 shows that E_z is evolving.

The two most likely sources for this imbalance in Eq. (224) are either change in the radial flow or axial electric field. We suggest these two sources because the symmetry in the axial direction causes the gradient of pressure term and the convective derivative term to be zero. In addition there is no radial magnetic field nor azimuthal flows. Let us look first at the electric field advance which we take from the displacement current in Ampère's Law. The steady state given by Ampère's Law

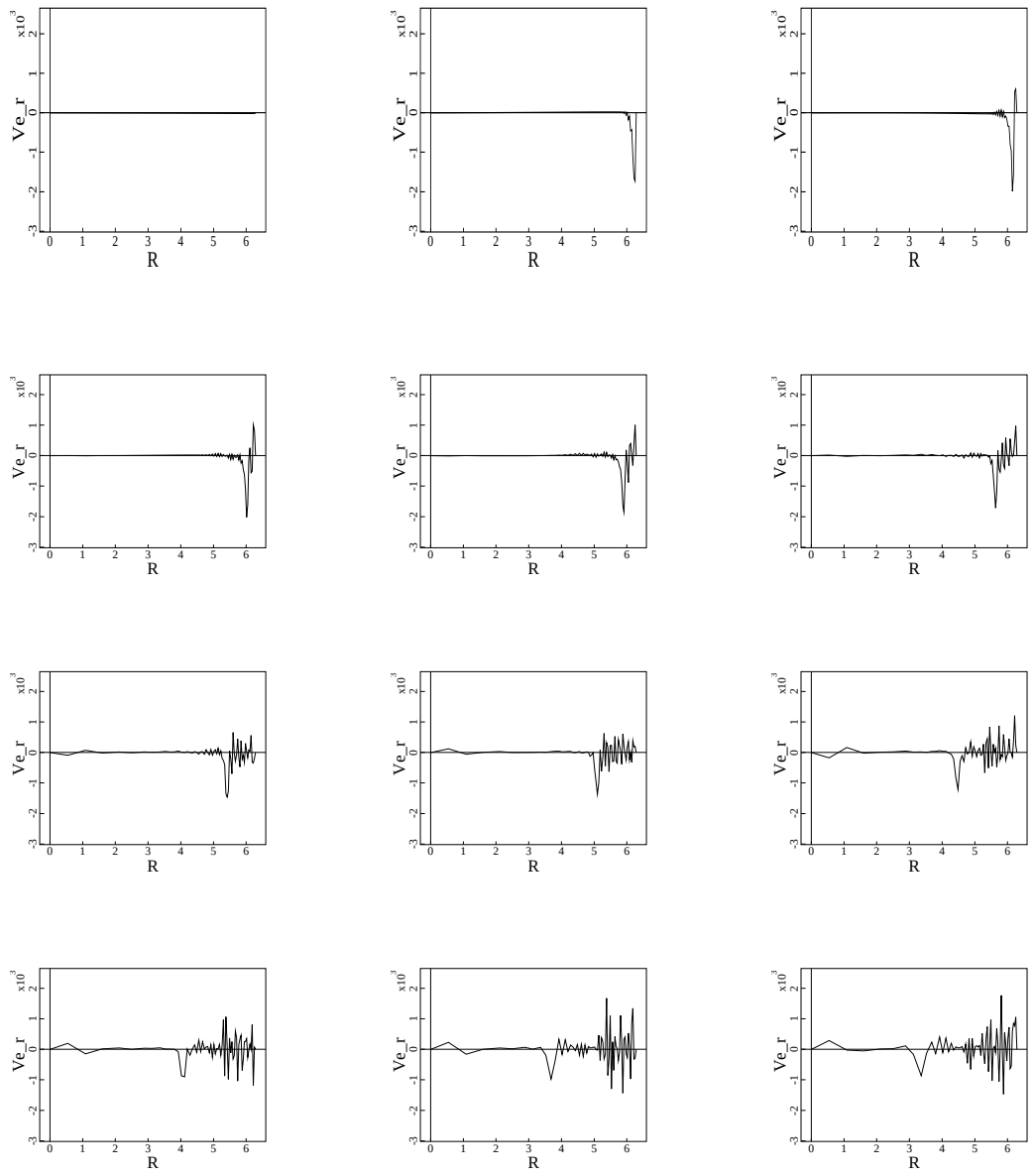

Fig. 29. The progression of perturbations in the radial electron flow that originate at the outside edge of the plasma column, most likely from lack of balance of forces at the outer edge. The perturbation moves to the inside and causes oscillations in its wake as the wave progresses.

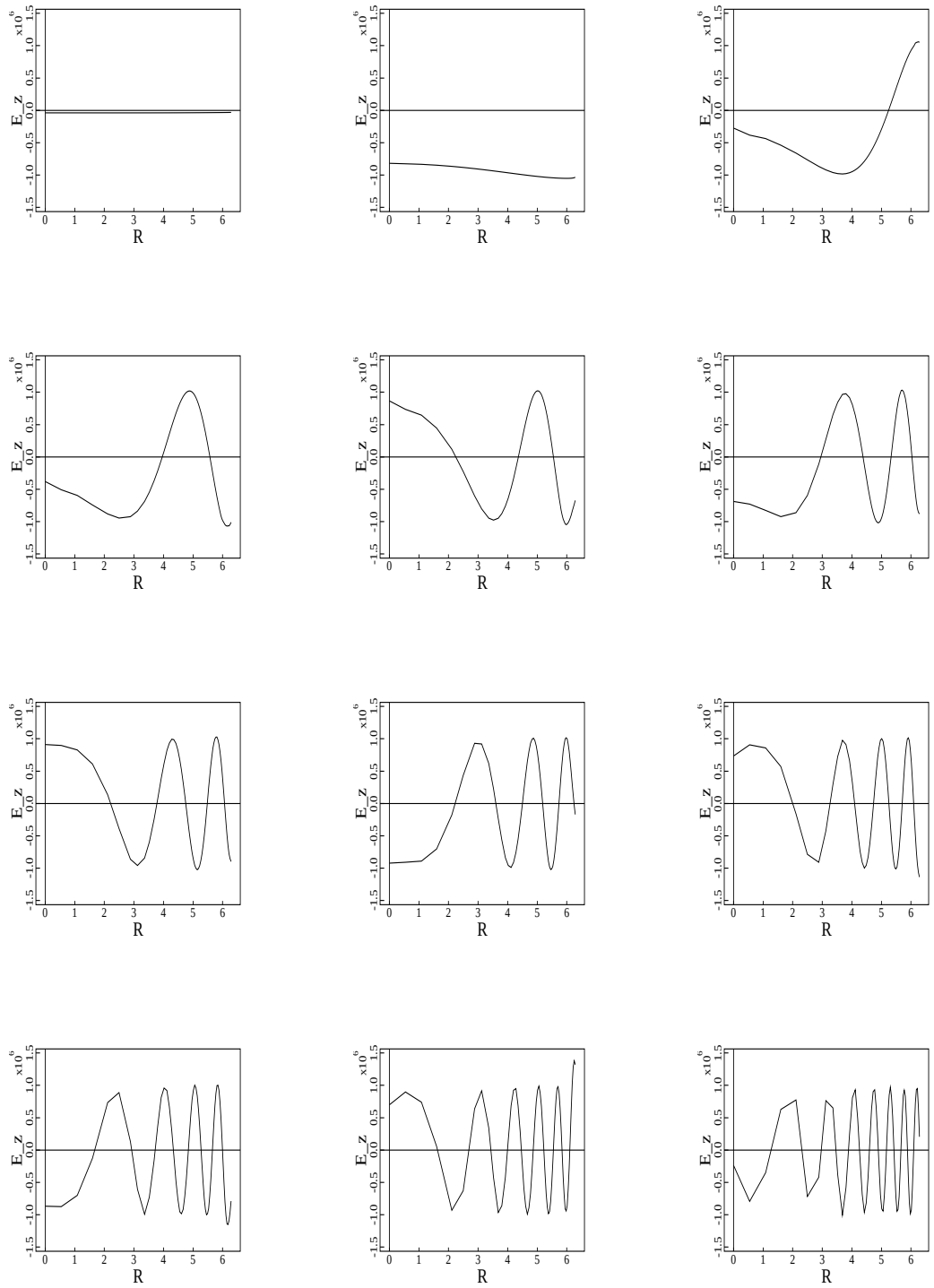

Fig. 30. The evolution of the electric field in the axial direction. It is initialized as zero; but, due to edge effects of the plasma column and not having perfect force balance, an oscillation starts and produces a wave that behaves in a whip fashion.

is

$$\nabla \times \mathbf{B} = \mu_0 \sum_s q_s n_s \mathbf{u}_s \ . \tag{225}$$

Considering only the axial directions with our initial conditions gives

$$\frac{1}{r}\frac{\partial}{\partial r}(rB_\phi) = \mu_0 e(n_i u_{i_z} - n_e u_{e_z}) \ . \tag{226}$$

As was done before, we can calculate an error associated with this equation as

$$\frac{1}{r^k}\frac{r^{k+1}B_\phi^{k+1} - r^{k-1}B_\phi^{k-1}}{2\Delta r} + \frac{B_\phi^k}{r^k} - \mu_0 e\left(n_i u_{i_z} - n_e u_{e_z}\right) = \mathcal{E}_2 \ . \tag{227}$$

Errors in this equation will give rise to an electric field in the axial direction (E_z) after taking a small time step. When we calculate $\mathcal{E}_2$ from the initial data arrays, we find it is much smaller and nearly constant in value, unlike the errors inherent in Poisson's equation. Thus, we claim the forces were adequately balanced in this axial direction.

It is conceivable this small difference will begin to cause some small growth in E_z, which could add into Eq. (224) and drive axial flow. But let us now look first at the velocity advance in the radial direction,

$$\frac{\partial}{\partial t}u_r + u_r\frac{\partial}{\partial r}u_r + u_z\frac{\partial}{\partial z}u_r + \frac{u_\phi}{r}\frac{\partial}{\partial \phi}u_r - \frac{u_\phi^2}{r} = \frac{q_s}{m_s}\left(E_r + u_z B_\phi - u_\phi B_z\right) - \frac{\partial}{\partial r}p_s \ . \tag{228}$$

Here, all the convective derivative terms will disappear, as well as the additional cylindrical coordinate term (u_ϕ^2/r) and part of the cross product term ($u_\phi B_z$). But, the E_r, $u_z B_\phi$ and the $\frac{\partial}{\partial r}p_s$ terms could give a contribution to the flow velocity in the radial direction, if the remaining terms do not balance in this manner:

$$E_r = -u_z B_\phi + \frac{m_s}{q_s n_s}\frac{\partial}{\partial r}p_s \ . \tag{229}$$

If this imbalance is the cause, then the resulting differences will be added into the advance of the radial velocities and in Eq. (224) the $u_r B_\phi$term will become finite, giving rise to a nonnegligible axial flow.

Again we compute the force balance from Eq. (229) by considering both species pressures and solving for the force balance difference as $\mathcal{E}_3$:

$$E_r^k - \frac{B_\phi^k}{2}\left(u_{i_z}^k - u_{e_z}^k\right) - \left(\frac{m_i - m_e}{2e}\right)\left(\frac{p_i^{k+1} - p_i^{k-1}}{2\Delta r\ n_i^k} + \frac{p_e^{k+1} - p_e^{k-1}}{2\Delta r\ n_e^k}\right) = \mathcal{E}_3 \ . \tag{230}$$

This $\mathcal{E}_3$ then is directly proportional to the time advanced radial flow velocities as shown in Eq. (228). Fig. (31) shows this is exactly what we see as the initial conditions are allowed to advance in time. Here we have taken the $\mathcal{E}_3$ values at each data point given as a function of radius, and compared that to the radial component of the velocity advance we obtained by testing our force balance. Note, although the values are different, the behavior is the same suggesting this nonnegligible axial electric field production is tied to this apparent inaccuracy in the force balance of Eq. (224).

This initial study of the minimum energy states for two fluid plasmas suggests before moving on to three-dimensional stability calculations, it is necessary to address the initial imbalance. Only

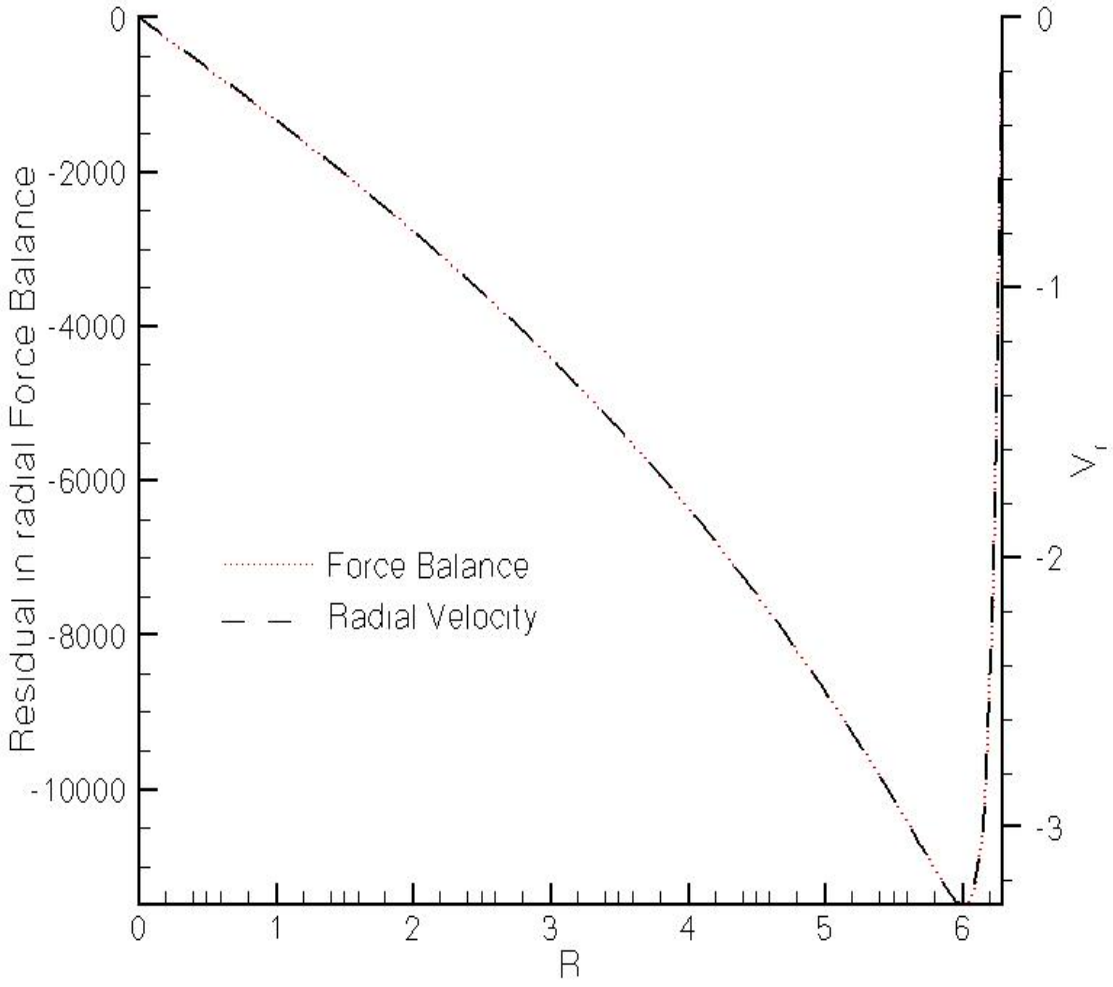

Fig. 31. The results of Eq. (230) in a graphical form as the dotted line. It also shows the radial velocity after the first time step as the dashed line. Although the scale is not the same the shape of the curves is. The correspondence suggests errors in radial force balance from the initial data set drives the evolution shown in Figs. 29 and 30.

then does it make sense to perturb the equilibrium and do full stability calculations. As we have looked at the many different waves that persist in a two species plasma, it is necessary to discuss and understand their sources. Our preliminary stability studies must satisfy force balance. If the forces are not balanced, plasma waves are immediately generated and the initial state moves away from the equilibrium we are testing.

As this work progresses, a next step would be to consider a different minimum energy equation, a different z pinch or a screw pinch, or possibly the one shown in Fig. 26 where the number densities of the ions smoothly go to zero at the edge of the plasma column. It is conceivable this would improve the force balance at the very edge of the plasma making 3-D stability tests of these systems possible.

In conclusion, we have made a study of two species plasmas, evolving the number density, flow velocity, and temperature equations coupled to Maxwell's electric and magnetic field equations, making special note of the inclusion of the displacement current. Analyzing and considering these coupled equations led to the discussion of normal modes in cold and hot plasmas, as represented by dispersion relations resulting from a linear analysis of the two fluid equations. In doing so, we addressed the numerical theory in relation to the ideas of geometry, temporal and spatial discretization, linearization of the fluid equations, and the NIMROD expansion using the finite element approach. This naturally led to the demonstration of numerical results generated by this algorithm in comparison to analytical results and other published material. Specifically, we discussed the numerical results of electrostatics, acoustic waves, temperature effects on acoustic waves, θ-centered time advances, electromagnetic waves, whistler waves, MHD waves, and a Fourier analysis of many different plasma waves. A final consideration was given to stability calculations, focusing on the force balance of the initial conditions in a resistive MHD mode and a static minimum energy plasma state. Initial observations were stated, as well as guidance for future work to be considered.

REFERENCES

[1] J.D. Huba, Revised NRL Plasma Formulary, Naval Research Laboratory, Washington, 2011.

[2] J.P. Freidburg, Ideal Magnetohydrodynamics, Plenum Press, New York, 1987.

[3] H.R. Strauss, Nonlinear, three-dimensional magnetohydrodynamics of noncircular tokamaks, The Physics of Fluids 19 (1) (1976) 134-140.

[4] H.R. Strauss, Dynamics of high beta tokamaks, The Physics of Fluids 20 (8) (1977) 1354-1360.

[5] J.A. Breslau, S.C. Jardin, A parallel algorithm for global magnetic reconnection studies, Computer Physics Communications 151 (1) (2003) 8-24.

[6] R.J. Mason, Hybrid two-dimensional electron transport in self-consisent electromagnetic fields, IEEE Transactions on Plasma Science 14 (1) (1986) 45-52.

[7] R.J. Mason, An electromagnetic field algorithm for 2d implicit plasma simulation, Journal of Computational Phyiscs 71 (2) (1987) 429-473.

[8] C. Hirsch, C. Hirsch, Numerical Computation of Internal and External Flows: Fundamentals of Numerical Discretization, Wiley series in numerical methods in engineering. Wiley, New York, 1991.

[9] E.F. Toro, Riemann Solvers and Numerical Methods for Fluid Dynamics: A Practical Introduction. Springer, Berlin, 1997.

[10] U. Shumlak, A. Hakim, J. Loverick, A high resolution wave propagation scheme for ideal two-fluid plasma equations. Journal of Computational Physics 219 (2006) 418-442.

[11] G.E. Karniadakis, G.K.S.J. Sherwin, Spectral/hp Element Methods for cfd, Numerical Mathematics and Scientific Computation Series, Oxford, 1999.

[12] W.G. Strang, G.J. Fix, An Analysis of the Finite Element Method, Prentice-Hall series in automatic computation, Prentice-Hall, Englewood Cliffs, 1973.

[13] T.H. Stix, Theory of Plasma Waves, Springer, New York, 1992.

[14] D.G. Swanson, Plasma Waves, Academic Press, Boston, 1989.

[15] D.G. Swanson, Plasma Waves, 2nd Edition, Series in Plasma Physics Series, Taylor & Francis Group, Bristol, 2003.

[16] J.A. Holmes, B.A. Carreras, T.C. Hender, H.R. Hicks, V.E. Lynch, B.F. Masden, A comparison of the full and reduced sets of magnetohydrodynamic equations for resistive tearing modes in cylindrical geometry, Physics of Fluids 26 (1983) 2569-2577.

[17] C.R. Sovinec, A.H. Glasser, T.A. Gianakon, D.C. Barnes, R.A. Nebel, S.E. Kruger, S.J. Plimpton, A. Tarditi, M.S. Chu, and the NIMROD Team, Nonlinear magnetohydrodynamics with high-order finite elements, Journal of Computational Physics 195 (2004) 355.

[18] D.D. Schnack, D.C. Barnes, D.P. Brennan, C.C. Hegna, E. Held, C.C. Kim, S.E. Kruger, A.Y. Pankin, C.R. Sovinec, Computational modeling of fully ionized magnetized plasmas using the fluid approximation, Physics of Plasmas 13 (5) (2006) 058103.

[19] W.F. Edwards, E.D. Held, Stationary equilibria of two fluid plasmas having significant, internal, static electric fields, Physics Review Letters 93 (25) (2004) 058103.

[20] S. Chapman, T.G. Cowling, The Mathematical Theory of Non-Uniform Gases, Cambridge University Press, London, 1970.

[21] D. Enskog, Kinetische theories, Svenska Akadamien, 63 (1921).

[22] D. Burnett, The distribution of velocities in a slightly non-uniform gas, Proceedings of the London Mathematical Society 2 (1935) 385.

[23] H. Grad, On the kinetic theory of rarefied gasses, Communications on Pure and Applied mathematics 2 (1949) 331-407.

[24] H. Grad, Asymptotic theory of the boltzmann equation, Physics of Fluides 6 (1963) 147-181.

[25] Jie Wu Bo-Nan Jiang, L.A. Povinelli, The origin of spurious solutions in computational electromagnetics, Journal of Computational Physics 125 (1996) 104-123.

[26] R. Schneider, E. Sonnendruker, U. VoB, C.-D. Munz, P. Omnes, Divergence correction techniques for Maxwell solvers based on hyperbolic model, Journal of Computational Phyiscs 161 (2000) 484-511.

[27] D.A. Gurnett, A. Bhattacharjee, Introduction to Plasma Phyiscs, Cambridge University Press, Cambridge, 2005.

[28] C.R. Sovinec, D.C. Barnes, R.A. Bayliss, D.P. Brennan, E.D. Held, S.E. Kruger, A.Y. Pankin, D.D. Schnackand, and the NIMROD Team, Two-fluid studies of edge relaxztion events in tokamaks, Journal of Physics: Conference Series 78 (1) (2007) 012070.

[29] Y. Saad, Iterative Methods for Sparse Linear Systems, Society for Industrial and Applied Mathematics, Philadelphia, 2003.

APPENDIX

Before rewriting all of the equations, a simplification of notation is used below by writing $\Delta A = A^{k+1} - A^k$. The time-discretized equations are

$$\Delta\mathbf{E} - \theta\Delta t\left[c^2\left(\nabla\times\Delta\mathbf{B}\right) - \sum_s \frac{e_s\Delta n_s\Delta\mathbf{u}_s}{\epsilon_0}\right] = \Delta t\left[c^2\left(\nabla\times\mathbf{B}^k\right) - \sum_s \frac{e_s n_s^k\mathbf{u}_s^k}{\epsilon_0}\right] , \tag{231}$$

$$\Delta\mathbf{B} + \theta\Delta t\nabla\times\Delta\mathbf{E} = -\Delta t\nabla\times\mathbf{E}^k , \tag{232}$$

$$\Delta\mathbf{u}_s + \theta\Delta t\left[\left(\Delta\mathbf{u}_s\cdot\nabla\right)\Delta\mathbf{u}_s + \frac{\nabla(\Delta p_s)}{\Delta n_s m_s} - \frac{e_s}{m_s}(\Delta\mathbf{E} + \Delta\mathbf{u}_s\times\Delta\mathbf{B})\right] = \\ -\Delta t\left[\left(\mathbf{u}_s^k\cdot\nabla\right)\mathbf{u}_s^k - \frac{\nabla p_s^k}{n_s^k m_s} + \frac{e_s}{m_s}\left(\mathbf{E}^k + \mathbf{u}_s^k\times\mathbf{B}^{tk}\right)\right] , \tag{233}$$

$$\Delta n_s + \theta\Delta t\nabla\cdot\left(\Delta n_s\Delta\mathbf{u}_s\right) = -\Delta t\nabla\cdot n_s^k\mathbf{u}_s^k , \tag{234}$$

$$\Delta T_s + \theta\Delta t\left[\left(\Delta\mathbf{u}_s\cdot\nabla\right)\Delta T_s + \frac{2}{3}\Delta T_s\left(\nabla\cdot\Delta\mathbf{u}_s\right)\right] = -\Delta t\left[\left(\mathbf{u}_s^k\cdot\nabla\right)T_s^k - \frac{2}{3}T_s^k\left(\nabla\cdot\mathbf{u}_s^k\right)\right] . \tag{235}$$

There is a bit of difficulty in treating nonlinear terms that have two perturbed variables multiplying each other, $\nabla\cdot(\Delta n_s\Delta\mathbf{u}_s)$ for instance. To demonstrate the specifics of these terms, we consider the divergence term in the continuity equation. We start by separating it into implicit and explicit parts

$$\theta\left[\nabla\cdot\left(n_s^{k+1}\mathbf{u}_s^{k+1}\right)\right] = -(1-\theta)\nabla\cdot\left(n_s^k\mathbf{u}_s^k\right) . \tag{236}$$

Next, substituting in $A^{k+1} = \Delta A + A^k$ for both the number density and flow velocity gives

$$\theta\left[\nabla\cdot\left(\Delta n_s\Delta\mathbf{u}_s\right) + \nabla\cdot\left(\Delta n_s\mathbf{u}_s^k\right) + \nabla\cdot\left(n_s^k\Delta\mathbf{u}\right) + \nabla\cdot\left(n_s^k\mathbf{u}_s^k\right)\right] = -(1-\theta)\nabla\cdot\left(n_s^k\mathbf{u}_s^k\right) . \tag{237}$$

This leaves four terms on the left side. The last three are linear, having either the previous solution to a field variable multiplied by a perturbed quantity, or the sum of two previous solutions. However, the first term is higher order, specifically the product of two perturbed quantities, Δn_s and $\Delta\mathbf{u}_s$. Taking only Newton-like steps (where vectors are evaluated using Taylor series expansions) keeping only linear terms (where higher-order terms are ignored)[28], and canceling like terms gives

$$\theta\left[\nabla\cdot\left(\Delta n_s\mathbf{u}_s^k\right) + \nabla\cdot\left(n_s^k\Delta\mathbf{u}\right)\right] = -\nabla\cdot\left(n_s^k\mathbf{u}_s^k\right) . \tag{238}$$

Before implementing this Newton-like step for the dual perturbed variables, we consider a term with three variables, $\frac{\nabla n_s T_s}{n_s}$. First, we use the product rule to simplify this down to a gradient of single terms, $\frac{\nabla n_s T_s}{n_s} = \nabla T_s + \frac{T_s \nabla n_s}{n_s}$. Now looking only at the second part and writing this in implicit and explicit parts gives

$$\theta \left(\frac{T_s^{k+1} \nabla n_s^{k+1}}{n_s^{k+1}} \right) = -(1-\theta) \frac{T_s^k \nabla n_s^k}{n_s^k} \ . \tag{239}$$

Using $A^{k+1} = \Delta A + A^k$ as before gives

$$\theta \left[\frac{\left(\Delta T_s + T_s^k\right) \nabla \left(\Delta n_s + n_s^k\right)}{\left(\Delta n_s + n_s^k\right)} \right] = -(1-\theta) \frac{T_s^k \nabla n_s^k}{n_s^k} \ . \tag{240}$$

Using a Taylor expansion for the denominator and factoring the numerator leads to

$$\theta \frac{1}{n_s^k} \left(1 - \frac{\Delta n_s}{n_s^k} \right) \left(\Delta T_s \nabla \Delta n_s + T_s^k \nabla \Delta n_s + \Delta T_s \nabla n_s^k + T_s^k \nabla n_s^k \right) = -(1-\theta) \frac{T_s^k \nabla n_s^k}{n_s^{tk}} \ . \tag{241}$$

Taking only Newton-like steps, thus getting rid of quadratic or triplet perturbed terms and canceling like terms on both sides gives

$$\theta \left[\frac{T_s^k \nabla \Delta n_s}{n_s^k} + \frac{\Delta T_s \nabla n_s^k}{n_s^k} - \frac{\left(T_s^k \nabla n_s^k\right) \Delta n_s}{\left(n_s^k\right)^2} \right] = -\frac{T_s^k \nabla n_s^k}{n_s^k} \ . \tag{242}$$

With these two substitutions and similar ones for the terms $q_s n_s \mathbf{u}_s$, $\mathbf{u}_s \cdot \nabla \mathbf{u}_s$, $\mathbf{u}_s \times \mathbf{B}$, $T_s \nabla \cdot \mathbf{u}_s$, and $\mathbf{u}_s \cdot \nabla T_s$ a Newton-like advance of the full nonlinear equations in time that can handle fully implicit, fully explicit, or anything in between is shown below:

$$\Delta \mathbf{E} - \theta \Delta t \left[c^2 \left(\nabla \times \Delta \mathbf{B} \right) - \zeta c^2 \nabla \Delta \phi - \sum_s \frac{e_s \left(\Delta n_s \mathbf{u}_s^k + n_s^k \Delta \mathbf{u}_s \right)}{\epsilon_0} \right] = \Delta t \left[c^2 \left(\nabla \times \mathbf{B}^k \right) - \zeta c^2 \nabla \phi^k - \sum_s \frac{e_s n_s^k \mathbf{u}_s^k}{\epsilon_0} \right] \ , \tag{243}$$

$$\Delta \mathbf{B} + \theta \Delta t \left[\left(\nabla \times \Delta \mathbf{E} \right) + \xi \nabla \Delta \varphi \right] = -\Delta t \left[\left(\nabla \times \mathbf{E}^k \right) - \xi \nabla \varphi^k \right] \ , \tag{244}$$

$$\Delta \mathbf{u}_s + \theta \Delta t [\left(\mathbf{u}_s^k \cdot \nabla\right) \Delta \mathbf{u}_s + \left(\Delta \mathbf{u}_s \cdot \nabla\right) \mathbf{u}_s^k$$
$$- \frac{e_s}{m_s} \left(\Delta \mathbf{E} + \mathbf{u}_s^k \times \Delta \mathbf{B} + \Delta \mathbf{u}_s \times \mathbf{B}^k\right)$$
$$+ \frac{\nabla \Delta T_s}{m_s} + \frac{T_s^k \nabla \Delta n_s}{m_s n_s^k} + \frac{\Delta T_s \nabla n_s^k}{m_s n_s^k} - \frac{\left(T_s^k \nabla n_s^k\right) v n_s}{m_s \left(n_s^k\right)^2}] =$$
$$- \Delta t \left[\left(\mathbf{u}_s^k \cdot \nabla\right) \mathbf{u}_s^k - \frac{\nabla T_s^k}{m_s} - \frac{T_s^k \nabla n_s^k}{m_s n_s^k} + \frac{e_s}{m_s} \left(\mathbf{E}^k + \mathbf{u}_s^k \times \mathbf{B}^k\right)\right] , \quad (245)$$

$$\Delta n_s + \theta \Delta t \left[\nabla \cdot \left(n_s^k \Delta \mathbf{u}_s + \Delta n_s \mathbf{u}_s^k\right)\right] = -\Delta t \nabla \cdot n_s^k \mathbf{u}_s^k , \quad (246)$$

$$\Delta T_s + \theta \Delta t \left[\left(\mathbf{u}_s^k \cdot \nabla\right) \Delta T_s + \left(\Delta \mathbf{u}_s \cdot \nabla\right) T_s^k + \frac{2}{3} T_s^k \left(\nabla \cdot \Delta \mathbf{u}_s\right) + \frac{2}{3} \Delta T_s \left(\nabla \cdot \mathbf{u}_s^k\right)\right] =$$
$$- \Delta t \left[\left(\mathbf{u}_s^k \cdot \nabla\right) T_s^k - \frac{2}{3} T_s^k \left(\nabla \cdot \mathbf{u}_s^k\right)\right] . \quad (247)$$

In addition, the time-discretized form of the corrective potential for the hyperbolic versions of Maxwell's equations is given as

$$\Delta \phi + \theta \Delta t \left[\zeta (\nabla \cdot \Delta \mathbf{E}) - \zeta \sum_s \frac{e_s \Delta n_s}{\epsilon_0}\right] = -\Delta t \left[\zeta (\nabla \cdot \mathbf{E}^k) + \zeta \sum_s \frac{e_s n_s^k}{\epsilon_0}\right] , \quad (248)$$

$$\Delta \varphi + \theta \Delta t \xi c^2 \nabla \cdot \Delta \mathbf{B} = -\Delta t \xi c^2 \nabla \cdot \mathbf{B}^k . \quad (249)$$

CURRICULUM VITAE

RICHARD F DATWYLER

Address
525 Aspen Drive
Rigby, ID 83442
(435) 881-4823
datwylerr@byui.edu

EDUCATION

- PhD May 2013 Utah State University, Logan, UT.
- BS May 2003 Physics Mathematics Dual degree, Cum Laude, Utah State University, Logan, UT.

RESEARCH INTEREST

- Plasma containment, transport theory, closure theory.
- Numerical methods, finite element and finite differences schemes.

RESEARCH EXPERIENCE

Graduate Research Assistant, Department of Physics, Utah State University.
Computational analysis of numerical modeling of minimum energy states, derivation and modeling of equations governing state, July 2008 - June 2009, January 2001 - July 2011.

Undergraduate Research Assistant, Department of Physics, Utah State University.
Assisted in developing models to describe large, stochastic fluctuations in water flow through fractured rock layers, December 2000 - August 2002.

TEACHING EXPERIENCE

Instructor

Brigham Young University Idaho, Rexburg, ID.
Designed course curriculum to help students prepare, teach one another, and ponder/prove ideas through: preparation assessment, group teaching assignments, quizzes, homework, exams. Also utilized laboratory, visual and online materials to aid in learning.

- "Introductory Applied Physics 1" (PH 105) and associated labs. Fall 2011, Winter 2012, Fall 2012 (2 sections each), Winter 2013, Spring 2013 (4 sections each).
- "Introductory Applied Physics 2" (PH 106) and associated labs. Spring 2012 (2 sections).
- "Principles of Physics 1" (PH 121) Fall 2011, Winter 2012.
- "Science Foundations" (FDSCI 101) Winter 2012, Spring 2012 (3 sections), Fall 2012 (3 sections).

Utah State University, Logan, UT.
Developed class curriculum focusing on learning through: homework assessments, quizzes, laboratories, exams, lectures, and other online materials.

- "Elements of Mechanics" (Phys 2200) Summers of 2007, 2008, 2009, 2010.
- "General Physics - Science and Engineering" (Phys 2210) Summers of 2007, 2008, 2009, 2010.
- "General Physics - Life Science II" (Phys 2120) Spring 2010.
- "Rock Climbing: Basic" (PE 1640) Fall 2001- Fall 2005.

Recitation Teacher

Utah State University, Logan, UT.
Managed grade book, organized online homework, taught weekly recitation classes, and taught lectures for professors when needed.

- "General Physics - Life Science I & II (Phys 2110 & 2120) 2004-2005, 2010-2011.
- "Elements of Mechanics" (Phys 2200) 2006-2008.
- "General Physics - Science and Engineering I & II" (Phys 2210 & 2220) 2006-2008 and Fall 2009.

Laboratory Teacher

Utah State University, Logan, UT.
Set up weekly labs with initial lecture, demonstration, and quizzes.

- "Elements of Mechanics" (Phys 2200) 2000-2003 and 2006-2008.
- "General Physics - Science and Engineering I & II" (Phys 2210 & 2220) 2000-2003, 2006-2008, and Fall 2009.
- "General Physics - Life Science I & II" (Phys 2110 & 2120) 2010-2011.
- Rewrote laboratory manuals for Phys 2110, 2120, 2200, 2210, and 2220. Focusing on exploratory questions, ease of reading design and integrating in new data analysis system. Summer 2003.

Tutor

Utah State University, Logan, UT.
Held weekly learning center hours. 2006-2008, Fall 2009 and 2010.

Tutor.com, New York, NY.
Tutored high-school and first year college students on topics of calculus and physics, Summer and Fall 2008.

SCHOLARSHIPS AND AWARDS

Nominated for Utah State University Graduate Teacher of the Year 2011.
Utah State University, College of Science Graduate Teacher of the Year 2011.
Farrell and Ann Edwards Endowment, for commitment to research and teaching 2010.
Utah State University, Physics Department Teaching Assistant of the Year 2008.
Utah State University, College of Graduate Studies Presidential Fellowship 2005.
Utah State University, Physics Department undergraduate Departmental Scholarship 2002.
Utah State University, Alpha Epsilon Delta Service Award and Scholarship, 2002.
Utah State University, College of Science Tuition waiver Scholarship 2001.
Utah State University, Honors at Entrance Scholarship 1-year tuition waiver, 1997.
Brigham Young University, University Scholar, 1-year tuition waiver (rejected) 1997.
University of Utah, Alumni Achievement Scholarship, 1-year tuition waiver (rejected) 1997.
Science and Mathematics Deseret News Sterling Scholar, 1997.
AP Scholar with Honors, 1997.

SKILLS

Computer: VI editing, FORTRAN, Maple, Mathematica, Excel.

CONFERENCE PRESENTATIONS

- Richard F Datwyler, "Fusion, Plasma, and Computation," Idaho State University, Colloquium speaker, Pocatello, ID, March 2013.
- Richard F Datwyler, "Fusion, Plasma, and Computation," Brigham Young University Idaho, Colloquium speaker, Rexburg, ID, January 2013.
- Richard F Datwyler, "Two species plasma fluid tests with 2D Fourier transform analysis," NIMROD Annual Team Meeting, Logan, UT 2011.
- Richard F Datwyler, Nels J. Rasmussen, Paul D. Simonson, David Peak, "Giant Fluctuations in Water Flow Through a Fractured Rock Medium," National Council for Undergraduate Research 2002, U. Wisconsin-Whitewater, April 26, 2002.
- Richard Datwyler, Paul Simonson, David Peak, Thomas R. Wood, Daphne Stoner, Thomas M. Stoops, "Giant Fluctuations in Water Flow Through a Fractured Rock Medium," Council for Undergraduate Research Posters on the Hill, Washington, D.C., April 18, 2002.
- Richard Datwyler, Nels Rasmussen, Paul Simonson, and David Peak, "Giant Fluctuations in Water Flow Through a Fractured Rock Medium," Utah Posters on the Hill, Utah State Capitol, Salt Lake City, UT, 2002.
- D. Peak, R. Datwyler, N. Rasmussen, P. Simonson, T.R. Wood, and T.M. Stoops, "Giant Fluctuations in Flow Through Fractured Media: A Stochastic, Self-Organized Dynamics Model," The International Conference for Chaos and Nonlinear Dynamics: Dynamics Days 2002, Baltimore, MD, January 4-7, 2002.
- Richard Datwyler, Nels Rasmussen, Paul Simonson, and David Peak, "Colossal Fluctuations in Water Flow Through a Fractured Rock Medium," USU Presidential Research Showcase, Utah State University, Logan, UT, November 2001.